Degradation and Thermal Performance of Li-ion Batteries: Implications for Electric Vehicles

Malgorzata Ewa Wojtala

Trinity College

University of Oxford

A thesis submitted for the degree of

Doctor of Philosophy in Engineering Science

21/04/2023

Declaration

I hereby declare that except where specific reference is made to the work of others, the contents of this dissertation are original and have not been submitted in whole or in part for consideration for any other degree or qualification in this, or any other university. This dissertation is my own work and contains nothing which is the outcome of work done in collaboration with others, except as specified in the text and Acknowledgements. Parts of the work have been presented at conferences and published in journal papers; these are specified in the text and referenced accordingly.

21 April 2023

Malgorzata E. Wojtala

To my parents, who always maintained a steadfast belief in the transformative power of education and the pursuit of knowledge, even when I may have wavered.

Acknowledgements

First and foremost, I would like to thank Professor David Howey for his guidance and his tireless efforts to help me succeed in my academic pursuits. I would also like to extend my thanks to Professor Charles Monroe for his invaluable discussions and access to his lab facilities.

I would like to express my gratitude to Andrew Wang, Luis Couto, Jie Lin, Eloise Tredenick, Guanchen Li, and Volkan Kumtepeli for sharing their knowledge and expertise with me. I am also grateful to my BIL colleagues Jorn Reniers, Antti Aittio, Samuel Greenbank, Taeho Jung, Zihao Zhou, Masaki Adachi, and Rebecca Perriment for their help and support.

I could not have survived my PhD journey without MD PhD Piotr Lukasik, who agreed for the questionable pleasure of reconstructing my leg repeatedly after my tennis endeavours. No matter the consequences, I would still like to thank the culprits: tennis and volleyball clubs and my amazing friends. Special thanks to Cooper, who transformed Covid-19 lockdown into a positively memorable time.

The funding generously provided by EPSRC, Trinity College, Edgell Sheppe, and Kandiah Thiruvukkarsau scholarships has been instrumental in making this work possible.

Abstract

Worldwide adoption of transport electrification creates a demand for optimised energy storage and control systems. This technology, despite being under strong development, has not yet reached its maturity and the electric vehicle (EV) performance envelope still needs improvement. This work investigates key challenges in battery management systems (BMS) and battery modelling for EVs, with a focus on ageing diagnostics, its effective inclusion within the BMS, and an accurate internal state estimation during high current applications i.e. fast charging.

Entropy profiling was investigated as a new approach to tackle the challenge of battery degradation diagnosis. This method leverages the interpretation of temperature and concentration dependencies of cell voltage to provide insight into the morphological changes experienced during battery life. The study finds that entropy profiling can successfully track ageing markers in a complementary way to differential voltage analysis, making it a useful battery diagnostics tool.

Even if degradation diagnosis is performed successfully, the inclusion of ageing information into a BMS is problematic. As an alternative, a periodic model parameter update is proposed here. The impact of this work was two-fold. Firstly, it highlights how the single particle model can accurately simulate both pristine and aged cell voltage responses with appropriate parameter updates. Secondly, it provides qualitative insight into the impact of ageing on model parameters, informing safety issues such as increased heat generation.

The prediction of heat generation during fast charging is a significant concern when considering the safety and performance of batteries. To address this issue, a pseudo-3D thermal-continuum model was proposed and tested up to 10C. The results showed that the fast diffusion encountered in high-power cells allows for substantial model simplifications without compromising prediction accuracy.

Publications

Research presented in this thesis has been published in the following articles and conference abstracts:

[1] Wojtala, M., Zulke, A.A., Burrell, R. M., Nagarathinam, M., Li, G., Hoster, H., Howey, D. and Mercer, M.P., 2022. Entropy profiling for the diagnosis of NCA/Gr-SiOx Li-ion battery health. Journal of The Electrochemical Society.

[2] Wojtala, M., Brosa Planella, F., Hoster, H., Howey, D. and Mercer, M.P., 2022. Investigating changes in transport, kinetics and heat generation over NCA/Gr-SiOx battery lifetime. 2022 IEEE Vehicle Power and Propulsion Conference, VPPC 2022 Proceedings.

[3] Wojtala, M.E., Zulke, A.A., Burrell, R., Mercer, M.P., Hoster, H. and Howey, D., 2022, July. Entropy Hysteresis during Lithiation/Delithiation of NCA/Gr-Si Battery Subjected to Accelerated Calendar Ageing and Cycle Ageing – in Electrochemical Society Meeting Abstracts 241 (pp. 528-528).

[4] Wojtala, M.E., Kumtepeli, V., Monroe, C.W., Howey D.A., 2023, March. Li-ion battery in high C-rate conditions: improving the temperature prediction – in ModVal 2023-19th Symposium on Fuel Cell and Battery Modeling and Experimental Validation.

[5] Zulke, A.A., Wojtala, M., Hoster, H.E. and Howey, D., 2020, November. Tracking Thermodynamic Changes Due to Cycling and Calendar Ageing of Commercial High-Energy Li-Ion Cells: Effects of Relaxation Periods – in Electrochemical Society Meeting Abstracts PRiME 2020 (pp. 104-104).

The author was also involved in the following article; this work is not covered in this thesis

[6] Lin, J., Chu, H.N., Thu, K., Wojtala, M., Gao, F. and Chua, K.J., 2023. Novel battery thermal management via scalable dew-point evaporative cooling. Energy Conversion and Management, 283, p.116948.

Contributions

In [1] we present an entropy profiling method for the diagnosis of a battery health. It was discovered that in addition to lithiation/delithiation hysteresis in the open circuit potential of Gr-Si blends, cells with Gr-Si anodes also exhibit differences in entropy profile depending on cycling direction, reflecting degradation-related morphological changes. The topic of entropy profiling is explored here in Chapter 2. This work was also presented at the 241st Meeting of the Electrochemical Society in May 2022, in Vancouver, Canada [3], with early project results also included in ECS PRiME 2020 conference [5]. The work was undertaken in collaboration with Lancaster University, who ran the long term ageing experiments in their lab, performed by Dr Alana Zulke, supervised by Professor Harry Hoster. My contributions in this work included idea formation, development of MATLAB code for entropy extraction (originally developed by [7]), data analysis, cell-teardown, and sample preparation for the SEM analysis. The SEM analysis was conducted by Chris Salter (Oxford Materials Characterisation Service). The work was written by me, and reviewed by Dr Michael Mercer, Dr Guanchen Li, and Professor David Howey who provided the foundation of the theory and general advice.

In [2], we traced the kinetic and transport changes taking place over battery lifetime through inverse modelling, highlighting significant increase in diffusion time and kinetic over-potential. This forms the basis for Chapter 3, which investigates the feasibility of electrochemical parameter updates during battery ageing. This work was presented at the IEEE Vehicle Power and Propulsion Conference (VPPC) in November 2022, in Merced, USA. My contribution to this work included idea formation, model development in COMSOL, experimental testing, data analysis and write-up. Dr Ferran-Brossa Planella provided guidance in PyBaMM model use as well as the development of the parameter optimisation. Professor David Howey provided general guidance and review.

In [4], we focused on modelling the cell response at high current rates, with the objective of accurately predicting battery states up to 10C. I conducted all of the experimental work, as well as model development in COMSOL and data analysis. Dr Volkan Kumtepeli developed the MATLAB code for the optimisation routine, as well as dynamic mode decomposition. This work is included in Chapter 4 and was presented by Dr Volkan Kumtepeli at the ModVal 2023 Conference in Duisburg, Germany, in March 2023. Technical guidance and review were provided throughout this study by Professor David Howey and Professor Charles Monroe.

Contents

List of Figures

List of Tables

Nomenclature

Acronyms and abbreviations

BMS battery management system

DFN Doyle-Fuller-Newman

DMD dynamic mode decomposition

DTV differential thermal voltammetry

DVA differential voltage analysis

ECM equivalent circuit model

EIS electrochemical impedance spectroscopy

EOL end of life

EV electric vehicle

FIB focused ion beam

ICA incremental capacity analysis

LAM loss of active material

LLI loss of lithium inventory

MLE maximum-likelihood estimate

OCP open circuit potential

P2D pseudo-2-dimensional model

SEI solid-electrolyte interphase

SEM scanning electron microscope

SOC state of charge

SOH state of health

SPM single particle model

SPMe single particle model with electrolyte dynamics

Q cell capacity

Energy and heat balance

$\boldsymbol{\alpha}$ thermal diffusivity

$\boldsymbol{\Delta G}$ Gibbs free energy of reaction (J/mol)

$\boldsymbol{\mu}$ electrochemical potential (J/mol)

$\boldsymbol{\rho}$ density (kg/m^3)

A cooling area (m^2)

$\mathbf{C}_\mathrm{p}$ heat capacity (J/K)

E output voltage (V)

$\mathbf{E}_\mathrm{OCP}$ open circuit potential (V)

F Faraday's constant (C/mol)

H enthalpy (J)

h heat transfer coefficient ($W/m^2/K$)

I applied current (A)

k thermal conductivity (W/m/K)

n number of reactants/products (-)

p pressure (Pa)

q volumetric heat generation rate ($J/K/m^3$)

$\mathbf{Q_0}$ nominal capacity of the cell (Ah)

$\mathbf{\Delta S}$ entropy of reaction (J/K)

T temperature (K)

$\mathbf{T}_{\text{amb}}$ ambient temperature (K)

v stoichiometry of reactant/products (-)

x SOC (-)

z electric charge (C)

Physics-based models

$\boldsymbol{\alpha}$ anodic charge transfer coefficient (-)

$\boldsymbol{\alpha_\kappa}$ temperature coefficient of κ (mS/m/K)

$\boldsymbol{\Delta S}$ entropy change (J/mol/K)

$\boldsymbol{\varepsilon_s}$ active material volume fraction (-)

$\boldsymbol{\eta}$ overpotential (V)

$\boldsymbol{\kappa}$ electrolyte ionic conductivity (S/m)

$\boldsymbol{\lambda}_{\mathrm{D}}$ diffusion ageing parameter (-)

$\boldsymbol{\sigma}$ matrix-phase conductivity (S/m)

$\boldsymbol{\tau}_{\mathrm{D}}$ diffusion time (s)

$\boldsymbol{\Theta}$ parameter vector (-)

$\mathbf{A}$ electrode active area (m^2)

$\mathbf{a}_{\mathrm{v}}$ specific active surface area (1/m)

$\mathbf{ai}_0$ volumetric exchange current density ($\mathrm{A/cm}^3$)

$\mathbf{c}$ Li concentration in solid phase ($\mathrm{mol/m}^3$)

$\mathbf{c}_0$ initial Li concentration in solid phase ($\mathrm{mol/m}^3$)

$\mathbf{c}_{\mathrm{l}}$ electrolyte concentration (mol/l)

$\mathbf{c}_{\mathrm{l}}^{\mathbf{0}}$ initial electrolyte concentration (mol/l)

$\mathbf{c}^{\mathrm{avg}}$ average concentration of Li in solid phase ($\mathrm{mol/m}^3$)

$\mathbf{c}^{\mathbf{max}}$ maximum concentration of Li in solid phase ($\mathrm{mol/m}^3$)

$\mathbf{c}^{\mathrm{s}}$ Li concentration at particle surface ($\mathrm{mol/m}^3$)

$\mathbf{D}_{\mathrm{l}}$ electrolyte diffusion coefficient ($\mathrm{m/s}^2$))

$\mathbf{D}_{\mathrm{s}}$ solid diffusion coefficient (m)

$\mathbf{Ei_0}$ activation energy (kJ/mol)

$\mathbf{i}$ current density (A/m^2)

$\mathbf{i_l}$ current density in liquid (A/m^2)

$\mathbf{i_s}$ current density in solid (A/m^2)

$\mathbf{i_0}$ exchange current density (A/m^2)

$\mathbf{I_{lim}}$ limiting current (-)

$\mathbf{J}$ electrochemical rate for the Li-ion (de)intercalation at solid/solution interface

$\mathbf{k}$ kinetic/reaction rate constant (m/s)

$\mathbf{k_U}$ open circuit potential gradient (V)

$\mathbf{L}$ coating thickness (m)

$\boldsymbol{\phi_l}$ electrical potential in the liquid phase

$\boldsymbol{\phi_s}$ electrical potential in the solid phase

$\mathbf{q}$ effective SOC at the particle surface

$\mathbf{R}$ gas constant (J/K/mol)

$\mathbf{R_p}$ particle radius (m)

$\mathbf{t_+}$ transport number (-)

$\mathbf{v}$ heat transfer velocity $\frac{h}{Cp}$ (µm/s)

$\mathbf{V_{hys}}$ open circuit potential hysteresis

$\mathbf{x}$ stoichiometry (-)

Chapter 1

Challenges and opportunities in battery management systems for electric vehicles

This chapter provides an in-depth examination of the key challenges encountered by electric vehicles (EVs), with a focus on battery management systems. Through a thorough review of current state-of-the-art methods, the chapter aims to identify areas with potential for further improvement and development:

- battery ageing diagnostics,
- effective inclusion of predicted degradation within the battery management system,
- accurate prediction of internal and measurable (voltage, temperature) battery states at high current rates (e.g., fast charge).

By examining these three key areas, the aim is to contribute to the development of advanced battery management systems for electric vehicles.

1.1 Introduction

Li-ion batteries have successfully made the leap from small portable devices to large-scale applications, where multi-cell arrangements must be effectively monitored and controlled by a battery management system (BMS) to guarantee durable and safe operation [8, 9]. The BMS requires reliable inference of state-of-charge and state-of-health (SOC and SOH), and this is more challenging as Li-ion batteries age. Currently, inaccurate SOC and SOH estimation algorithms are compensated for by over-designing battery packs and keeping conservative operational limits, which increases costs and carbon footprint. Research on the modelling of battery internal states using only the available measurements provided by the BMS (voltage, current and temperature) is therefore fundamental to accelerate battery innovation, and there is a rising demand for ageing data and battery models [10–12].

The challenge of accurate battery state prediction is compounded by its desired application in electric vehicles (EVs). Batteries are packed in large modules which makes monitoring individual units problematic or infeasible in certain cases. Furthermore, EV users want their vehicles to be charged quickly, yet have a long driving range on a single charge, creating conflicting design requirements—for example, the use of power-dense cells to support fast charging vs. energy-dense cells to increase capacity for improved driving range. Additionally, excessive currents promoted by the fast charge desire exaggerate degradation processes, decreasing battery performance and shortening useful life. Thus, finding a solution to these problems remains a pressing challenge.

The purpose of this chapter is to present a comprehensive review of the current state-of-the-art methods utilised to tackle cell control where scientific understanding needs to be improved.

1.2 Battery modelling

The field of battery modelling can be broadly divided into three categories: equivalent circuit models (ECMs) continuum models, and atomistic models [13].

ECMs are simple mathematical representations that are derived from experimental data and provide quick and easy predictions of battery behaviour. Here battery is represented by an ideal voltage source, a series resistor(s), and a capacitor(s) [14]. However, ECMs may not provide detailed insight into the underlying physical and chemical processes that occur within the battery.

The continuum models are based on porous-electrode theory and use coupled partial differential equations to describe mass-transport in liquid and solid phases [15,16]. However, this complexity comes at the expense of heavily increased computation time and complicated characterisation protocol. The continuum-scale models include the microscale models [17], homogenised models [17] and the 'pseudo-2D' Doyle-Fuller-Newman (DFN) model [15, 16] with its subsequent derivations to a single particle model (SPM) and SPM with electrolyte (SPMe) [18, 19]. Additionally, it is also possible to integrate thermal effects and mechanical stress dynamics into the continuum models [20, 21].

Atomistic models use molecular dynamics or density functional theory to simulate the behaviour of batteries at the atomic or molecular scale [22]. They provide a detailed representation of the behaviour of individual atoms, ions, and electrons within a material, and are used to study the behaviour of materials and systems that are not accessible to experimental observation. Despite the high level of detail that atomistic models provide, they are also computationally intensive, making them less practical for use in real-time applications.

Equivalent circuit models are good fit for EV BMS onboard use, given their simplicity and computational speed. However, to create a more advanced BMS control, models that give more insight into the underlying physical and chemical processes

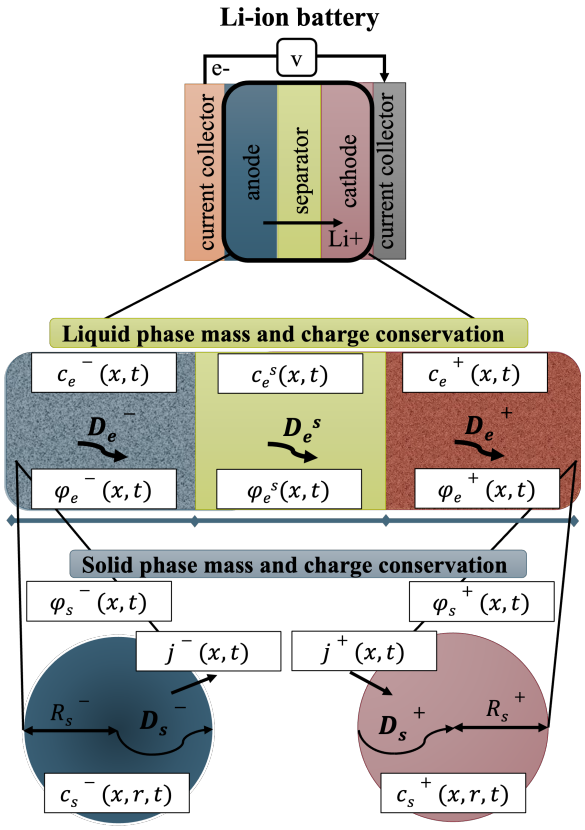

Figure 1.1: DFN model schematic of a Li-ion battery during charge, adopted and modified from [23].

may be considered. With this in mind, but also considering the computational cost increasing with model complexity, the focus here is placed on continuum models.

1.2.1 Continuum models: DFN and SPM

Doyle, Fuller and Newman proposed perhaps one of the most popular Li-ion battery models up to date, the DFN model [15]. The DFN model uses a collection of governing laws describing individual processes taking place across the porous electrodes and liquid electrolyte. This includes mass and charge conservation in the solid phase electrodes. A schematic representation of a DFN model is shown in Fig. 1.1.

The DFN model assumes that electrodes may be modelled as a collection of spherical particles within the electrode volume. The macroscopic dimension x is defined

across the electrode-separator-electrode 'sandwich' thickness and includes transport in the electrolyte. A microscopic problem is solved for the radial transport of ions within the electrode particles, and kinetics at the surface of each particle is defined by Butler-Volmer Eq. ([24]).

While the DFN model simplifies the 3D microstructure of the electrodes, it still requires careful implementation to solve the combination of linear and nonlinear partial differential equations and algebraic constraints. Moreover, it requires a total of 33 parameters, which are either obtained experimentally (resource consuming), or via parameter optimisation to experimental data. When parameter optimisation is used, the solution time should be sufficiently short to perform the required number of iterations to find the optimal solution.

To avoid (to some extent) the above mentioned problems, several DFN model reductions have been proposed, resulting in two simpler models – the single particle model (SPM) and the SPM with electrolyte (SPMe).

The SPM assumes that all particles within each electrode behave identically and hence can be modelled by a single representative 'average' spherical particle. It further simplifies the reaction current distribution across the porous electrodes, assuming it to be uniform. The potential gradients in the solid phase of the electrodes are neglected. The local potential and concentration gradients in the solution phase are ignored and accounted for using a lumped solution resistance term [18]. The SPM assumes that the electrolyte dynamics have a negligible impact on the measured voltage. This is a reasonable assumption for low C-rates, where C-rate is a measure of the rate at which a battery is charged or discharged, expressed in terms of the battery capacity. SPM model reductions result in significantly faster simulation effort and reduced number of parameters from 33 to 25. More details on the SPM can be found in the literature [25, 26]. Bizeray et al. [27] showed that it is possible to reduce number of model parameters needed by grouping them and partially nondimensionalising the

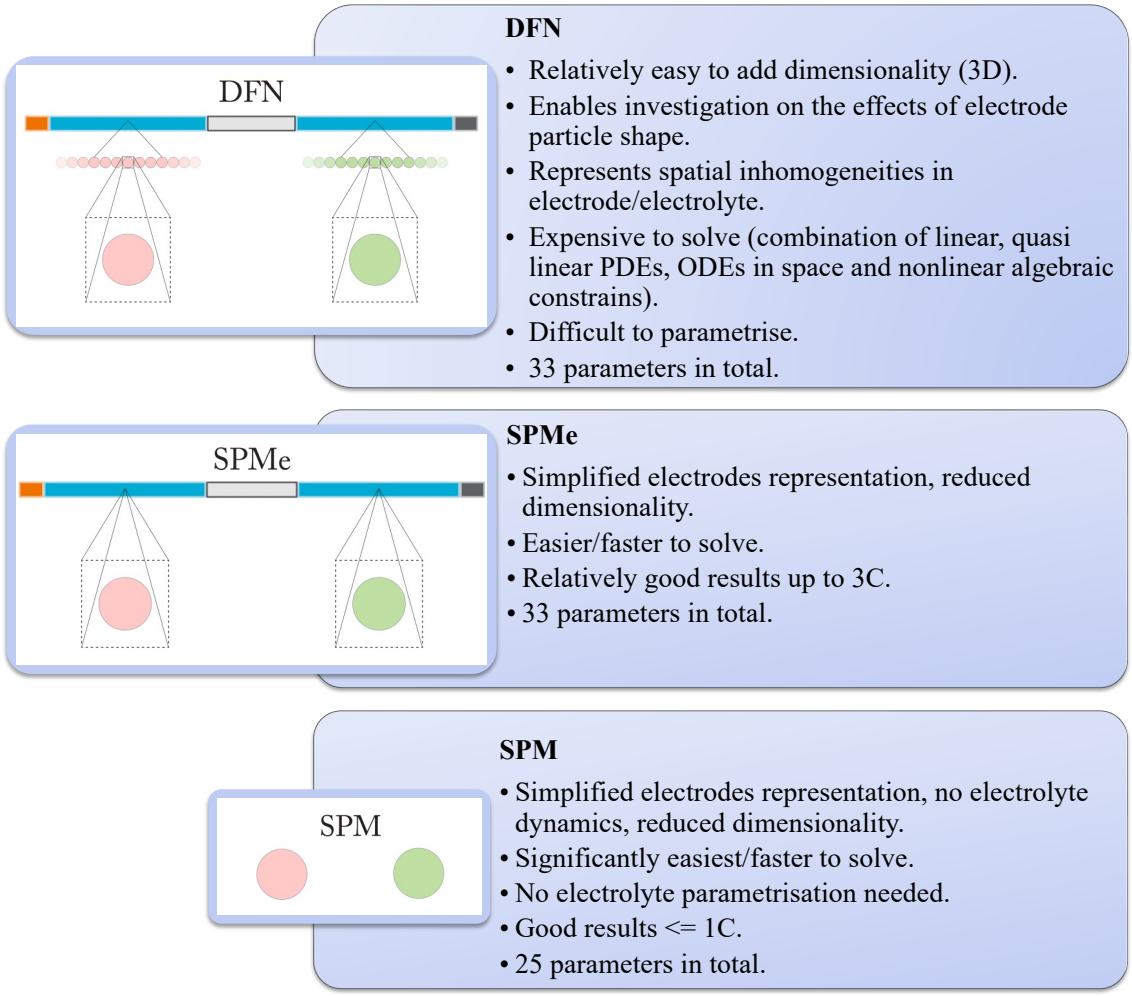

Figure 1.2: DFN, SPMe, SPM characteristics summary, diagrams taken from [17].

model. In this case number of parameters in SPM was reduced from 25 to 8 (the work quotes 6 parameters, but individual cell OCP is also counted as parameter here).

The SPMe can be placed between DFN and SPM in terms of complexity. Like the SPM, the electrodes are modelled by a single representative spherical particle and so the reaction current distribution across the porous electrodes is assumed to be uniform. However, unlike the SPM, the SPMe models the ionic current and consequently approximates the potential gradient and concentration gradients in the electrolyte. The inclusion of electrolyte dynamics improves model performance at higher C-rates, but also means that electrolyte parametrisation is necessary, hence no reduction in required number of parameters [28].

A summary of similarities and differences between DFN, SPM, and SPMe is illustrated in Fig. 1.2. The derivation of these models is widely available in the literature [18, 24, 28], with relevant model equations included in further chapters.

1.2.2 Temperature dependency

Certain battery parameters exhibit temperature dependency. To model this behaviour, an (electrochemical) model can be coupled with a thermal model, which is further reviewed in section 1.2.4, and some electrochemical parameters given temperature dependency, which is often assumed to obey an Arrhenius relationship :

$$\Psi = \Psi_{\text{ref}} \exp\left[-\frac{E_\Psi}{R}\left(\frac{1}{T_\text{l}} - \frac{1}{T_{\text{ref}}}\right)\right], \tag{1.1}$$

The temperature dependent parameters are typically:

$$\Psi \in \left\{D_\text{s}^\pm, D_\text{l}, k^\pm, \kappa\right\}, \tag{1.2}$$

where $D_\text{s}^\pm$ is solid diffusivity, D_l is electrolyte diffusivity, $k^\pm$ is the kinetic rate constant, and κ electrolyte conductivity. Superscript '$\pm$' refers to positive and negative electrodes respectively.

1.2.3 Parametrisation of the SPM, SPMe and DFN models

The parametrisation of the DFN-derived models requires information on the geometrical properties of the electrodes, such as their size, coating thickness, and number of layers. These can be fairly easily extracted from a cell tear-down. However, measurement of micro-scale geometry parameters requires more specialised equipment and careful procedures. Conventionally, the distribution of particle sizes, and electrode porosities, are obtained through scanning electron microscope (SEM) analysis [29] or focused ion beam milling SEM (FIB-SEM) [29], as well as mercury porosimetry [30].

The summary of all geometrical parameters required for DFN, SPMe and SPM is in Table 1.1. The extraction of the electrochemical parameters poses perhaps an even bigger challenge. The maximum allowable concentration of lithium in the electrode solid material is usually calculated based on electrode loading, coating thickness, active material volume fraction and molar mass. To extract anode and cathode OCP curves, half cells or three-electrode cells must be constructed, then OCP or pseudo-OCP can be measured [29]. The kinetic rate constant and diffusion coefficient can be estimated from electrochemical impedance spectroscopy (EIS) data [31], with alternative methods available and summarised in Table 1.2.3. Film contact resistance, as well as the electrical conductivity of the current collectors, is measured with a four point probe [30]. While various experimental methods have been proposed to estimate the Bruggeman constant to account for tortuosity, their accuracy is questionable and very often it is therefore fitted to data, or assumed as a value of 1.5. Electrolyte conductivity is measured with a conductometer that has a four-electrode glass/platinum probe [32, 33]. Galvanostatic polarisation experiments [32] are used to estimate both salt diffusion and the transport number [32–34]. The mean molar activity coefficient can be estimated from Debye-Huckel theory [35], which provides mathematical relationship between the mean molar activity coefficient and the reference salt concentration. An infrared spectroscopy is used to estimate the reference salt concentration in an electrolyte based on the analysis of absorption/transmission of light through the electrolyte [36].

Temperature dependency involves one more group of parameters. This may include the heat capacity of each material, although often bulk (homogenised) properties are considered. Lin et al. [20] proposed an efficient method of full cell heat capacity characterisation by applying Newton's law of cooling to an insulated container (thermal bath), in which a cell was submerged in dielectric fluid at elevated temperature. Heat transfer coefficient values can be roughly chosen for a given known transfer

medium, but the exact number is predominantly found from data fitting/optimisation. The activation energies for diffusivities and kinetic rates are found by measuring the appropriate parameter (diffusion coefficient or rate constant) over a range of temperatures and then applying the Arrhenius relation [29, 37, 38].

To summarise, electrochemical parametrisation is a long and cumbersome process, relying on methods that do not always provide the desired level of accuracy. However, the alternative is limited to parameter fitting from cell data, which cannot be performed over a full range of parameters due to parameter (un)identifiability and computational cost. The parameter identifiability refers to the ability to uniquely determine parameter value from observed data (current, voltage, temperature). Bizeray et al. [27] studied 'structural' identifiability which is irrespective of the identification data considered, while, Aitio [39, 40] discussed 'practical' identifiability, which accounts for quality of input and output. A common practice to identify parameter sensitivity to one another is via estimating the correlation between parameters [41, 42].

Table 1.1: Parametrisation summary and methods for SPM, SPMe and DFN models.

	Required parameter	SPM	SPMe	DFN	Parametrisation method
Physical design parameters	Cell geometry				
	Positive electrode thickness [m]	Y	Y	Y	Manufacturer/teardown, incremental length gauge [29].
	Negative electrode thickness [m]	Y	Y	Y	
	Separator thickness [m]	Y	Y	Y	
	Positive current collector thickness [m]	N	N	N	
	Negative current collector thickness [m]	N	N	N	
	Positive electrode length [m]	Y	Y	Y	
	Negative electrode length [m]	Y	Y	Y	
	Positive electrode width [m]	Y	Y	Y	
	Negative electrode width [m]	Y	Y	Y	
	Tabs dimensions [m]	N	N	N	
	Microscale geometry				
	Mean particle radius of positive electrode [m]	Y	Y	Y	Scanning electron microscopy (SEM) [29], mercury-porosimetry [30].
	Mean particle radius of negative electrode [m]	Y	Y	Y	
	Positive electrode porosity (electrolyte volume fraction) [-]	Y	Y	Y	Manufacturer, gas surface absorption (BET theory) and mercury porosimetry. Imaging techniques, such as X-ray tomography and electron microscopy, e.g. focused ion beam milling with scanning electron microscopy (FIB-SEM) [29]. FIB-SEM gives quantitative information about porosity, particle shapes and densities, packing density and carbon and binder domain distribution [29].
	Negative electrode porosity (electrolyte volume fraction) [-]	Y	Y	Y	
	Positive electrode solid phase (active material volume fraction) [-]	Y	Y	Y	
	Negative electrode solid phase (active material volume fraction) [-]	Y	Y	Y	

	Required parameter	SPM	SPMe	DFN	Parametrisation method
			Electrode		
Electrochemical	Nominal cell capacity [Ah]	N	N	N	Capacity test.
	Electrical conductivity of positive current collector [S/m]	N	N	N	Literature - standard materials (copper, aluminum).
	Electrical conductivity of negative current collector [S/m]	N	N	N	
	Electrical conductivity of positive electrode [S/m]	N	**Y**	**Y**	Delamination, then voltage response to a DC current using four point probe (4FPP) method [30].
	Electrical conductivity of negative electrode [S/m]	N	**Y**	**Y**	
	Diffusivity of positive electrode [m2/s]	**Y**	**Y**	**Y**	GITT, EIS, PITT [43].
	Diffusivity of negative electrode [m2/s]	**Y**	**Y**	**Y**	
	Bruggeman constants (positive and negative electrodes, separator) [-]	N	**Y**	**Y**	Often assumed ∼1.5 for all/ optimisation/tortuosity can also be determined by the electrochemical impedance spectroscopy (EIS) [29]. Hg-porosimetry [30]. Methods with questionable accuracy fit for model.
	Maximum concentration of positive electrode solid material [mol/m3]	**Y**	**Y**	**Y**	Calculated from electrode coating mass (loading), thickness, active material volume fraction, fraction of Li per mole of LiMO2 and molar mass [29, 44].
	Maximum concentration of negative electrode solid material [mol/m3]	**Y**	**Y**	**Y**	
	Stoichiometry of positive electrode at 0% and 100% SOC [-]	**Y**	**Y**	**Y**	Combination of a HC and 3EL, assuming full lithiation. Eg. OCP of a HC and then DVA/ALAWA toolboox/similar. 3EL to remove Li potential contribution [29].
	Stoichiometry of negative electrode at 0% and 100% SOC [-]	**Y**	**Y**	**Y**	

	Required parameter	SPM	SPMe	DFN	Parametrisation method
Electrochemical	OCP of positive electrode []	**Y**	**Y**	**Y**	HC and/or 3EL, then pseudo OCV/GITT [29].
	OCP of negative electrode []	**Y**	**Y**	**Y**	
	Charge transfer coefficient for positive and negative electrodes [-]	**Y**	**Y**	**Y**	Assumed symmetry for Li-ion (theoretical value = 0.5) [45].
	Kinetic rate constant for positive electrode [m/s]	**Y**	**Y**	**Y**	EIS [31].
	Kinetic rate constant for negative electrode [m/s]	**Y**	**Y**	**Y**	
	Film contact resistance (SEI) [Ωm^2]	Y	Y	Y	4FPP, micro 4FPP [46].
	Electrolyte				
	Electrolyte ionic diffusivity [m^2/s]	N	**Y**	**Y**	Galvanostatic polarisation, nuclear magnetic resonance [30, 32, 47].
	Mean molar activity coefficient in electrolyte [-]	N	**Y**	**Y**	Debye-Huckel theory [35], Potentiometric titration [48].
	Transference number [-]	N	**Y**	**Y**	Galvanostatic polarisation, Hittorf formula [32, 34].
	Electrolyte volume fraction [-]	N	**Y**	**Y**	Manufacturer [29, 30]
	Electrolyte reference concentration [mol/m3]	**Y**	**Y**	**Y**	Spectroscopic analysis [36].
	Electrolyte ionic conductivity [S/m]	N	**Y**	**Y**	Conductometer with a four-electrode glass/platinum probe [32].
	Electrode and electrolyte				
Thermal	Activation energy of diffusion in electrolyte [J/mol] or [eV]	Y	Y	Y	Measuring diffusion coefficient over a range of temperatures and then applying the Arrhenius relation [38].
	Activation energy of diffusion in positive electrode [J/mol]	Y	Y	Y	Measuring diffusion coefficient or rate constant over a range of temperatures and then applying the Arrhenius relation [29, 38].
	Activation energy of diffusion in negative electrode [J/mol]	Y	Y	Y	

	Required parameter	SPM	SPMe	DFN	Parametrisation method
Thermal	Activation energy of kinetic rate in positive electrode [J/mol]	Y	Y	Y	EIS over a range of temperatures in combination with Arrhenius relation [29, 37, 38].
	Activation energy of kinetic rate in negative electrode [J/mol]	Y	Y	Y	
	Thermal conductivity of positive electrode current collector [W/m/K]	N	N	N	Literature - standard materials (copper, aluminum).
	Thermal conductivity of negative electrode current collector [W/m/K]	N	N	N	
	Thermal conductivity of positive electrode [W/m/K]	N	Y	Y	Internal heating method, step change method [49].
	Thermal conductivity of negative electrode [W/m/K]	N	Y	Y	
	Thermal conductivity of separator [W/m/K]	Y	Y	Y	
	Heat capacity of positive electrode (at const pressure) [J/kg/K]	Y*	Y*	Y*	*Often bulk heat capacity measurement in thermal bath/thermal chamber [20].
	Heat capacity of negative electrode [J/kg/K]	Y*	Y*	Y*	
	Heat capacity of separator [J/kg/K]	Y*	Y*	Y*	
	Heat capacity of positive electrode current collector [J/kg/K]	Y*	Y*	Y*	
	Heat capacity of negative electrode current collector [J/kg/K]	Y*	Y*	Y*	
	Heat transfer coefficient	Y	Y	Y	The exact value often found via optimisation.

The 'Thermal' section in Table 1.2.3 is relevant to models considering thermal dependency. However, if an isothermal model is considered, the parameters listed in this section are not required. Table 1.2.3 could be further enhanced by including ageing models; however, battery ageing modelling is not directly addressed in this

work. The discussion about the inclusion of thermal dependency and ageing is further addressed in Chapter 1 Section 1.2.4 and Chapter 3respectively.

1.2.4 Multi-physics models: thermal modelling

Temperature prediction is another challenge faced by the battery community. Given the danger of thermal runaway, it is imperative to ensure operational conditions that are within the cell safety envelope (usually up to 60 °C). In a single cell setup a temperature sensor can be fitted to the surface of a cell, but measuring temperature becomes an issue in an EV application involving thousands of tightly packed cells in a battery pack. Another problem becomes temperature non-uniformity within a cell. Firstly, the cell core temperature is expected to be higher than the measured surface temperature, given limited cooling within the cell. Secondly, the location of tabs in a cell creates a non-uniform current flux, which results in temperature gradients across the cell surface. This makes the choice of sensor placement and its readings ambiguous.

To understand and address these challenges, battery thermal modelling is used. While thermal models vary in their level of complexity and approach, a basic understanding may be achieved using a lumped energy balance Eq. (1.3):

$$\rho C_{\mathrm{p}} \frac{dT}{dt} = -hA(T - T_{\mathrm{amb}}) - I\left(E - E_{\mathrm{OCP}}(x,T)\right) - IT\left(\frac{\partial E_{\mathrm{OCP}}(x,T)}{\partial T}\right)_{p,\mathrm{x}}. \quad (1.3)$$

The irreversible heat source term is the difference between the open-circuit potential E_{OCP} and an output voltage E, multiplied by an applied current I. The reversible heat is defined by the partial change in the E_{OCP} with respect to temperature T at constant pressure p and state of charge x. The heat of mixing [50] is neglected due to its low contribution. Heat removal is assumed to occur mostly via convection, where h is the heat transfer coefficient, A is the cooling area, and T_{amb} is the ambient

temperature. The C_{p} is heat capacity, ρ is density and $\frac{dT}{dt}$ marks temperature change in time. The validity of this lumped model relates to the Biot number $Bi = L\frac{h}{k}$, which indicates whether thermal gradients (ratio of thermal resistances) are present across the body volume; L is the characteristic length of the cell, h is the heat transfer coefficient, and k is thermal conductivity. A Biot number > 1 indicates spatial non-uniformity, while Biot numbers significantly lower than 1 indicate that temperature modelling can be considered as a simple lumped problem. In the literature spatial temperature uniformity is usually assumed for Biot <0.1 [51] for lumped thermal models. Radiation heat transfer is neglected.

1.2.4.1 Lumped thermal models

The lumped thermal models assume that there are no thermal gradients across the cell. This approximation is viable if the Biot number is small, i.e.,

$$\frac{1}{h} >> \frac{L}{k}. \tag{1.4}$$

This means that the thermal resistance to convection between the solid and the surrounding is much larger than the thermal resistance to conduction within the solid [51]. Common assumptions made in lumped thermal models are:

- two separate isothermal nodes for battery core and battery case,
- averaged and homogeneous properties for cell layers,
- uniform heat generation across the cell.

Equivalent circuit models are, essentially, networks of lumped thermal models. The energy balance Eq. (1.3) is represented by an equivalent electric circuit, with capacitors and resistors serving as representations of accumulation terms and heat transfer phenomena, respectively. Moreover, the heat source term Q is indicated

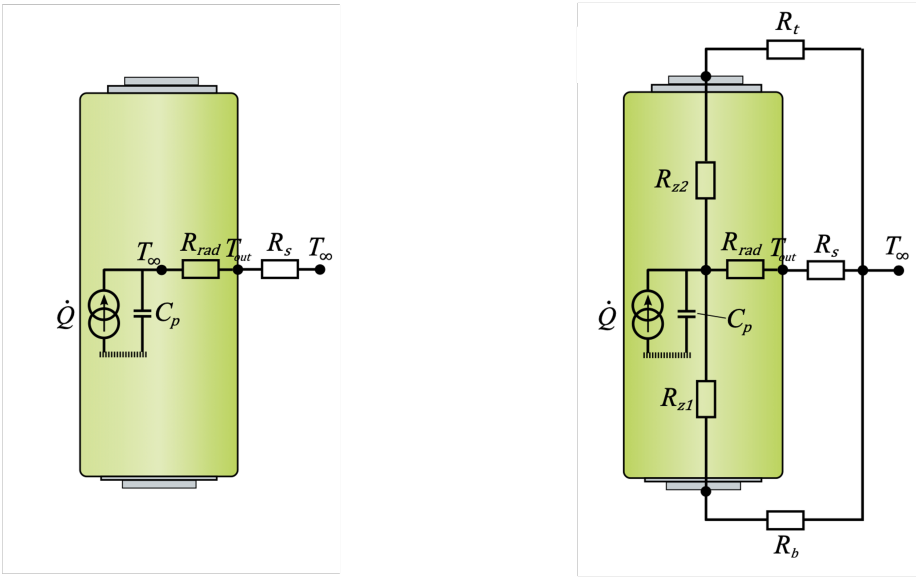

(a) (b)

Figure 1.3: Lumped thermal equivalent circuit model diagrams of a cylindrical cell a) 1D b) 2D from [52].

using a current source. Assuming uniform temperature throughout the cell, it can be modelled in 1D as showed in Fig. 1.3(a). If the lateral surface temperature is significantly different to the top and bottom of the cell, a 2D model is considered shown in 1.3(b).

The 1D approach has been used in multiple studies [53–56], and tested up to 6C with 1.5 °C temperature error [54].

A more complex, 2D equivalent circuit networks was presented by Zhao et al. [57] for a pouch cell, but temperature prediction error was higher than previously described 1D model in [54]. For the studied pouch cell, the authors assumed that the thermal gradient along cell width was negligible and only length and thickness dimensions were considered. The cell was discretised into a number of unit cells, and for each unit cell, an empirical thermal equivalent circuit network (ECN) model was derived. Each ECN contained an anode, cathode, separator, and current collector represented by individual resistances, while heat storage was modelled by an individual capacitance as shown in Fig. 1.4. The authors assumed that all material properties

were homogeneous. The use of multiple ECNs allows for modelling different thermal boundary conditions, which is particularly relevant for cell stacking and modelling pouch cell-tab connections, however, adds considerable complexity.

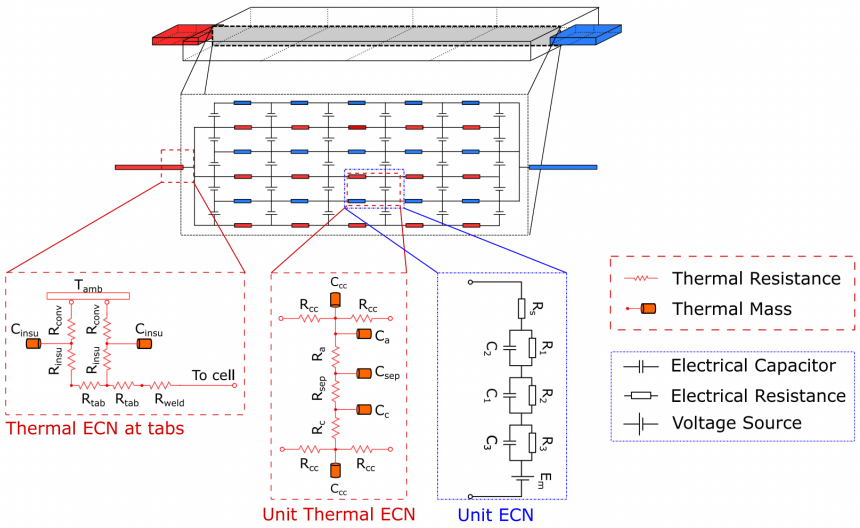

Figure 1.4: 2D thermal network ECN schematic from [57] of a pouch cell. Each ECN contains an anode, cathode, separator and current collector represented by an individual resistance, while heat storage is modelled by individual capacitance.

The model was tested at a 6C discharge current with tab cooling applied. While the simulation results were good near the tabs area, the model had the worst prediction in the middle of the cell surface with a maximum error of 2.3 °C. The authors concluded that the accuracy of the model is acceptable to investigate cell internal states. However, considering the application of EVs, an error in excess of 2 °C is rather significant. Additionally, thermal gradients across the cell width are likely to be non-negligible, implying that perhaps additional complexity of this model is in the wrong place and/or that spatially non-uniform thermal models are needed to obtain higher levels of thermal prediction.

1.2.4.2 Spatially non-uniform thermal models

Finite element method (FEM) is commonly used for numerically solving differential equations in engineering problems such as fluid flow, structural analysis, and also battery modelling. The cell geometry is divided into a finite number of elements, and for each element, FEM solves the partial differential equation, finding an approximate answer to the boundary value problem.

Cylindrical cell geometry

For a cylindrical cell, it is often assumed that the temperature varies only radially in space. This it because it was found that cell heat transfer resistance in the axial direction is twenty times lower than in the radial direction [58]. With this assumption, Hallaj et al. [59] used a simplified one dimensional model to describe the thermal dynamics of a cylindrical cell, where radial version of the heat equation takes form

$$\frac{\partial^2 T}{\partial r^2} + \frac{1}{r}\frac{\partial T}{\partial r} + \frac{\dot{q}}{k_{\mathrm{r,cell}}} = \frac{1}{\alpha}\frac{\partial T}{\partial t}, \tag{1.5}$$

where T is cell temperature, r is radial distance, $k_{\mathrm{r,cell}}$ is radial thermal conductivity, $\dot{q}$ is volumetric heat generation rate, and α is thermal diffusivity.

Pouch cell geometry

In a pouch cell, for each element, the spatial (x, y) temperature distribution is determined:

$$\frac{\partial^2 T}{\partial x^2} + \frac{\partial^2 T}{\partial y^2} + \frac{\dot{q}}{k} = \frac{1}{\alpha}\frac{\partial T}{\partial t}. \tag{1.6}$$

Considering the geometry of a pouch cell, although it is possible to model each cell layer separately, it is computationally expensive, and the variation across cell thickness is small (i.e. it is justified to assume uniform internal temperature across cell thickness if the Biot number is small [60]). Therefore, an alternative solution

was proposed, where cell layers are lumped in a homogenised pseudo-3D model [37]. Here, the cell consists of a single homogenised anode, cathode, and separator, where the thickness of an individual element is multiplied by the number of layers existing within the cell, as shown in Fig. 1.5.

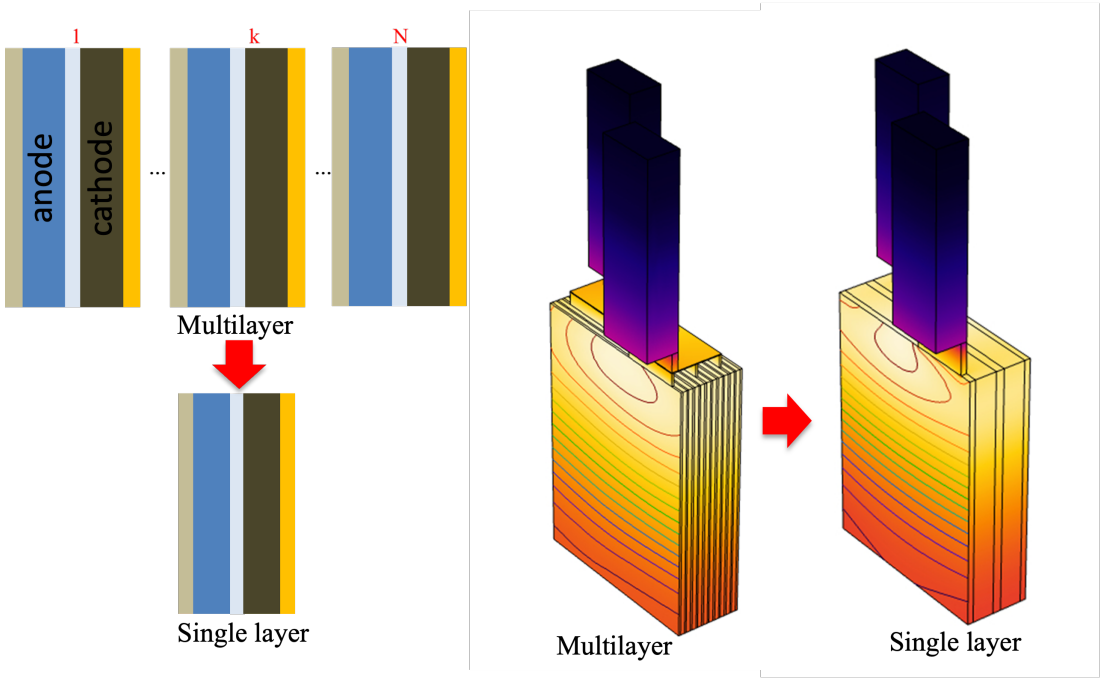

Figure 1.5: 3D model reduction from multilayer to single layer, adapted from Lin et al. [20].

This approach requires either detailed knowledge about the individual material properties used, or the cell's bulk properties, which increases parametrisation complexity. Nonetheless, this model was proven to provide good thermal prediction (0.2 K RMSE) in both x (cell height) and y (cell width) planes for 4C discharge [20]. Given that simpler models are unable to accurately reflect cell spatial temperature at higher C-rates, this lumped pseudo 3D model offers a good balance between model complexity and accurate physical interpretation. Although it has not been tested at higher C-rates, this modelling approach seems promising for EV applications.

1.3 Battery degradation

1.3.1 Degradation modes

Battery degradation can be caused by a number of factors, each resulting in a specific outcome. The primary contributing factors include high cycle count, operating at extreme temperatures, or operating at extreme currents and prolonged storage. Additional stress factors may include operating at high SOC level or high voltage level. The impact of the primary factors on degradation mechanisms and resultant modes (quantifiable symptoms of the degradation mechanisms) is illustrated in Fig. 1.6.

1.3.1.1 Loss of active material

Loss of active material (LAM) occurs on both the positive and negative electrodes of a battery, and it reduces the amount of electrode material available for the insertion or extraction of lithium. This can lead to a decrease in both capacity and power, known as capacity and power fade. However, the causes of LAM differ depending on the electrode. Both electrodes can experience LAM due to structural disordering and volume changes, which result in particle cracking and loss of electrical contact. Additionally, the anode may experience the buildup of a resistive surface layer, which limits access to active sites and exacerbates LAM [64]. On the other hand, the cathode may experience decomposition of electrode material, leading to the migration of species that contribute to further LAM. While both electrodes may experience volume changes, the most severe are reported for silicon, with $\sim$ 300-400 % volume expansion [65–67] during lithiation, followed by a contraction in delithiation. For comparison, graphite's total volume expansion from a fully delithiated to a fully lithiated state is around ($\sim$10%). These volumetric changes can stimulate particle cracking and subsequent contact loss, further exacerbating LAM.

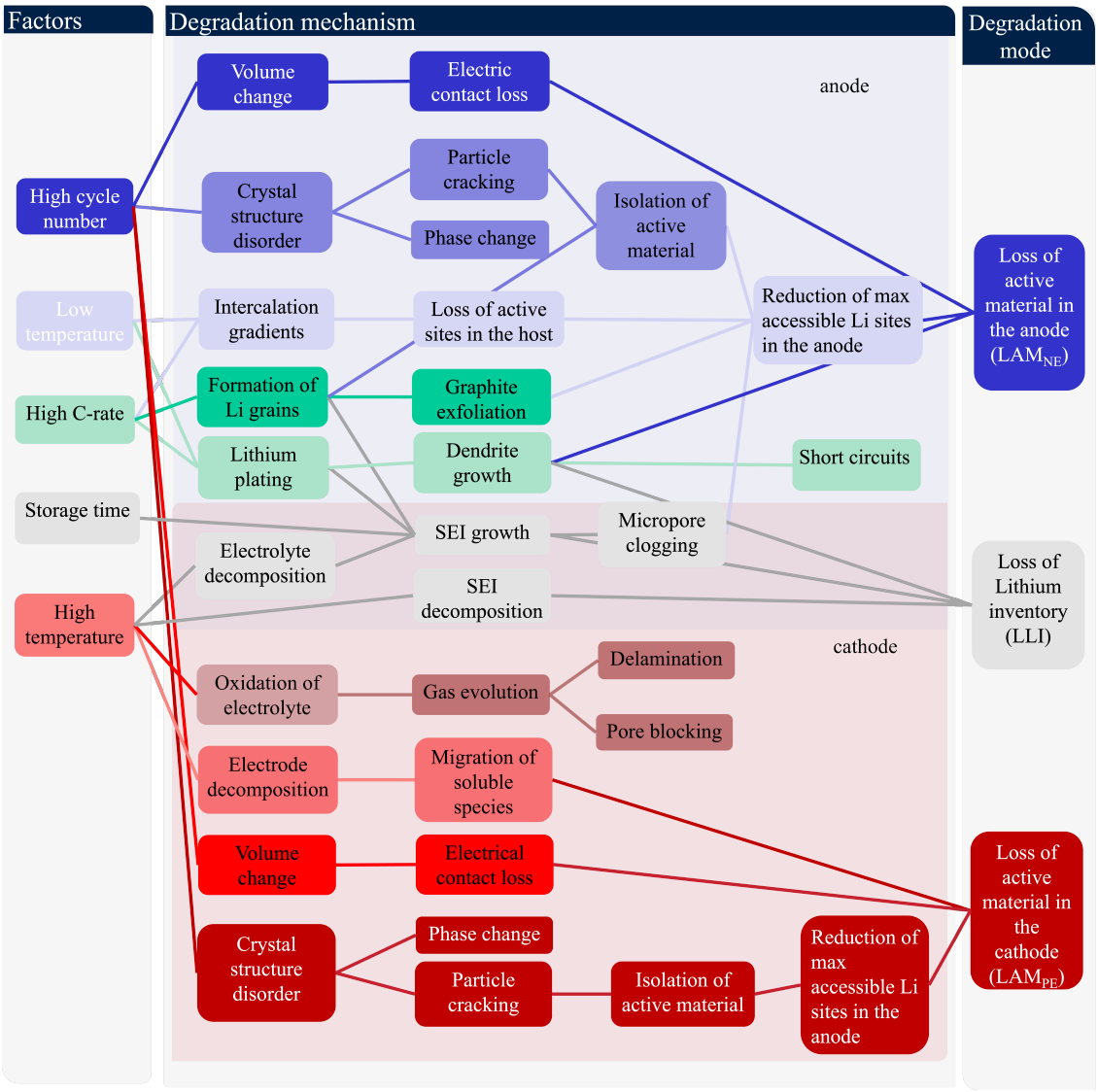

Figure 1.6: A diagram summarising the most relevant degradation effects, mechanisms and modes for this thesis based on a combination of [61–63].

1.3.1.2 Loss of lithium inventory

Loss of lithium inventory (LLI) occurs when lithium is either trapped within disconnected electrode material or consumed by parasitic reactions within the electrode, such as dendrite growth or solid electrolyte interphase (SEI). In both cases, the lithium becomes unavailable for further reactions. This can happen at higher current rates or at low temperatures. Low temperatures and prolonged storage can also promote the formation of a surface film, known as a SEI. The SEI is a thin layer that forms as a result of electrolyte decomposition on the surface of electrode particles, which blocks their porous structure. While the SEI allows for lithium-ion transport for continued electrochemical reactions [68], its buildup causes an increase in cell impedance and LLI. LLI is reflected as a respective stoichiometric drift visible on the electrode OCPs.

1.3.2 Degradation diagnosis methods

A variety of non-destructive methods have been reported in the literature for diagnosing battery ageing or state of health. The most established methods include incremental capacity analysis (ICA) [69–71], differential voltage analysis (DVA) [72] and EIS [73]. These methods, based on voltage response to an applied current are, understandably, limited in their analysis depth, but allow for the quantification of LLI and LAM in the electrodes. Another method proposed in the literature is entropy profiling [7,74–76], however it has not been explored in depth to assess its merit compared with the other techniques. Cell tear down and a post-mortem analysis allow for more detailed identification of ageing processes, such as lithium plating and changes in the active microstructure. However, these destructive diagnostic methods are limited in their application to laboratory settings.

1.3.2.1 Differential voltage analysis and incremental capacity analysis

Differential voltage analysis and incremental capacity analysis are based on differentiation of the voltage and capacity curves obtained near equilibrium conditions to quantify resultant peak shifts and classify degradation [77, 78]. The DVA technique considers dV/dQ as a function of Q, and ICA is calculated as dQ/dV and considered as a function of V, where Q is capacity and V is open circuit voltage. The method was first introduced in 2004 by Bloom et al. [79] who discovered that the main difference between the two derivatives is that the peaks in the dV/dQ curve represent phase transitions, whereas the peaks in the dQ/dV curve show phase equilibria.

According to the literature [80], a horizontal shift on a DVA curve is due to loss of cyclable lithium. Loss of active material in the positive electrode $Q_{LAM,PE}$ is calculated from the capacity difference between the characteristic cathode peak [80] and cell maximum measured capacity. Similarly, at the negative electrode $Q_{LAM,NE}$ is identified as the change in capacity between characteristic anode peak [80] and 0 Ah, while the shift between electrodes $Q_{balance}$ is the difference between the maximum capacity and $Q_{LAM,NE}$.

In the case of ICA, a horizontal shift towards higher potentials of ICA peaks indicates LLI. A decrease in the intensity of the ICA peaks indicates LAM [81], but it cannot be quantified and distinguished between individual electrodes as accurately as with DVA.

Dubarry et al. claim [77] that dQ/dV is more sensitive than dV/dQ for degradation analysis, as it shows the degradation signature on a voltage scale instead of capacity scale. For small amounts of capacity fade ($\sim$5 %) and very low currents (C/25), ICA signatures may not allow for distinction between the LLI and LAM mechanisms [77]. The performance of ICA is dependent on the battery chemistry, and for chemistries with significant phase change, e.g. LFP, the change in voltage (dV) is small. Both ICA and DVA are prone to measurement noise and their accuracy may be influenced

by sampling rate. For optimal results the sampling rate should be relatively high but not too high to avoid numerical conditioning problems when fitting ($< 1\,\text{Hz}$).

So far, the application of these methods to degradation has been based only on LAM/LLI quantification, without further interpretation [80, 82, 83]. Additionally, all these methods must be performed at constant temperature, however, temperature dependence also contains information relevant to degradation. Given that the electrochemical potential is a function of both concentration and temperature, neglecting one of these dependencies in ageing diagnostics is limiting.

1.3.2.2 Differential thermal voltammetry

Differential thermal voltammetry (DTV) refers to the simultaneous measurement of a cell terminal voltage and temperature during 1C (or similar) galvanostatic charge/discharge process, therefore addressing coupled electrochemical and thermal processes. Based on Eq. (1.7), the resulting dT/dV profile is then plotted against cell voltage.

$$DTV = \frac{dT}{dt} / \frac{dV}{dt} = \frac{dT}{dV} \tag{1.7}$$

Since the DTV method uses temperature as an input, it is important to minimise convective heat transfer and ideally insulate the cell to avoid biased thermal boundary conditions [84] to minimise signal noise. Similar to the ICA method, DTV reveals characteristic peaks, which can be used to interpret degradation mechanisms based on peak magnitude, shift, and width.

Merla et al. [85] studied the evolution of the two most dominant DTV peaks, and similarly to ICA, during ageing the peaks exhibited a steady shift towards lower potentials which was attributed to increasing impedance. However, they also noted that this shift could represent stoichiometric drift between the electrodes [85]. Since stoichiometric drift affects the potential window of combined electrodes, it is visible as a variation in the width of the peaks. The drift is caused by Li-ion loss and the

formation of new SEI, leading to a shift in anode stoichiometry towards lower lithium content and higher thermodynamic potentials.

Although DTV considers heat-generation dependency with battery age, and has a simpler experimental procedure than ICA/DVA, it is challenging to distinguish between degradation mechanisms. Moreover, DTV assumes that the SOC dependency linking voltage and temperature is negligible, which is not necessarily the case.

1.3.2.3 Electrochemical impedance spectroscopy (EIS)

Electrochemical impedance spectroscopy (EIS) is a technique that involves analysing a cell's voltage response to a sinusoidal current input signal. This can also be done in a potentiostatic mode [86]. The resulting impedance spectra are calculated over a range of frequencies (usually from around 10 kHz to 10 mHz), and are presented as a Nyquist plot, with the imaginary part plotted on the y-axis and the real part on the x-axis [87]. The resultant impedance spectra can be divided into four sections based on the frequency range, as depicted in Fig. 1.7.

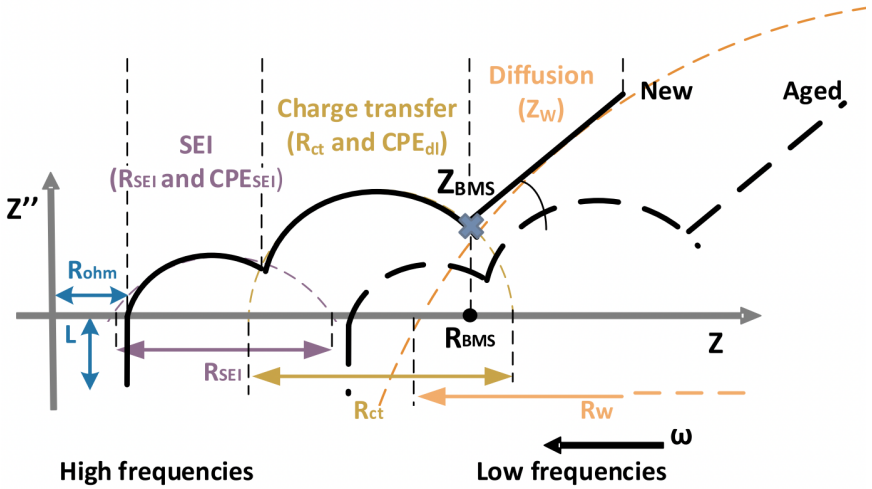

Figure 1.7: An EIS spectrum from [31] can be interpreted as follows: reading from left to right, starting with high frequencies, the intersection with the real axis represents the ohmic resistance (R_{ohm}). The first EIS semicircle corresponds to the SEI resistance (R_{SEI}), the second semicircle marks the charge transfer resistance (R_{ct}), and the characteristic tail signifies the diffusion process.

The first section of the spectrum represents high frequencies, characterised by inductive (L) behaviour. The point at which the spectrum intersects the real axis marks the ohmic resistance (R_{ohm}). The second section, represented by a smaller semicircle, gives information about the SEI resistance (R_{SEI}), while the larger semicircle marks the charge transfer resistance (R_{ct}), which is also associated with the double layer capacitance. At low frequencies, the spectrum exhibits a characteristic tail shape, which is indicative of diffusion processes, according to [86, 88–90].

Battery ageing is reflected in a horizontal shift of the EIS spectrum profile towards lower frequencies, making it an effective tool for the identification of state of health (SOH). EIS can be a quick procedure (25 min per cell [91]) and it can easily determine the parameters of equivalent circuit models, which cannot be obtained from DVA/ICA. However, EIS may be more time intensive if lower frequencies are used to extract diffusion information. Moreover, the accuracy of EIS results depends on the fitting procedure and model used. This means that the results may not be universally applicable and the estimation of SOH may be compromised, depending on the chosen model, as noted in [91]. Moreover, the challenge is that EIS is only valid for a linear time invariant system, but batteries have nonlineratities and nonstationarities.

1.3.2.4 Entropy profiling

Entropy profiling, i.e. the measurement of entropy changes, is another method proposed for the analysis of battery degradation [7, 74–76]. Entropy change is conventionally measured using calorimetry, or a potentiometric method.

Calorimetric entropy measurement Calorimetric entropy profiling involves sequentially charging and discharging a cell within a closed, insulated container that is matched to the cell size. The heat generated during the process is calculated based on the recorded temperature change, given the known heat capacity (C_{p}) of

the calorimeter.

$$Q_{\text{total}} = Q_{\text{irr}} + Q_{\text{rev}} \tag{1.8}$$

The challenge for calorimetric entropy profiling lies in isolating and measuring the heat flow sources, which are reversible (Q_{rev}) and irreversible (Q_{irr}) in nature, as defined in Eq. (1.8). Instead of directly attempting separation of individual terms, a total thermal energy is recorded with the calorimeter over the full charge-discharge cycle. The reversible heat flow changes direction depending on the current direction, so the integration of the measured thermal power over a complete cycle results in the cancellation of the thermal energy associated with entropy changes, as described in [92]. In this way, the irreversible heat can be isolated, assuming it consists of polarisation and parasitic contributions. The polarisation thermal energy can be determined by integrating the hysteresis voltage curve obtained during the charge/discharge process. The polarisation heat term refers to the overpotential multiplied by the current [93]. Then the parasitic losses can be calculated by subtracting the polarisation heat from the total heat measured by the calorimeter, as described in [92]. In other words, for a closed cycle, the reversible work is eliminated and the entropy is calculated by subtracting the actual work from the total heat term. Downie [94] argues that to minimise the electrical losses, the method should be performed at low current and high temperature, as polarisation dominates heat generation. The measurement time is significantly shorter than the potentiometric method, because relaxation phases following each charge/discharge cycle are avoided. Schmidt et al. states that the accuracy of calorimetric readings tends to be lower than potentiometric method [73]. However, Krause et al. demonstrated that high accuracy (1 µW) can be achieved with the calorimetric measurement [92].

Potentiometric entropy measurement Potentiometric entropy measurement is a passive and discontinuous method in which cell is subjected to temperature variation

at a fixed SOC. As a response to the temperature variation, the cell terminal voltage changes, and the relationship between voltage change and temperature change may then be used to calculate entropy change ΔS at individual SOC levels.

Thermal equilibration times used in entropy profiling range between 2.5 h to 60 h, with 12 - 54 h relaxation times being most common [95–98]. Zhang et al. [76] investigated the impact of the relaxation time on the accuracy of entropy change measurement and found that longer relaxation times could enhance accuracy. On the other hand, Thomas et al. [99] pointed out that longer relaxation times could introduce errors due to battery self-discharge. Given the very long test durations, often a compromise is found by decreasing the number of SOC points, thus sacrificing measurement resolution. Although justified, this may hide certain entropy features.

Entropy profiling used for degradation diagnosis Maher and Yazami [75] explored the effect of cycle ageing on a LCO/Gr cell and discovered changes in the entropy profiles related to a decrease in battery capacity. However, no clear trend was observed in the entropy change profiles. Sullivan et al. [74] conducted a study on an LCO half-cell and observed that, with prolonged cycling, the distinctive entropy profile features (maximum and minimum) of LCO became less pronounced. Sullivan et al. attributed changes in the entropy curves to alterations in lithium ordering caused by ageing. Zhang et al. [76] and Osswald et al. [7] also performed entropy profiling for aged cells, but neither study provided an explanation for the changes in entropy features with ageing.

1.4 Summary and gap analysis

This chapter explored the requirements and challenges faced by electric vehicles and conducted a thorough examination of state-of-the-art methods to identify areas for potential improvement and development. The challenges faced by electric vehicles

include conflicting design requirements: vehicles are to be charged quickly, yet have a long driving range on a single charge. On top of the usual battery degradation effects due to storage and driving, the use of excessive C-rates motivated by fast charging exacerbates degradation processes, leading to decreased battery performance and shorter useful life.

A comprehensive solution to these pressing challenges requires a multi-faceted approach that considers both cell design and materials science, as well as BMS optimisation and control. While a solution encompassing all aspects would be ideal, the scope of this work is focused on cell diagnostics and improved modelling to boost BMS capabilities. Cell modelling is making significant progress towards maturity, but the three aspects still pose a challenge:

- accurate diagnosis of battery ageing,
- effective inclusion of predicted degradation within a BMS,
- accurate prediction of internal battery states at high current rates (fast charge).

All three aspects are closely linked to the understanding of the electrochemical processes accompanying the cell reactions at various timescales (dynamic and ageing) and their integration is crucial for optimised BMS development.

Gap 1: Accurate diagnosis of battery ageing: Li-ion battery degradation mechanisms have been comprehensively studied in the literature and their classification into LAM and LLI modes is clear. However, the origins of some of these mechanisms are not well defined or fully understood. DVA is based on differentiation of cell OCP vs. capacity, which when plotted produces a curve with characteristic features relating to phase transitions. The evolution of such features may be tracked through battery cycle life, allowing for quantification of LAM and LLI. Entropy profiling uses a similar concept, but this time the OCP is differentiated with respect to temperature,

which provides additional information about battery thermodynamic behaviour. By combining both temperature and concentration dependencies, entropy profiling has the potential to provide more information about battery ageing to DVA/ICA. The inclusion of thermodynamic behaviour has the potential to elucidate morphological changes experienced throughout battery life, which is not possible with the existing non-destructive techniques. However, the available literature on this topic is limited, and the full capabilities of entropy profiling have yet to be explored.

Gap 2: Effective inclusion of predicted degradation within the onboard BMS The current limitations of predictive models and state observers result in an under-utilisation of lithium-ion batteries [100]. As the battery ages, these uncertainties become more pronounced, because traditional predictive models rely on parameters that are extracted from a brand new cell. Conventionally, degradation effects are incorporated into existing models by coupling them with specific degradation mechanism models. However, this method increases the complexity of the model and demands accurate assumptions, prior knowledge, and quantification of specific degradation mechanisms. Although this approach provides insights into degradation processes, the practical application in electric vehicles calls for a less complex approach. A good alternative for a BMS could be periodic numerical parameter re-evaluation over battery life instead of inclusion of separate 'open loop' degradation models. In this way, the accuracy of model predictions could be maintained over battery life. An SPM could be a good candidate for this application, given its relative simplicity and fair accuracy of physical processes, which could be useful in degradation analysis.

Gap 3: Accurate prediction of battery internal and measured states at high current rates The consensus in the literature seems that the reduced physics based model, the SPM, works well for low C-rates, but with an increase in applied current, the lack of electrolyte dynamics hinders model accuracy. Therefore, the

SPMe and DFN models, where electrolyte dynamics are included, are often preferred for higher C-rates. However, the additional complexity of these models may be in the wrong place. Instead of adding more transport mechanisms, it has been shown that long-range temperature variations, and temperature dependency of parameters, is particularly important for predicting large pouch cell behaviour [37]. With C-rate increase, the literature becomes scarce and presents worsening results, where large error becomes visible especially for temperature prediction. While the definition of "high current" is dependant on cell design (i.e. power vs. energy cell), the limiting conditions might be triggered sooner or not reached at all.

Is it possible then to model accurately internal states of the cell at high C-rate conditions with current battery models if the limiting condition is not reached? Is there an additional current dependency/dynamics that becomes more prevalent with C-rate increase that state-of-the-art models do not account for? To investigate this problem, a high-fidelity multi-physics model is considered and compared to experimental data with charging up to 10C.

1.5 Thesis outline

Chapter 1 (Challenges and opportunities in battery management systems for electric vehicles) highlights the three crucial challenges in the use of batteries in electric vehicles: accurate battery health diagnosis, effective integration of diagnosed degradation into onboard BMS, and precise modelling of both electrochemical and thermal processes under high C-rate conditions. To optimise battery performance in EVs, these challenges must be addressed through a comprehensive understanding of battery behaviour. The following chapters delve into each challenge, seeking to find optimal solutions applicable for BMS to enhance an EV performance.

Chapter 2 (Entropy profiling for the diagnosis of battery health) exam-

ines battery degradation from a thermodynamic perspective. It aims to determine if entropy profiling, a method not yet fully explored in literature, can provide additional insights into degradation. The chapter focuses on ageing entropy results for a Si-doped cell (NCA/Gr-Si), a composition that has gained attention due to its improved capacity capability. It also examines the specific impact of Si doping on battery degradation behaviour. The results show that entropy profiling can offer the same information as DVA and ICA regarding degradation mechanisms, but also provides information about particle morphology changes.

Chapter 3 (Electrochemical and thermal degradation modelling) explores the correlation between degradation modes and SPM battery parameter variations. It investigates if periodic parameter updates throughout battery life can replace explicit degradation models, thus improving internal state estimation without adding complexity to the existing model. Additionally, the chapter delves into the impact of ageing on cell heating, examining both reversible and irreversible heat contributions.

Chapter 4 (High C-rate thermal model) investigates performance of a 3D multi-physics continuum model that is simulated across a range of C-rates, from 2C to 10C. Parameter optimisation procedure is introduced and special focus is placed on the solid diffusion parameter and its subsequent relevance to the model. The study further discusses this topic in relation to cell-level limiting factors.

Chapter 5 (Conclusions) Summarises the findings from previous chapters, identifies the limitations, and highlights potential areas for improvement and future work.

Chapter 2

Thermodynamic changes accompanying battery degradation

The previous chapter gave an overview of current challenges faced by EVs. This chapter aims to address the degradation diagnosis problem from a thermodynamics perspective, specifically to test the hypothesis that more information about battery degradation can be obtained in a non-invasive manner using entropy measurements compared to current state-of-the-art methods such as ICA/DVA. Entropy change measurement—which probes the response of the OCP to temperature—offers a unique battery diagnostics tool. While entropy change measurements have previously been applied to study degradation, the implications of Si negative electrode additives on the entropy profiles of commercial cells have not been explored, and this chapter aims to fill this gap. Additionally, it is shown that entropy profiling is capable of tracking ageing markers in the same way as DVA. In addition to high OCP hysteresis of Gr-Si blends, entropy hysteresis is also observable. Changes in the entropy profile reflect degradation-related morphological changes over battery life.

2.1 Literature review

2.1.1 Entropy origins

The Gibbs free energy (G) expresses the capacity for 'useful work' that can be obtained from a cell under constant temperature and pressure. It is linked to entropy (S) and enthalpy, (H) through a well established relation

$$G = H - TS, \tag{2.1}$$

where T is temperature. For battery systems, Gibbs free energy of reaction is determined from its reactants (subscript R) and products (subscript P) contributions:

$$\Delta G = \sum_{n=1}^{n_{\mathrm{P}}} v_{\mathrm{P}i}\mu_{\mathrm{P}i} - \sum_{n=1}^{n_{\mathrm{R}}} v_{\mathrm{R}i}\mu_{\mathrm{R}i}. \tag{2.2}$$

Here, v is the stoichiometry, μ is the electrochemical potential and n is the number of reactants/products.

The equilibrium potential (E_{OCP}) of the intercalation electrode is given by differencing the electron electrochemical potentials $\Delta\mu = \mu_{\text{e-}}^{\text{cathode}} - \mu_{\text{e-}}^{\text{anode}}$ [101]

$$E_{\mathrm{OCP}} = \frac{\Delta\mu}{nFz_{\mathrm{e}}}, \tag{2.3}$$

where $n = 1$ is the number of electrons transferred in the reaction, $z_{\mathrm{e}} = -1$ is the charge of an electron.

The entropy of reaction is denoted as (ΔS) here, and may be related to cell open circuit potential according to

$$\left.\frac{\partial\left(\Delta S\right)}{\partial x}\right|_{p,T} = nF \left.\frac{\partial E_{\mathrm{OCP}}}{\partial T}\right|_{p,x}, \tag{2.4}$$

where x is the extent of the reaction (degree of lithiation in the insertion electrodes),

which can also be represented as $x = Q/Q_0$, where Q is the stored charge in the cell and Q_0 is the nominal capacity of the cell. p denotes pressure, which is usually assumed constant for battery systems. Throughout this thesis entropy change for a full cell will be referred to as ΔS.

Mechanical effects are often neglected in the majority of electrode materials, but in the specific case of silicon they are likely important due to its high volumetric expansion during charging [67]—this aspect will be discussed later in this chapter together with its implications. Abrupt energy changes accompanying first-order phase transitions result in rapid changes in OCP gradient at these points. Since phase change is always associated with changes in thermodynamic properties, it might be reasonably expected to see correspondence between features present in DVA and also features in entropy of reaction changes with respect to stoichiometry.

In a stable, fully-reversible charge-discharge cycle, the result of the integration of entropy change around a closed cycle would be zero. However, according to the second law of thermodynamics, for a real battery system, a charge-discharge cycle cannot be thermodynamically reversible above 0 K. Assat et al. [102] identified that entropy production relates to the observed voltage hysteresis. Therefore, in addition to the hysteresis measured in OCP curves, one also measures a hysteresis associated with entropy measurements [102–104]. This source of hysteresis is always present in a metastable system [102].

2.1.2 Deriving the link between entropy profiling and DVA

The variation of partial molar entropy (also referred to as entropy change), as defined in Eq. (2.4), is predominantly determined by lithium/vacancy configurations and is thus sensitive to the host electrode microstructure [105–108]. When a phase transition occurs, it is often accompanied by a sudden change in the slope of the open circuit potential curve, which may be referred to as a 'discontinuity' in the graph. Since

the open circuit potential is a function of both lithiation and temperature, the discontinuity propagate across both dimensions. In DVA, which is a measure of voltage change with respect to capacity change (dV/dQ), this 'discontinuity' (sudden change in voltage slope) is used to identify phase transitions. By calculating entropy change with respect to capacity change, the same phase transitions as visible in DVA should be detectable from the $d\Delta S/dQ$ curve. This means that measuring entropy changes and their variation with cycle direction may allow the tracking of structural defects and volume and ordering changes dependent on ageing conditions. The complete derivation of the relation between the DVA and entropy change is demonstrated in Appendix 5.2.2.

2.1.3 Accelerated entropy measurement

Reaction entropy in a battery is conventionally measured either with calorimetry or by a potentiometric method as described in chapter 1, section 1.3.2.4. As an alternative to the long-duration potentiometric method, an accelerated entropy measurement method has been presented by Osswald [7]—the principle is similar to the potentiometric method, but the relaxation time is considerably reduced. The cell is brought to a desired SOC, allowed to rest for only ~ 15 min, and then subjected to a temperature change. To promote faster heat exchange from the environment to the cell, the cell is placed in a copper cell holder with high thermal conductance. Given that entropy is estimated from the voltage/temperature slopes, Osswald [7] states that it is not necessary to know the exact equilibrium OCP, thus heavily reducing the rest times. For this assumption to work, three conditions must be met. Firstly, the 15 min rest period following temperature change must be sufficient for homogeneous temperatures within the cell. If the thermal conduction medium or size of the battery were to change, it is likely that the 15 min interval would be no longer optimal. Secondly, a background voltage subtraction method is used to remove the

voltage relaxation characteristic from the temperature-induced changes. This is done by fitting a simple function to the voltage profile before and after the temperature variation. There is no need for deeper interpretation of the simulated OCP curves themselves. However, to capture the correct OCV relaxation dynamics, an appropriate initial observation window needs to be selected. The time required is dictated by the chemistry of the cell and the coating thickness of the individual electrodes to account for different diffusion paths. The estimated voltage is subtracted from the measured voltage, which is computed for each temperature change. The gradient of the line joining the identified points is the resultant entropy. Osswald et al. [7] states that the subsequent reduction in time does not sacrifice entropy measurement accuracy, however the comparison with the literature is inadequate given insufficient examples and widely different results have been presented [109, 110].

2.1.4 The effect of silicon addition in a graphite anode

An introduction of silicon to the anode material presents additional challenges for characterisation because of the much greater OCP hysteresis found during lithiation/delithiation of silicon than in pure graphite anode materials [78, 111, 112].

While for graphite the total volume expansion from a fully delithiated to fully lithiated state is small ($\sim$ 10%), and confined to one crystallographic axis [113, 114], silicon is reported to experience $\sim$ 300-400 % volume expansion [65–67] during lithiation, followed by a contraction during delithiation. Sullivan et al. found that particle cracking, and hence a decrease in the mean active particle size, leads to visible changes in entropy curves [74]. This finding suggests that there could be an association between particle size and entropy profile features. In the case of silicon, therefore, the large changes in volume during lithiation/delithiation could be associated with changes to the measured hysteresis during cycling.

Vorauer et al. [115] used post-mortem small-angle neutron scattering which pro-

duces intensity versus scattering vector (Q) plots to visualise the (de)lithiation structural changes of an amorphous silicon (a-Si) /crystalline iron-silicide graphite composite anode. They observed no nanoscale swelling of a-Si with cycling after lithiation. However, anode delithiation was followed by a high-Q intensity decrease due to a-Si shrinkage that did not reverse back to its initial value. Instead, the intensity in the aged sample remained slightly higher than the pristine sample, which means that the a-Si phase remained more expanded [115].

The rate of SEI growth is higher in silicon-doped anodes [116] than in anodes without silicon. The change in silicon particle size with cycling exerts a mechanical strain on the SEI layer, causing cracking and exposure of fresh active material to the electrolyte [117]. Furthermore, neutron reflectometry studies performed by Veith et al. [116] indicate that the SEI on silicon restructures during lithiation/delithiation. During delithiation, Si particles contract and the SEI becomes dispersed in the matrix pores, leading to a lower electrical conductivity and more limited access of Li to the active particles.

As a consequence of these irreversible volume changes during lithiation/delithiation, the hysteresis in the OCP and entropy change are both expected to vary with cycling ageing. During calendar storage, where no repetitive volumetric changes occur, the hysteresis is expected to remain stable throughout life.

2.1.5 The impact of battery ageing on entropy

At the lab scale, various non-invasive techniques can be used (and combined [118]) for classifying the above-mentioned degradation modes. One of the methods monitors electrode slippage, which refers to the shift in the capacity of the anode versus cathode OCPs relative to their alignment in a pristine cell [79, 119]. It is also common to differentiate voltage vs. capacity curves obtained near equilibrium conditions to quantify peak shifts in dV/dQ vs. Q and classify degradation [77, 78]. These methods are

known as differential voltage analysis, defined as dV/dQ versus Q, and incremental capacity analysis, calculated as dQ/dV versus V. These are well-established methods for degradation mechanism identification [77, 78]. However, so far the application of these methods has been based only on LAM/LLI, without further microstructural interpretation [80, 82, 83]. Additionally, all these methods are performed at constant temperature, however, temperature-dependent results also contain information relevant to degradation. Given that the OCP is a function of both concentration and temperature, neglecting one of these dependencies in ageing diagnostics is limiting. In this regard, thermal and voltage analysis, obtained e.g. via differential thermal voltammetry (DTV), can provide an insight into ageing mechanisms [84]. However, the resultant curves depend on galvanostatic cycle rate and hence it is non-trivial to interpret them from a microstructural perspective.

Additionally, just as voltage versus SOC data has been shown to depend on cycling direction [78, 102, 103, 111, 112], the partial molar entropy (or entropy change) related to the variation of the OCP with temperature also shows a directional path dependency [102, 103]. This type of hysteresis is found even in half cell studies of lithium (de)insertion from graphite anodes [103, 104]. The addition of silicon or silicon suboxide (SiOx) to graphite to form a blended anode material leads to greater OCP hysteresis than in graphite-only anodes [78, 111, 112]. A greater mass fraction of SiOx leads to an even greater observed hysteresis [66]. The physical relationship between OCP hysteresis and entropy has been shown by Assat et al. [102] for a single cell chemistry at the beginning of cell life, but the entropy hysteresis might also depend on the long-term history of the cell and related microscopic changes due to ageing.

The specific case of LCO cathodes has been comprehensively studied by Sullivan et al. [74] who revealed that the entropy profile shape and characteristic regions did not change when a substantial proportion of cell capacity was removed. This means

that the intercalation mechanisms in the aged cell remain the same. Since there are no fundamental changes in the structure and thermodynamics of the materials, the degradation is likely caused by increasing kinetic (ohmic and transport) barriers to lithiation and delithiation of Li_xCoO_2. However, with cycling, there was a gradual decrease in the the entropy curve magnitude. This is likely caused by the growth of a passivating layer on the electrode, and by particle breaking and cracking, which in turn increases ohmic resistance. Also Zhang [76] documented a clear decrease in the entropy magnitude between fresh and cycled LCO cathodes, but his work did not focus on degradation mechanisms.

Calendar ageing promotes different ageing mechanisms than cycling ageing [64], but due to the long duration of calendar ageing tests, they are usually performed at elevated temperatures to accelerate the ageing process. Higher temperatures may lead to different degradation paths—such as electrolyte decomposition and diffusivity changes as well as LLI in the anode and LAM in the cathode. The pores in the active material may become clogged, reducing the number of accessible sites in the host material [62], which could also alter the entropy profile. Osswald et al. [7] showed that for NCA/Gr cells stored at 60 °C and 100 % SOC for 224 days, measured entropy preserved its shape and increased slightly in magnitude.

2.1.6 Research hypothesis

The hypothesis is that entropy profiling is a unique non-invasive battery diagnostic tool that provides the same information about ageing as DVA, but can elucidate morphological changes experienced by a battery throughout its life. This hypothesis is tested here by extracting and comparing entropy profiles from pristine, accelerated calendar-aged, and cycle-aged cells. The case of a silicon-doped anode is particularly interesting from the thermodynamic point of view, given its large volume variation during (de)intercalation.

2.2 Experimental

2.2.1 Methods

Commercially available Li-ion cells (Samsung 35E3) with high silicon content (∼10 wt % Si and ∼90 wt % Gr) were used, with specifications given in Table 2.1. All cells tested were from the same manufacturing batch, purchased in 2018. Screening tests at beginning of life for the entire group of cells (178 units) revealed a mean discharge capacity of (3.40 ± 0.01) Ah, measured at C/3 and 23 °C. The cells were divided into two groups of three cells each. The first group was stored at elevated temperature to act as an accelerated calendar ageing example, while the second group underwent cycle ageing tests.

2.2.2 Experimental setup

2.2.2.1 Full cells

A high-precision battery tester (HPC 10, Battery Dynamics) was used for battery cycling, with NTC (5 kΩ) thermistors mechanically attached to the cell surfaces using O-rings for temperature recording. For temperature control, all cells were submerged in a thermostatic bath (Corio CD 900F, Julabo) filled with polydimethylsiloxane (PDMS, H5 bath fluid, Julabo) [120].

Table 2.1: Samsung 35E specifications.

Cell model	INR18650-35E
Cathode chemistry	$LiNi_{0.8}Co_{0.15}Al_{0.05}O_2$ (NCA)
Anode chemistry	Gr-SiO_x (∼10 wt % SiO_x and ∼90 wt % Gr)
Nominal capacity	3.4 Ah
Cut-off voltage	4.2 V/ 2.5 V

2.2.2.2 Half-cells

To investigate individual electrode entropy contributions, several half cells were manufactured. A pristine full cell was fully discharged to 2.5 V at C/25 constant current and disassembled in an Argon-filled glove-box (MBraun). The harvested electrode material from the anode and cathode foils was punched into 16 mm diameter discs and re-assembled into coin cells with metallic lithium discs (Xiamen Tob New Energy Technology) as the other electrode, using pre-dried LP30 (Sigma Aldrich) as electrolyte and glass microfiber filters (grade GF/F, Whatman) as separators.

Electrochemical characterisation for the anode and cathode half cells was performed using a BaSyTec CTS cycler. Experimental measurements were performed using aluminium heat exchangers, in direct thermal contact with the coin cells, which were connected to a Julabo F12 refrigerated heating circulator, allowing direct control over the cell temperatures. This setup enabled more rapid thermal equilibration of the cells than would be possible using a climate chamber. Cell temperatures were monitored with type-T thermocouples. A Keysight 34972A data acquisition system with multiplexer unit was used for high resolution (22 bit) voltage and temperature measurements, assisting post processing of entropy profile data, as described in previous publications [7, 103, 108, 121, 122].

All half cells were allowed a 24-hour rest period following manufacture, to ensure proper wetting of the electrodes. For the anode half cells, three consecutive cycles at cycle rate 27 mA/g (normalised to the mass of active material of each electrode) were undertaken for loading and conditioning, at 25 °C. Subsequent to the galvanostatic cycles, cells were subjected to constant current constant voltage (CCCV) protocols at 25 °C. Anode half cells were discharged at 27 mA/g until reaching a cell voltage of 0.005 V vs. Li, and were subsequently held at 0.005 V for 2 hours. After manufacture and rest, cathode half cells were cycled three times at 13.5 mA/g, followed by CCCV at 13.5 mA/g, terminating at 4.3 V vs. Li for 2 hours. Both sets of half cells then

underwent an accelerated entropy measurement (described in section 2.1.3).

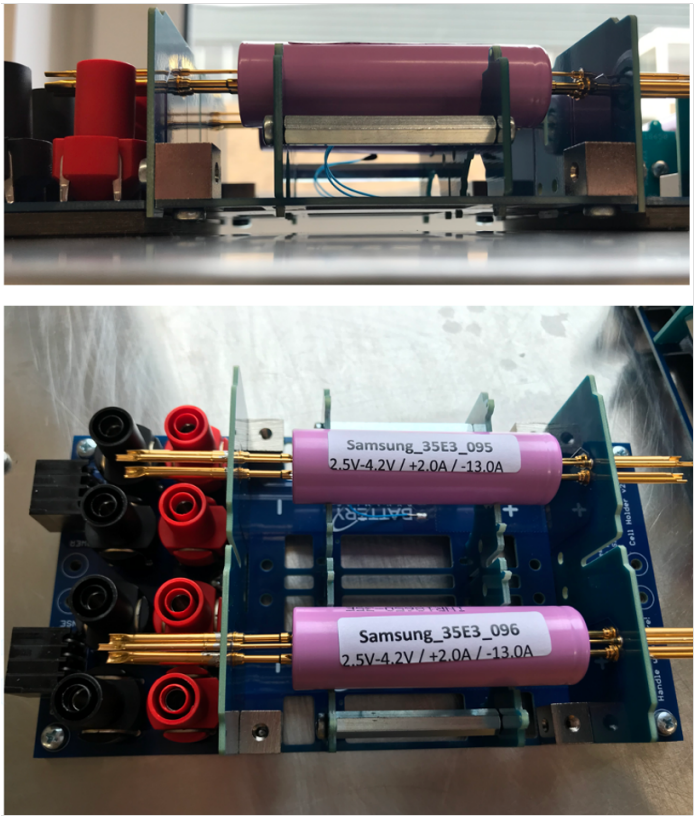

Figure 2.1: Samsung 35E 18650 cylindrical cells.

2.2.3 Accelerated ageing procedure

The first group of full cells experienced one year of calendar ageing at 75% SOC and 45 °C and the second group underwent continuous cycling (up to $\sim$ 720 cycles) with 2 A constant current charging until 4.2 V and 2 A constant current discharging until 2.5 V at 45 °C.

Both groups of full cells (calendar and cycle aged) underwent periodic characterisation tests called reference performance tests (RPTs) to record capacity and pseudo-OCV data. Each RPT consisted of a full charge and discharge at C/20 at 23 °C, followed by a non-isothermal galvanostatic intermittent titration technique (GITT) for accelerated entropy measurement. The non-isothermal GITT procedure is described in section 2.1.3.

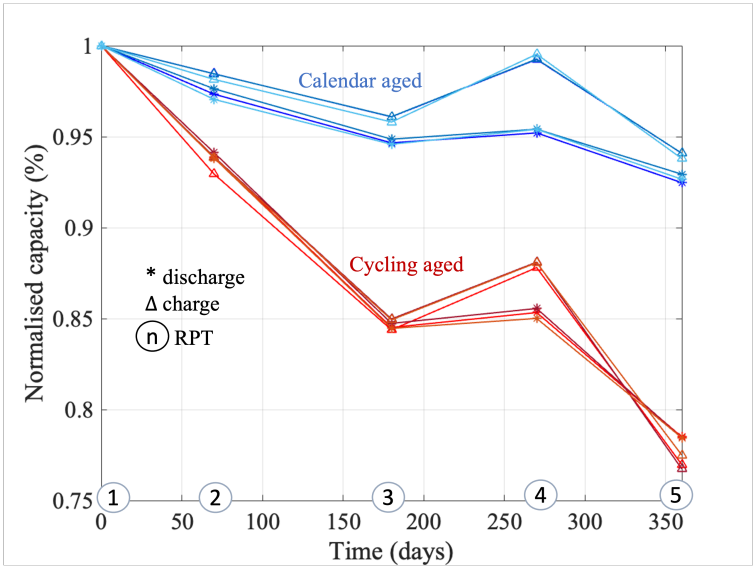

Figure 2.2: Observed capacity loss through RPTs for calendar and cycle aged cells for charge and discharge. The encircled numbers 1-5 in the figure refer to the RPT number. All cells experienced a 3 months rest period at 23 °C and 50% SOC between RPT3 and RPT4 due to COVID-19 lab closure.

Fig. 2.2 shows the capacity fade in both the calendar and cycle aged groups, measured by the RPTs. Due to a lab closure caused by COVID-19, all cells experienced an unplanned rest period of 3 months at 50% SOC and 23 °C. The resulting capacity recovery between RPT3 and RPT4 is shown in Fig. 2.2; the implications of this effect for the interpretation of the results is discussed later in the text.

2.2.4 Entropy estimation

To investigate entropy changes during battery ageing, an accelerated measurement method proposed by Osswald et al. [7] was used. Compared to the conventional potentiometric method, which requires up to 30 h relaxation time per SOC point [76], the accelerated method proposed by Osswald et al. [7] shortens this to 2.5 h per SOC evaluation.

The accelerated entropy measurement method uses curve fitting to correct for small changes in the open circuit voltage as it equilibrates, thus decreasing the re-

quired rest times. (As an aside, it is not possible to obtain the true equilibrium potential over a practical timescale anyway [103, 111, 113, 123–125]; this means we can, at best, probe metastable behaviour). To avoid measurement artefacts, two steps were taken. Firstly, the initial rest period of 20 min following a temperature change was sufficiently long to ensure uniform cell internal temperature. Secondly, the background voltage change was subtracted from the temperature-induced changes [7]. In our case, for full cells, 63 titration steps were used (0.3 A current between steps) during both charge and discharge excursions including subsequent 80 min of relaxation, until the potential reached the respective cut-off voltage. During the GITT relaxation steps, temperature jumps to 28 , 25 and 22 °C were included, shown in Fig. 2.3. To promote rapid and uniform heat exchange with the environment, the cells were submerged in a non-conductive silicone oil thermal bath instead of the copper cell holder originally used by Osswald et al. [7].

For half cells, the same GITT relaxation steps and temperature profile were used as for the full cells. During titration steps, the current of the cathode half cells was set to 13.5 mA/g (discharge) and the anode half cells was set to 27 mA/g (charge), to account for the factor of ≈ 2 difference between anode and cathode half cell capacity.

The entropy estimation method followed five steps described below.

Step 1 The objective is to simulate the voltage relaxation profile with data provided only at the beginning and end of the relaxation phase. Two training datasets are used. The first training data set is taken between 25-50 % of the initial relaxation time, that is from the 5th to 15th minute after the current was stopped. The second data-set uses (80 to 100 %) of the total relaxation time, that is 75th to the 80th minute. Simulation training intervals are marked with red stars in Fig. 2.5(a). The time intervals were modified from the original Osswald et al. [7] method to capture the slow dynamics of

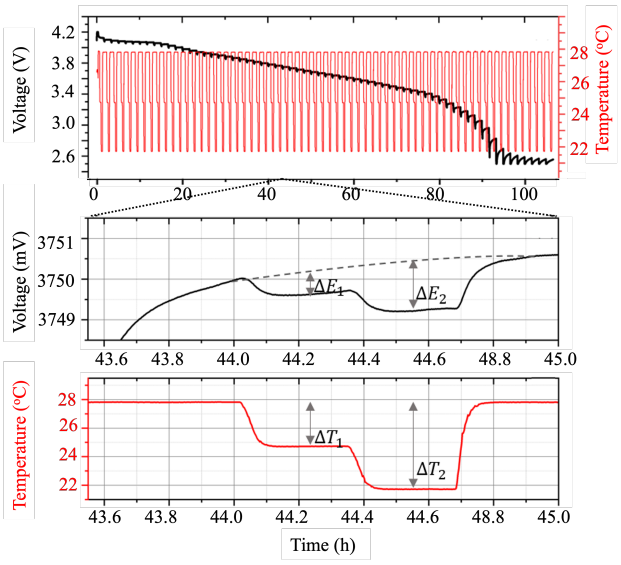

(a)

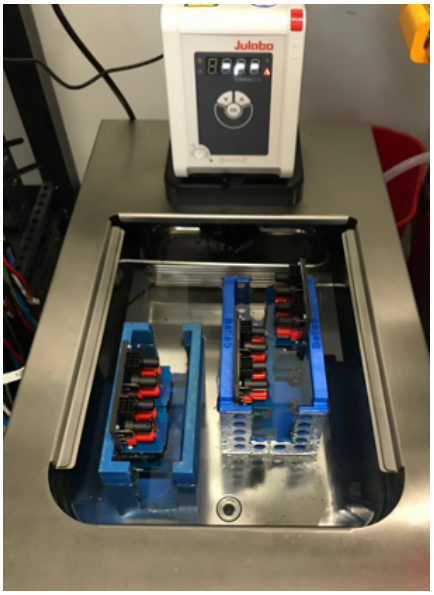

(b)

Figure 2.3: Accelerated entropy profiling experiment during a complete discharge (a). Zoomed regions indicates the deviation of the cell terminal voltage from the expected value (dashed line), caused by the temperature-step. Experimental setup showing the location of the cells in the direct-cooling apparatus is shown in Fig. (b).

investigated cell.

Step 2 Having established the training data-sets, the MATLAB curve fitting toolbox was used to fit the simulated voltage for each SOC point of data. Three different methods were considered when fitting the voltage curves, with results for all methods shown in Fig. 2.5(a) and (b).

$$\text{Method 1:} \qquad E_{\text{OCP,est}} = a + b \cdot \ln(t) \tag{2.5}$$

$$\text{Method 2:} \qquad E_{\text{OCP,est}} = a \cdot e^{-b \cdot t} + c \tag{2.6}$$

$$\text{Method 3:} \qquad E_{\text{OCP,est}} = \frac{a \cdot t}{b + t} + c \tag{2.7}$$

Here, a, b, c are adjustable parameters and t denotes the time index; $E_{\text{OCP,est}}$ is the estimated open circuit potential.

Method 2, described by Eq. (2.6), was selected as the most accurate based on

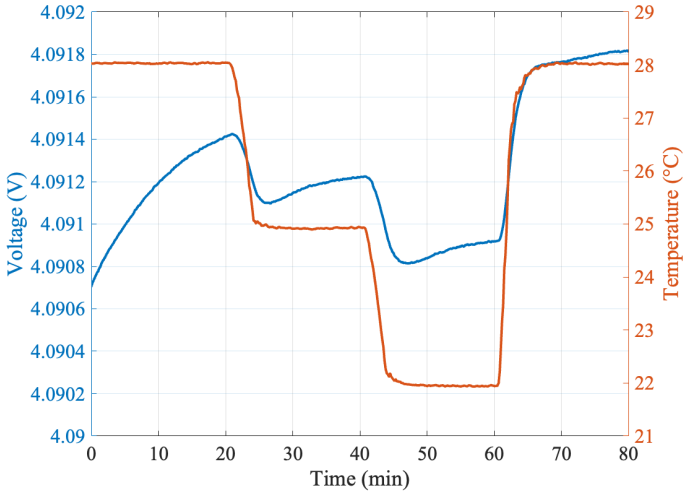

Figure 2.4: Entropy estimation: voltage variation due to temperature changes at 93 % SOC (discharge).

it having the smallest voltage error between the simulated and measured voltages within the training interval. Found parameter values together with standard errors are shown in Appendix B.

Step 3 Estimated voltage ($E_{\mathrm{OCP,est}}$) is subtracted from the measured voltage ($E_{\mathrm{OCP,meas}}$)

$$\Delta E_{\mathrm{OCP,est}} = E_{\mathrm{OCP,meas}} - E_{\mathrm{OCP,est}}. \tag{2.8}$$

Step 4 For improved accuracy, the mean of the last 6 points of each index of temperature change was used to estimate the OCP.

Step 5 The entropy (ΔS_{est}) was computed as the slope of the mean values of the estimated OCP change and the temperature change, as shown in Fig. 2.6,

$$\Delta S_{\mathrm{est}} = nF\frac{\Delta E_{\mathrm{OCP,est}}}{\Delta T}. \tag{2.9}$$

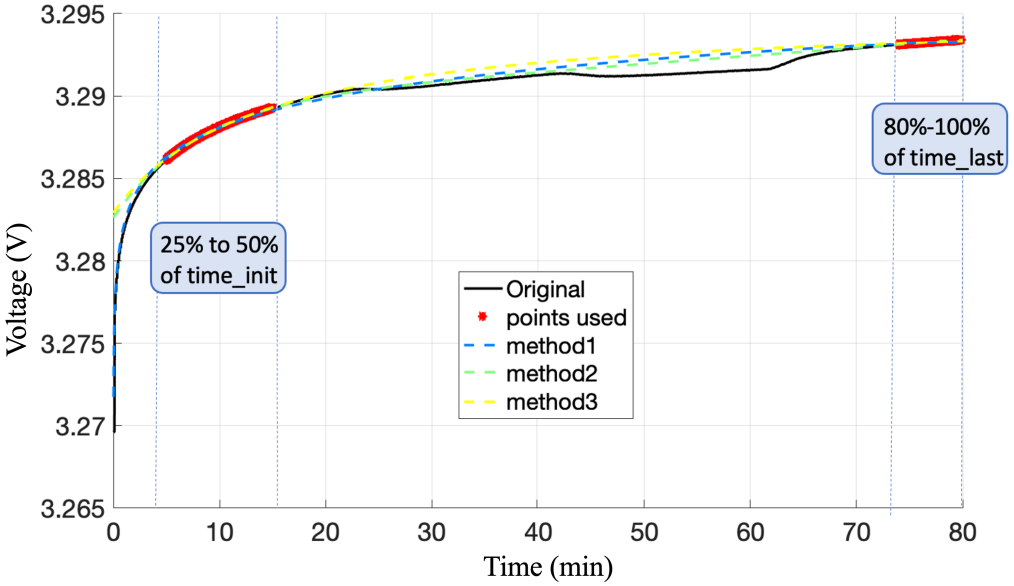

(a) Voltage simulation comparison using methods 1-5. Red stars indicate training intervals.

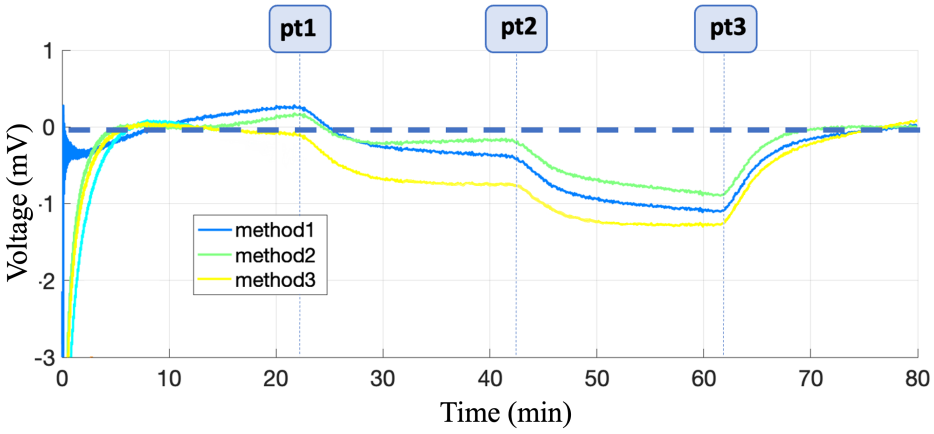

(b) Voltage error comparison between methods 1-5.

Figure 2.5: Entropy estimation: voltage simulation methods comparison.

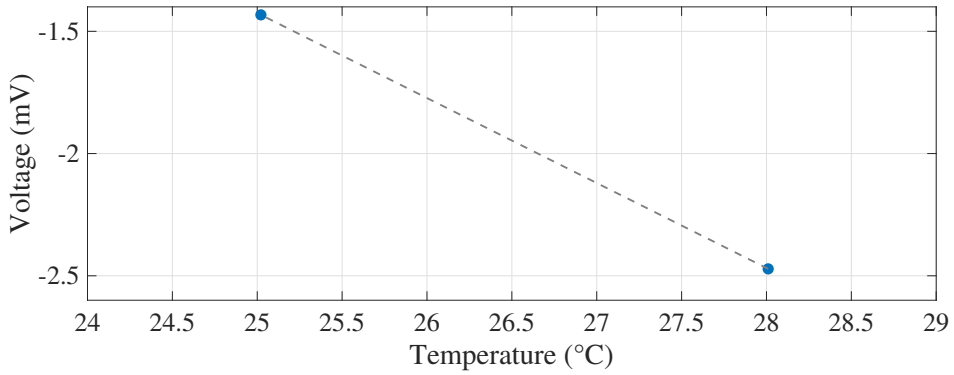

Figure 2.6: Entropy estimation: voltage vs temperature change.

2.3 Discussion of results

2.3.1 Half-cell entropy contributions

Differential voltage analysis, apart from being an effective quantitative method to identify the degradation modes of Li-ion batteries, is also used for comparison of individual electrodes with respect to the full cell. Anode and cathode capacities are scaled and horizontally shifted so that their dV/dQ profile superimposes with the dV/dQ curve of the full cell [82, 126]. The results of this comparison are shown in Fig. 2.7(a), where DVA is based on voltage and capacity data extracted from GITT. The low resolution of the OCP measurements here makes the DVA adjustment less accurate than that of the continuous C/25 (dis)charge data, but it does directly correspond to the extracted entropy data points.

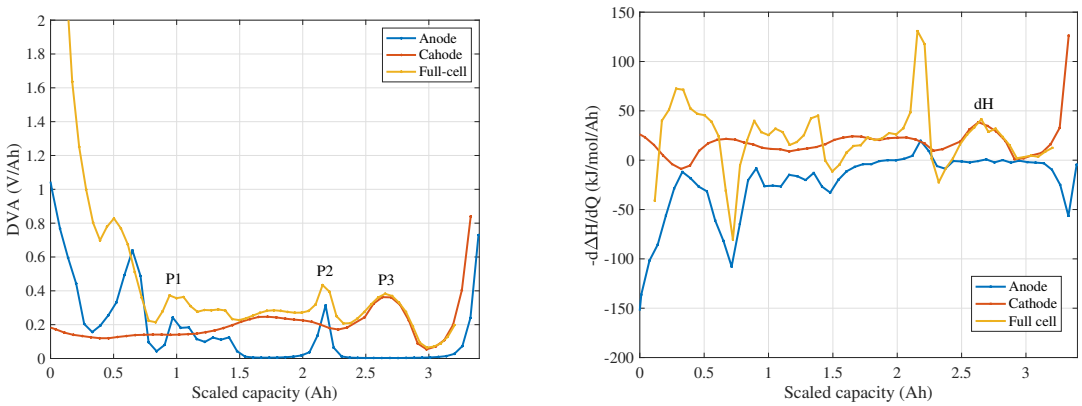

(a) (b)

Figure 2.7: (a) dV/dQ curves for the anode, cathode and a full cell. b) $d\Delta H/dQ$ for Gr/SiOx anode, NCA cathode, and a full cell during discharge. The phase transition marked 'dH' is dominated by the cathode. Here, partial molar enthalpy is estimated from $\Delta H = T\Delta S + nFE_{\mathrm{OCP}}$.

The measurements of half-cell reaction entropy may be summed to obtain the full-cell entropy change (as defined in Eq. 2.4), enabling features to be attributed to an individual electrode, as shown in Fig. 2.8. The full cell entropy change comprises the cathode (ΔS_{c}) and anode (ΔS_{a}) contributions

$$\Delta S = \Delta S_{\mathrm{c}} - \Delta S_{\mathrm{a}}, \tag{2.10}$$

which are defined similarly to Eq. (2.4).

During lithium intercalation, the open circuit potential of the Li–graphite system measured with respect to Li/Li$^+$ declines through a succession of sloping and flat regions that result from the staging process: single-phase transitions are the slopes and two-phase transitions correspond to flat regions [78, 103, 108, 127]. Although the anode material contains SiOx, during anode delithiation the anode related features are very similar to reported responses for lithium insertion into pure graphite [103, 108]. First, the Li$^+$ inserts into the spaces between each graphite layer in the anode host. Increasing Li$^+$ concentration drives the Li–graphite system into dilute stage IV

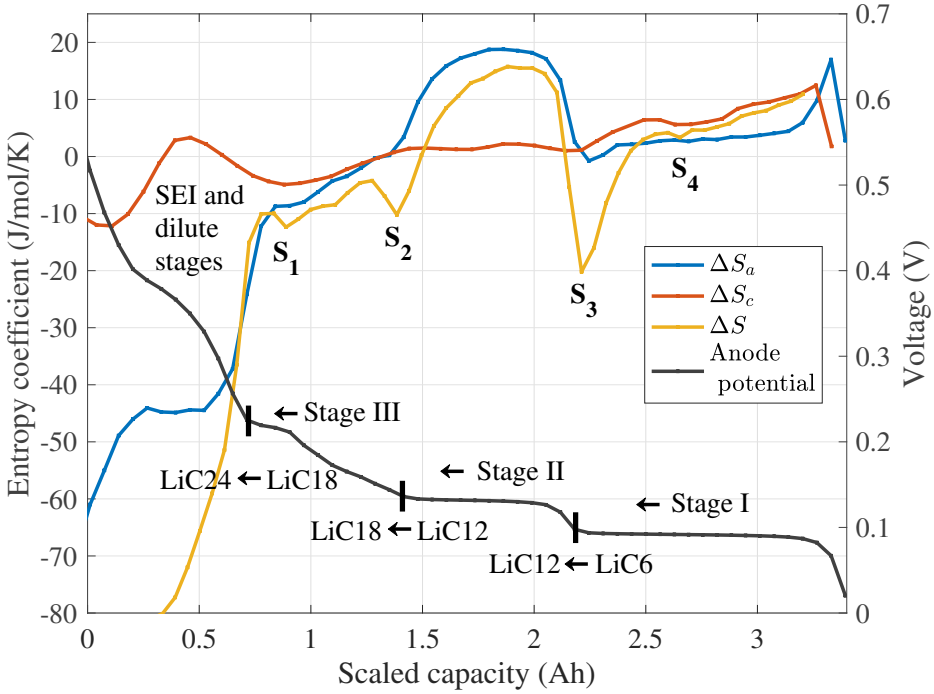

Figure 2.8: Entropy change profiles for anode (Gr/Si), cathode (NCA), and a full cell at the beginning of life. The entropy coefficient on the left y-axis refers to the ΔS_{a}, ΔS_{c}, ΔS respectively. The black line marking the anode OCP versus $\mathrm{Li/Li^{+}}$ uses the right-y axis. Characteristic full cell entropy features $\mathrm{S_1}$-$\mathrm{S_3}$ correspond to anode OCP staging.

structures, followed by dilute stage III structures. However, these stages are weakly ordered and so the entropy change follows an ideal solid-solution response in these regions [108]. Hence, at low lithium occupation in the anode (scaled capacity less than 1.5 Ah in Fig. 2.8), the ΔS_a rises as lithium is inserted. Over the same capacity range, there is a small feature in ΔS_c, but the cathode entropy profile otherwise remains relatively featureless.

Additional incorporation of Li^+ into graphite results in a two-phase region between about 1.5 Ah and 2.25 Ah capacity, where LiC_{12} and LiC_{18} coexist. There is therefore a voltage plateau, and similarly the S_a shows a transition at about 1.5 Ah capacity and then the entropy response remains nearly constant over the two-phase region. At about 2.25 Ah, a transition to LiC_{12}-LiC_6 coexistence occurs and ΔS_a rapidly changes in value, remaining again approximately constant across the capacity range of the voltage plateau. The cathode entropy remains close to zero within the capacity interval of the two main graphite phase transitions, which makes the anode the main contributor to the total cell entropy in this interval. Graphite-dominated phase transitions in the anode manifest as changes S_1-S_3 on the entropy curve, although these features appear as even more pronounced transitions in the full cell data than in the anode half cell data.

It is known that the phase transformations and lithium transport in graphite are relatively slow, limited by grain boundaries in the material [128], the staging dynamics of graphite [129, 130] and the exchange of ions at the electrode/electrolyte interface [131]. In full-cell configurations, non-uniform lithium distributions in the anode material arise from different Ohmic voltage drops and hence different local potentials at the centre versus the edges of the electrodes [132]. Consequently, inhomogeneous lithiation of graphite-based anodes has been reported, and because of slow relaxation processes, the resulting concentration gradients, from even modest polarisation, can persist over hours or even days of relaxation time [103, 133, 134]. In

commercial cells, these heterogeneities also persist over multiple length scales, and are observable by x-ray tomography and neutron diffraction [133,135]. Making the anode area slightly larger than the cathode, common in commercial cells, could lead to still greater inhomogeneous lithiation at the edges, as observed optically by Grimsmann et al. [136]. The cell examined in the present study was found to have an anode area $\approx 790\,\mathrm{cm}^2$ and cathode area $\approx 740\,\mathrm{cm}^2$, resulting in an overhang size $\approx 6\%$. The resulting non-uniform lithium distribution in the anode material could lead to higher lithium disorder and hence a greater entropy change due to disordered Stage II configurations [103,137,138]—anode overhang areas can also lead to reversible LLI [139]. The net result of all of these effects may be disparities between the combined reaction entropy from half-cells and the full-cell reaction entropy, particularly at the boundaries between graphite phase transitions. Despite these differences, it is still possible to extract the information concerning which electrode drives the full-cell entropy profile, because the phase boundaries on a voltage axis are clear from both the anode half-cell and the full-cell data.

In terms of the transitions in the cathode material, the redox process during delithiation is mainly at the Ni (III)–Ni (IV) pair, accompanied by three distinct phase transformations [140]. First, there is a transition from a hexagonal to monoclinic phase (H1 $\rightarrow$ M) starting at 0.4 Ah, then from monoclinic to hexagonal (M $\rightarrow$ H2) at around 2.5 Ah, and lastly, from hexagonal to hexagonal (H2 $\rightarrow$ H3) at 3.25 Ah [141]. The two last phase transitions do not appear to result in features in the full cell entropy profile. However, the M $\rightarrow$ H2 transition is associated with a sharp transition in the partial molar enthalpy in the cathode material (marked as 'dH' in Fig. 2.7(b)). This is advantageous because it allows changes in the position and amplitude of transition S_3 in the entropy profile (attributable to the main staging transition of graphite) to be probed in the absence of overlapping features from the cathode material.

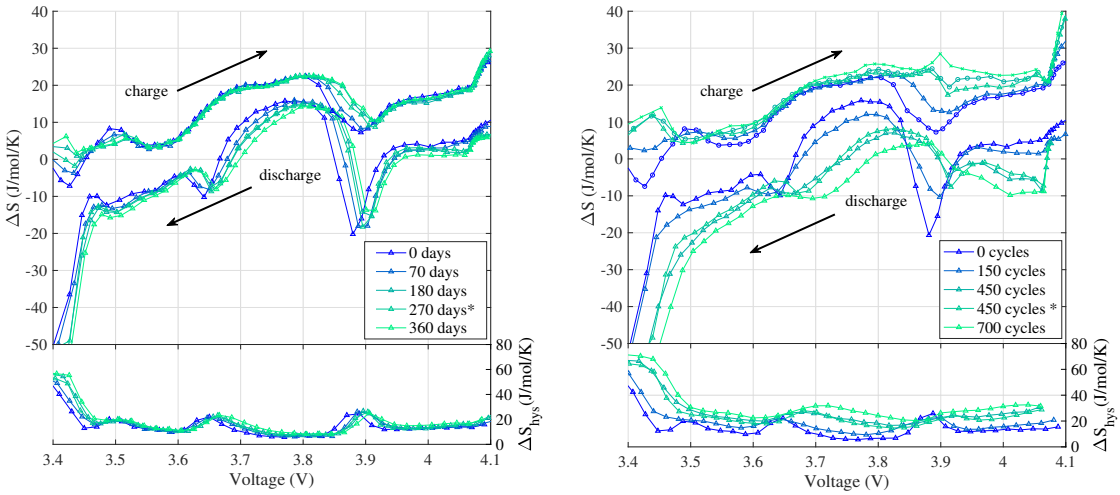

Figure 2.9: Charge and discharge entropy profile (a) after several days of storage at 75 % SOC at 45 °C, (b) after CCCV cycling at 45 °C. The bottom panel in both cases indicates entropy hysteresis, quantified by S_{hys}. * An unplanned 90 days of storage at 23 °C due to COVID-19.

2.3.2 Full cell entropy results

The reaction entropy measurements for the full cell are plotted against voltage in Fig. 2.9. The voltage range shown is 3.4 V to 4.1 V since this is where features of interest are present. Plotting entropy change against voltage allows for a more accurate comparison between charge and discharge by removing shifts in features with respect to concentration.

2.3.2.1 Calendar ageing

Fig. 2.9(a) shows that the entropy measurements remain almost unchanged after calendar storage. A small increase in the entropy magnitude is observed ∼3.87 V, denoted S_3 in the preceding section, corresponding to the graphite stage I to stage II transition; however, this effect is nearly negligible. The most pronounced change in the data is a horizontal shift towards higher potentials and horizontal expansion on the voltage axis. Similarly to ICA, this observed horizontal shift and expansion

indicates LLI [142]. There is a hysteresis in the entropy profile response, which is shown in the bottom panel of Fig. 2.9(a). The hysteresis is defined in Eq. (2.11) and results from the difference between the charge (ch) and discharge (dch) entropy change

$$\Delta S_{\text{hys}} = \Delta S_{\text{ch}} - \Delta S_{\text{dch}}. \tag{2.11}$$

Since there are no significant changes to the entropy magnitude experienced by calendar aged cells, the entropy hysteresis also remains almost unchanged. These findings are consistent with the results presented by Sullivan et al. [74] studying a LCO cathode half-cell subjected to calendar ageing. The entropy profile shape and characteristic regions did not change when a substantial proportion of cell capacity was removed. It was concluded that the intercalation mechanisms in the aged cell remained the same.

2.3.2.2 Cycling ageing

Fig. 2.9(b) shows the effects of cycle ageing on entropy change. In contrast with the results shown for calendar ageing, the cycling ageing results indicate a more dramatic shift of all of the features towards higher potentials. Additionally, different changes in entropy magnitude are observed with respect to the direction of reaction. For full cell discharge, a gradual decrease and flattening of characteristic features is observed. For charge, however, entropy change increases with cycling age, with the most pronounced increase above 3.87 V.

Features near 3.87 V The characteristic minimum in the entropy profile occurring ~3.87 V corresponds to the most pronounced graphite transition, stage I to stage II [103, 108, 137]. The cathode entropy change is featureless in this region. Therefore, the recorded entropy change variation most likely originates from microstructural changes to the graphite. With cycling, the entropy minimum increases (i.e. the step

becomes less pronounced) and shifts positively in voltage.

Features below 3.87 V To the left of the characteristic graphite stage I → stage II transition, there is a slight increase in the entropy change during charge (lithiation of the anode material). However, during discharge (anode delithiation), a more substantial decrease in entropy is seen as the cell ages.

Features above 3.87 V At voltages above ∼3.87 V, the full cell entropy change continues to decrease with cycle age. For charge, an increase in entropy change is observed. For a pristine cell shown in Fig. 2.8, the entropy change contribution from the anode material is close to zero, and the full cell entropy response is mainly due to the cathode material. As the internal resistance of the cell increases with cycle age, the upper voltage limit is reached prematurely. Consequently, the ability to extract the entropy values at these points is compromised. As a result, the number of extracted entropy points decreases as the battery ages, which is visible at the edges of Fig. 2.9(b).

2.3.2.3 Impact of silicon on entropy profiles

As a battery electrode material, graphite is an intercalating material, with Li inserting into its layered structure [112], whereas silicon is an alloying material, experiencing solid-solution reactions with lithium [112]. The features of the OCP versus SOC and the balance of lithium intercalated in Si and Gr at each SOC depend on the ratio of Gr to Si in the anode and also the cycling direction [66, 143]. Since Si is 10% wt of the anode, but its gravimetric capacity is 10 times the graphite (372 mAh/g), the overall anode capacity is equally composed of 50% Si and 50% Gr [144].

Anode delithiation Due to the similar contributions of Si and Gr to the anode capacity, delithiation happens sequentially [78, 112], that is to say, Gr dominates the

initial stages of full cell discharge in the range 4.2 V to 3.87 V (Fig. 2.9). Then, the capacity contribution from Si and Gr become comparable within 3.87 V to 3.65 V interval. Lastly, at < 3.65 V, anode delithiation becomes completely dominated by Si.

Consequently, the discharge entropy change profile shown in Fig. 2.9(b) is a combination of both the Si and Gr reactions, where a steady entropy change flattening with cycling is observed.

A possible explanation for this is mechanical changes in the anode particles, specifically breaking and cracking, as has been reported in other studies [145, 146]. This is also often mentioned as a primary cause of Si particle inactivation in Gr-Si anodes [78, 147–149]. Entropy profiling measures (among other contributions) the configurational degrees of freedom of lithium-vacancy arrangements in the electrode materials [103,105,106,108,137]. Microstructural changes reduce the number of accessible sites in the host material by causing point defects [107, 121] and stacking faults (i.e. turbostratic disorder [150, 151]). Given that there are only small entropy profile features from the cathode material at the start of life, changes to cathode morphology from entropy profiling are not expected to be detectable, even if they are present. Changes to the surface structural ordering of graphite with repeated cycling have been reported elsewhere using Raman spectroscopy [152, 153], even when the C-rate is as low as C/37 [153]. It is known that the Li-graphite stages are extremely sensitive to the stacking order of graphite [150, 151]. The observed changes in entropy profiling with cycle ageing are consistent with the changes to the staging sequence that would be expected with this type of structural disordering, resulting in a reduced amplitude of the entropy change from those transitions. This trend is in accordance with the observed changes to the S_3 feature at $\sim$3.87 V.

Anode lithiation Because of the (de)lithiation hysteresis introduced by Si, the balance of lithium in Gr and Si at each full-cell voltage is very different during lithiation of the anode. Based on the stoichiometric model of lithium filling in Gr/Si blends presented by Jiang et al. [112], lithiation proceeds simultaneously within Si and Gr in the interval 3.4 V to 4.1 V. However, over the same voltage interval, a greater fraction of Li is inserted into Si. According to the same model, it is only in the part of the anode half-cell voltage profile corresponding to full cell voltage ($>$ 4.1 V) that a greater fraction of lithium is into inserted into Gr. This explains the observed differences between charge and discharge entropy profiles. An increase in the entropy change with cycle ageing may suggest expansion of the Si particles with ageing, agreeing with Vorauer et al. [115]. The cited work suggests volume expansion is associated with a more non-uniform distribution of lithium, and therefore, it is possible that this results in the observed increase in entropy change. Therefore, the discharge entropy measurements should be considered and analysed separately from the charge measurements.

Entropy hysteresis Over a broad voltage range, the entropy hysteresis increases with cycling. It is known that there is a negligible difference between graphite (de)lithiation entropy change above $\sim$3.87 V in a full-cell [103, 108, 137], but there is a hysteresis in pristine graphite at full-cell voltage $\sim$3.87 V, which is attributed to metastable carbon stacking configurations [103]. It is hypothesized that the main source of hysteresis visible in Fig. 2.9(b) originates from Si, given its large OCP hysteresis [149] over a broad voltage scale. However, during graphite transition II $\rightarrow$ I at $\sim$3.87 V, and graphite transition III $\rightarrow$ II at $\sim$3.65 V, the entropy hysteresis remains fairly constant with cycle age. This could be due to a localised decrease in hysteresis from graphite, in combination with increase in hysteresis from silicon across the entire voltage range. Since additional features in the anode half-cell en-

tropy profiles compared with published data for pure Gr anodes cannot be detected, the observed behaviour at 3.87 V and 3.65 V is attributed to the effect of microscopic Gr degradation.

2.3.2.4 Comparison of DVA and entropy profiling

Entropy magnitudes and entropy hysteresis ageing data may be plotted against voltage, as above, giving insight into microstructural material changes. One can also compare data against capacity, giving insight into electrode stoichiometry changes (similar to DVA). For consistency, entropy and DVA curves were all calculated from the same GITT data. Fig. 2.10 shows superimposed profiles of entropy change and DVA against capacity axis for pristine and aged cells. For calendar aged cells, there is a slight shift towards lower capacities with age. This characteristic is emphasised for cycle aged cells, which lost more capacity. It is apparent, however, that the DVA peaks marking phase transitions find no correlation with characteristic features in the entropy change profile.

To compare DVA with entropy profiling directly, the derivative of ΔS with respect to capacity (i.e. $d\Delta S/dQ$) is computed and is plotted in Fig. 2.11. Since DVA is a well established diagnostic method, it is used here as a baseline for identification of degradation mechanisms experienced by aged cells. DVA curves for charge and discharge are shown in Fig. 2.11. In all test data, the cathode DVA peak D_4 shifts towards lower capacities with ageing. According to the literature [80], a horizontal shift on a DVA curve is due to loss of cyclable lithium. The calendar aged cells exhibit less visible shifts, indicating less capacity loss than the cycled cells. A corresponding horizontal shift of marker dS_4 is observed in Fig. 2.11. The anode peak D_3, indicating the graphite stage II $\rightarrow$ I transition, decreases marginally in magnitude for the calendar aged group. This is followed by a proportionally smaller decrease of the dS_3 peak. In the cycled group, however, the DVA peak D_3 flattens to the point that it

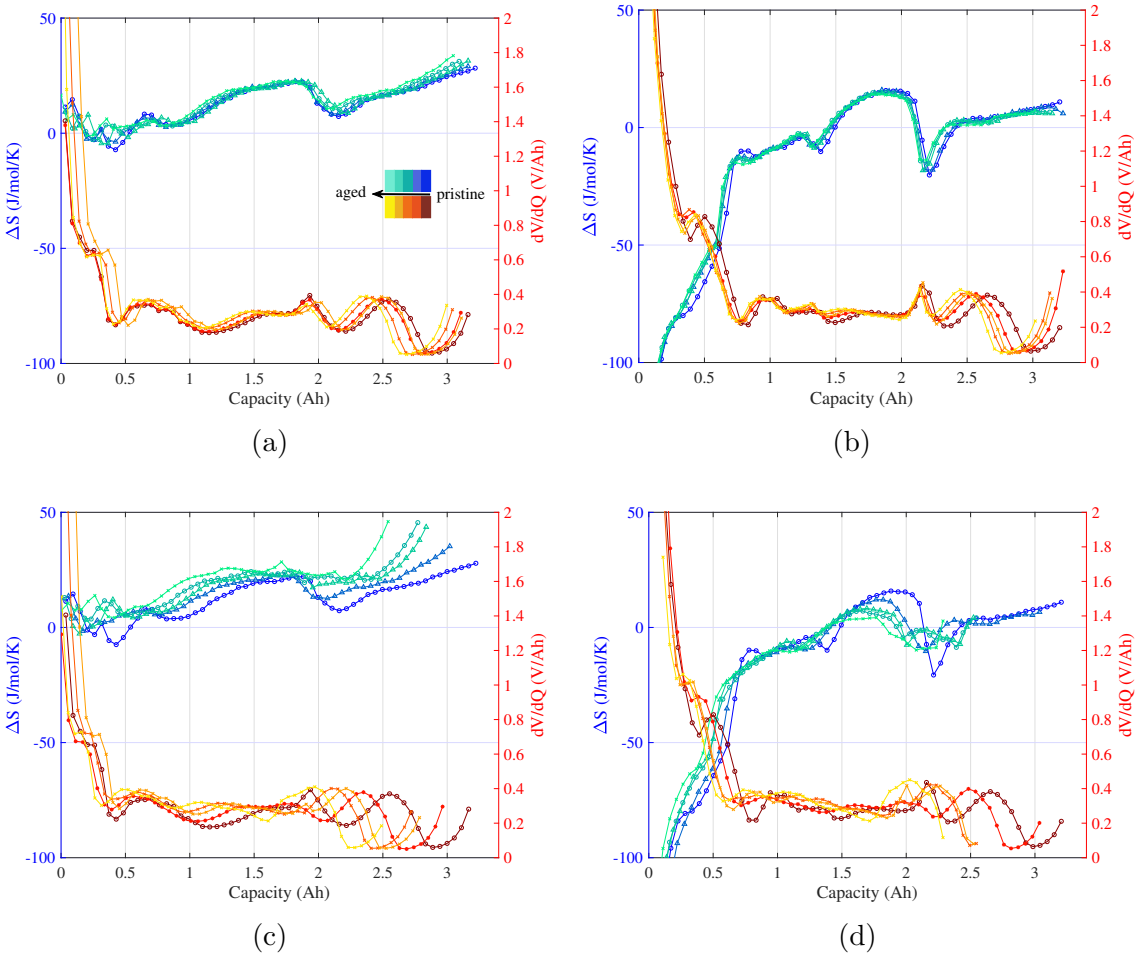

Figure 2.10: Entropy change and DVA plots for calendar aged cells (a) charge (b) discharge and cycle aged cells c) charge d) discharge.

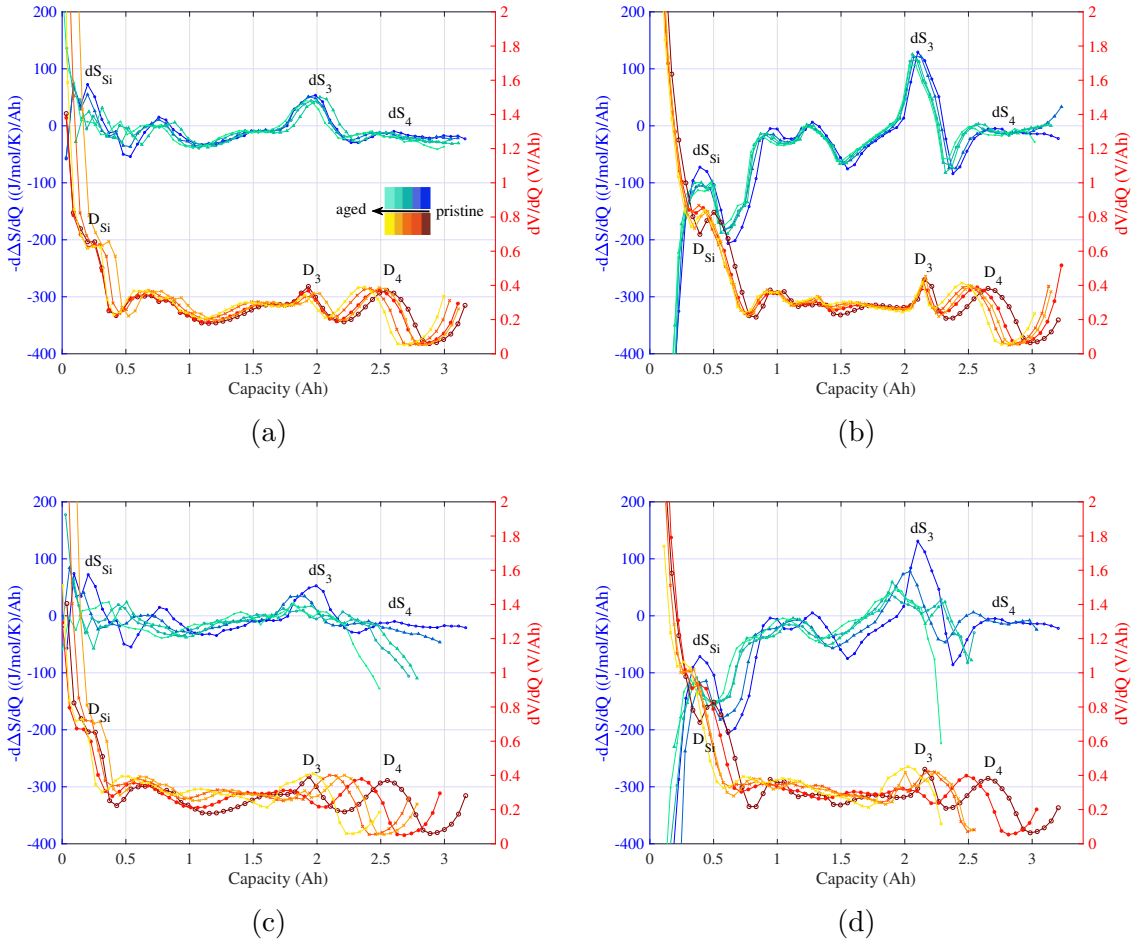

Figure 2.11: $d\Delta S/dQ$ and DVA plots for calendar aged cells (a) charge (b) discharge and cycle aged cells (c) charge (d) discharge.

becomes difficult to distinguish. In the entropy plot, peak dS_3 is still well recognisable, although it decreases in magnitude from the pristine cell data. This suggests that the entropy change curve is more sensitive to anode phase transformations than the DVA curve.

The two DVA features D_3 and D_4 are crucial for the diagnosis of electrode-specific degradation modes [80, 83]. Loss of active material (LAM) in the positive electrode $Q_{\text{LAM,PE}}$ is calculated from the capacity difference between D_4 and Q_{full}, the maximum measured capacity. Similarly, at the negative electrode $Q_{\text{LAM,NE}}$ is identified as the change in capacity between D_3 and 0 Ah, while the shift between electrodes Q_{balance} is the difference between the maximum capacity and $Q_{\text{LAM,NE}}$.

Following the Keil et al. method [80], the same procedure was applied to the entropy curves to extract ageing markers. From Fig. 2.11 it is clear that the anode peak D_3 corresponds to DVA peak dS_3 and so peak shifts indicate LAM_{NE}. The cathode peak D_4 occurs in the same region as the dS_4 peak, and is therefore used to calculate LAM_{PE}. The results obtained from both the entropy and DVA markers are shown in Fig. 2.12. Despite some differences, the resemblance is noteworthy, confirming that entropy measurements can be successfully used for identification of degradation mechanisms.

Note that, due to the full cell hysteresis emerging largely from Si in the anode material, the ageing markers may provide different information when calculated from charge instead of discharge data. However, the standard practice in the literature is to analyse only one direction of DVA profiles, most commonly charge [82, 119, 145]. Given that the main objective in this study is the comparison of extracted markers from both DVA and entropy profiling, the same procedure is followed here, and only charge data is used. However, extracted markers are presented in terms of normalised capacity to account for differences between charge and discharge. Note that the Si marker in Fig. 2.11, dS_{Si}, occurs at low SOC and is strongly influenced by current direction. Shifts to this marker are difficult to quantify and interpret, and therefore are not considered in this study.

Analysis of ageing markers Fig. 2.12(a) shows the estimated ageing markers for the calendar aged cells. Capacity fade appears to be caused primarily by LLI, which manifests in electrode balancing changes. This confirms that the horizontal shift on the voltage axis observed in Fig. 2.9(a) is due to changes in electrode balancing. No further ageing markers are evident for the calendar aged cells, making LLI the main ageing mechanism. Conversely, Fig. 2.12(b) shows the ageing markers for the cycle-aged cells. Overall, there appears to be a decrease in LAM_{NE} with age, as has

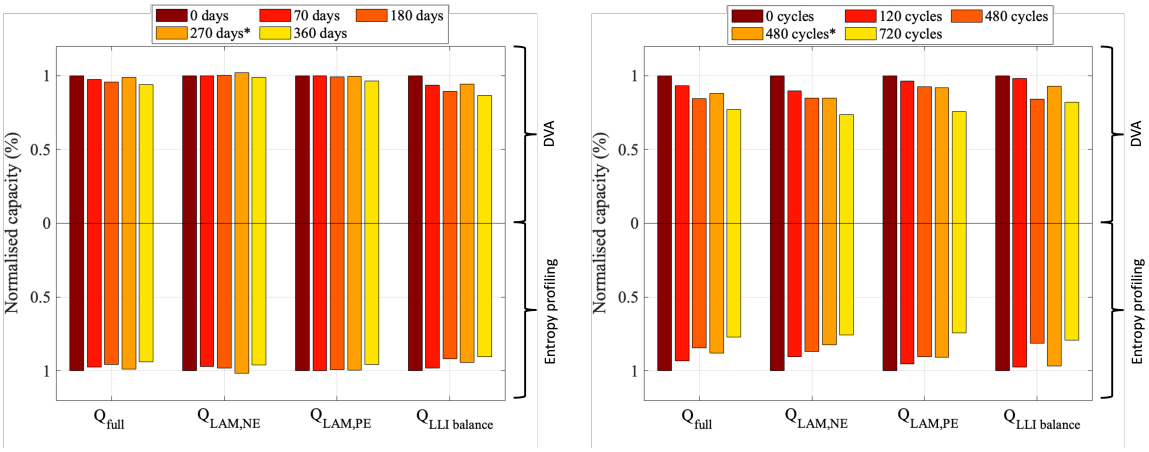

(a) (b)

Figure 2.12: A comparison of ageing markers extracted from DVA and entropy profiling for calendar aged (a) and cycle aged (b) groups of cells. In both cases, the charge profiles were used to extract the ageing markers.

been found by others [145, 154]. In our data, LAM_{PE} also decreases, indicating additional degradation of the cathode material. Lastly, a decrease in electrode balancing $Q_{LLI\ balance}$ suggests lost Li inventory.

It is noted that there is an apparent 'capacity recovery effect' between RPT3 and RPT4. This time period corresponds to an extended COVID-19 lab closure, during which two test conditions were changed simultaneously: the temperature was decreased from 45 °C to 23 °C and the SOC decreased from 75% to 50%. This resulted in calendar aged cells experiencing a recovery in LLI together with a less pronounced increase in LAM_{NE}. This suggests recovery of capacity from the well-known 'anode overhang' effect [139]. Geometrically, anode overhang is defined as an additional anode area which is not directly opposed by the cathode [155]. Given longer ionic pathways and therefore a very slow timescale for lateral diffusion from the anode overhang area to the usable battery area, under certain favourable conditions and very long time periods, some capacity can be regained [155]. This effect is also present in the cycled cells between RPT3 and RPT4; however, LAM_{NE} remains constant in that case.

2.3.2.5 Comparison of ICA and entropy profiling

The comparison of entropy profiling with ICA provides further, but limited, insight into degradation characteristic. ICA peaks indicate phase equilibria, and are expected to manifest as featureless regions on the entropy curves—therefore they cannot be directly correlated with entropy profiling characteristic features. Both dQ/dV and entropy profiles are presented in Fig. 2.13 for charge and discharge for both calendar aged and cycled aged cells.

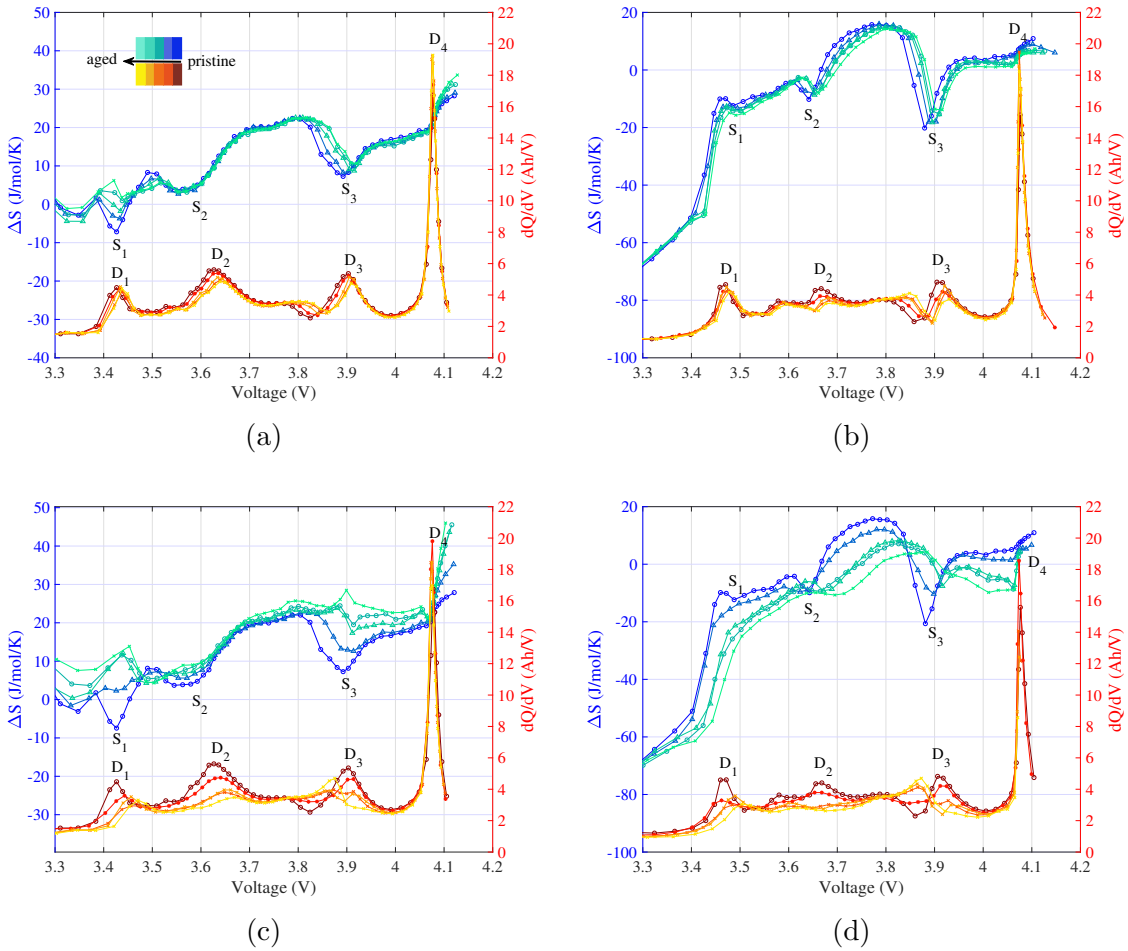

Figure 2.13: Entropy change and ICA plots for calendar aged cells (a) charge (b) discharge and cycle aged cells (c) charge (d) discharge.

For the calendar aged cell, the ICA peaks shift toward higher potentials, except for peak D_4 as shown in Fig. 2.13(a) and (b). According to [142], the stability of peak

D_4 indicates no significant change in the cathode active material. The horizontal shift towards higher potentials of ICA peaks during charging suggests an increase in LLI [156]. The same conclusion can be drawn from the entropy behaviour. For both charge and discharge, the entropy profile shifts towards higher voltages, which, as indicated by ICA, suggests LLI.

According to Riviere et al. [81], a decrease in the intensity of the ICA peaks indicates LAM, but this cannot be quantified and distinguished between individual electrodes as accurately as with DVA. The intensity of peak D_4 increased, while the magnitude of peaks D_1-D_3 decreased marginally, indicating that LAM in either electrode was minimal. This supports the conclusion that LLI is the primary degradation mechanism for calendar aged cell. The intensity of the entropy peaks remained relatively unchanged, with only a slight decrease in the magnitude of feature S_3. This confirms that there have been negligible changes in the particle morphology, and therefore no LAM. While the trough S_2 remains constant, feature S_3 shifts towards higher potentials, elongating the anodic S_2-S_3 region. There is no information in the literature that discusses such behaviour, but based on the information obtained from ICA, it likely relates to changes in the electrode balancing. For the cycled cells, as shown in Fig. 2.13(c) and (d), the ICA and entropy profiles are more diverse, possibly indicating the presence of multiple competing ageing mechanisms. For both charge and discharge, the first two ICA peaks (D_1 and D_2) shift towards higher potentials, while peak D_3 shifts towards lower potentials. This shift suggests changes in the electrode balancing. Peak D_4 remained stationary, therefore it can be concluded that the cell did not experience LAM in the positive electrode. In contrast, the intensity of peaks D_1-D_3 decreased significantly, pointing to LAM in the negative electrode (LAM_{NE}) and LLI as the main contributors to degradation for the cycle aged cell.

The cycled cells display significant differences in their charge and discharge entropy profiles. These differences are perhaps a result of morphological changes experienced by Si, such as expansion and contraction during cycling, causing alterations in both the magnitude and shape of the entropy profile. The fact that region S_2-S_3 expands (visible for both charge and discharge) suggests LLI as a degradation mode.

2.3.2.6 Changes in the internal resistance

The internal resistance of the cells R_{IR} may be calculated from the initial voltage drop following an applied current. In this case voltage drop in the first 1 s of applied GITT pulse was used to calculate the R_{IR}. Considering the low current magnitude (C/10) of a GITT pulse, an assumption can be made that the obtained values contain ohmic, SEI and ionic resistances, all independent of applied current.

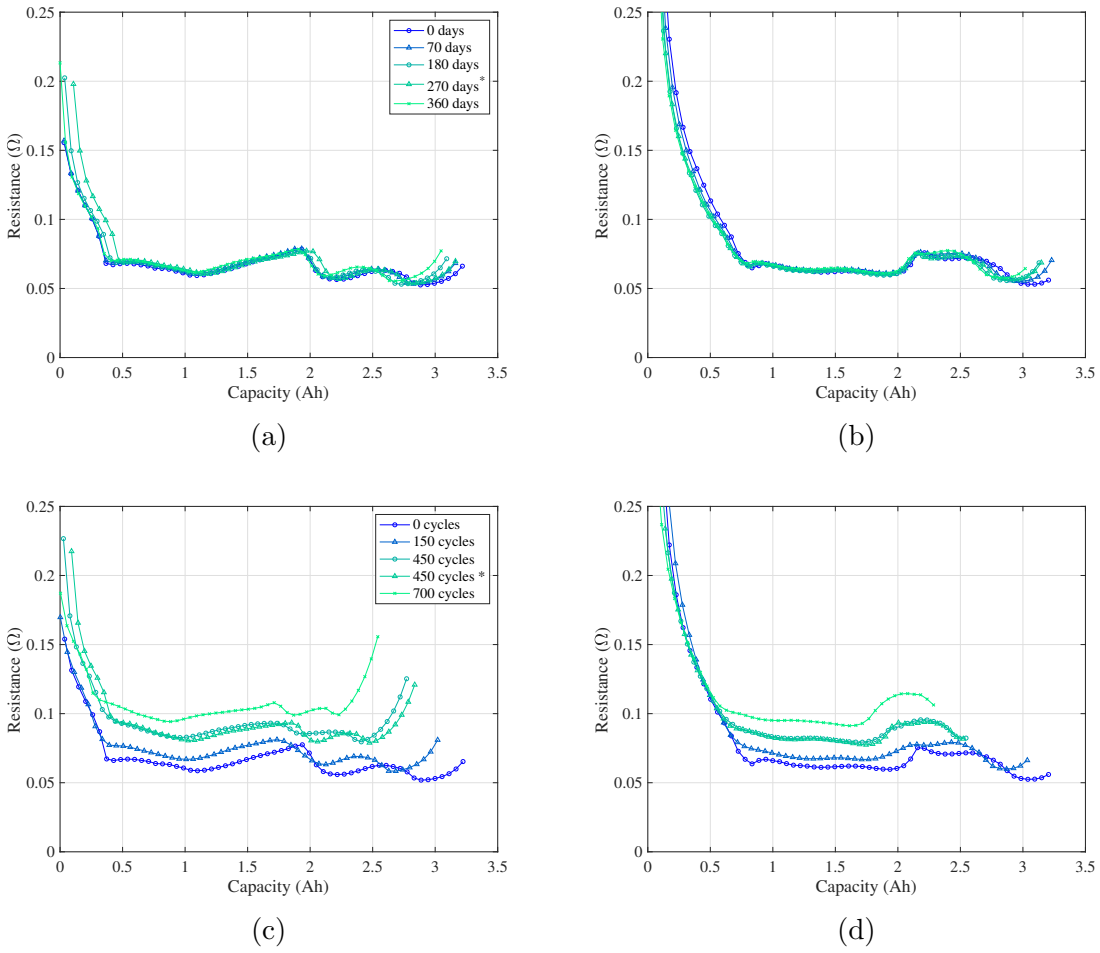

Figure 2.14: Internal resistance plots for calendar aged cell charge (a) and discharge (b). Cycle aged cell reveals substantial increase in internal resistance for charge (c) and discharge (d) with number of cycles.

The internal resistance (R_{IR}) is plotted against cell capacity in Fig. 2.14 for both charge and discharge cycles of calendar aged and cycle aged cells. The results show a negligible change in R_{IR} for the calendar aged cell but a substantial, two-fold increase in R_{IR} for the cycle aged cell.

2.4 SEM/EDX analysis

To independently check the degradation signatures obtained from entropy profiling, a post-mortem analysis was conducted on one cell from each of the interest groups—

pristine, calendar aged and cycle aged.

2.4.1 Method

A pristine, calendar aged, and cycle aged full-cell were fully discharged to 2.5 V at C/10 constant current and disassembled in an Argon-filled glovebox (Inert Pure-Lab HE). Scanning electron microscopy (SEM) measurements were performed with a JEOL JSM 6500F FEG-SEM, operated at low voltage (5 kV) to highlight the surface details. Subsequently, a JEOL JSM 6480LV (15 kV) SEM was used to obtain energy-dispersive X-ray spectroscopy (EDX) maps.

A micrometer with 0.001 mm resolution and ±0.002 mm accuracy was used to measure the coating thicknesses of the electrode material harvested from the full cells. The coating thickness was determined by subtracting current collector thickness from a single layer thickness. This procedure was performed at three different locations on the electrode and a resultant average value was calculated.

2.4.2 Results

The cell tear-down inspection revealed no noticeable discoloration or delamination on the cathode of both the pristine and the aged cells. However, the anode's active material was found to be more susceptible to cracking and flaking after opening the jelly roll. The most significant contrast between pristine, calendar-aged, and cycle-aged cells was observed on the separator surface, which exhibited indications of electrolyte decomposition, as depicted in Fig. 2.15.

Subsequently, the morphologies of both the negative and positive electrodes were studied using SEM. Fig. 2.16(a) shows the surface of the pristine anode material. In this image, the Gr edges are sharp and well defined. The image of the calendar aged material is presented in Fig. 2.16(b), which shows that the sharp edges of Gr become less prominent. The coarse particles could be ascribed to the formation of the

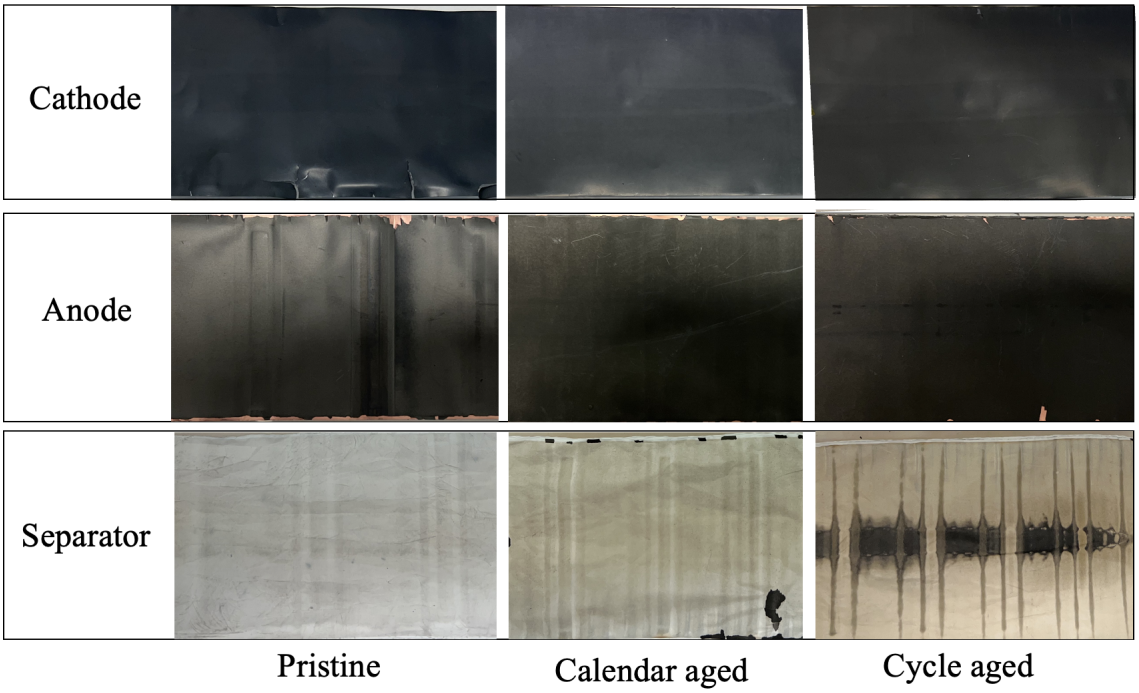

Figure 2.15: Representative samples of cathode (first row), anode(second row) and separator (3rd row) from Samsung 35E teardown. The first column corresponds to pristine cell, the second to the calendar aged cell and the third to the cycle aged cell.

SEI layer. Consequently, the surface film thickness increases from 82 µm to 86 µm. These observations correspond well with the dominant degradation mode identified by DVA and entropy profiling, namely LLI caused by SEI growth. Finally, Fig. 2.16(c) shows the impact of cycle ageing, where surface film formation becomes significant, also consistent with LLI. Consequently, the coating thickness increased to 90 µm, i.e. slightly thicker than the calendar aged film. Given that the LLI in the calendar and cycle aged materials was similar, it is attributed the difference between the two instead to greater volume expansion from cycle ageing.

Fig. 2.16(d)-(f) show the back scattered electron (BSE-SEM) images of the pristine, calendar and cycle aged electrodes, respectively. In the pristine sample, the SiO_x particles are visibly brighter than the surrounding graphite particles because of the higher atomic number of Si compared with carbon, and hence greater electron back scattering. The SiO_x particles in the pristine sample are also brighter compared

with the calendar aged and cycle aged ones. The difference in brightness can be attributed to the pulverisation of the densely packed SiO_x aggregates upon electrochemical cycling, which leads to disconnection of particles via vacancies left behind by lithium-ion stripping [157]. This lithiation-driven fracture in SiO_x particles results in a newly exposed active material surface, which leads to further SEI formation. The SEI is composed of lighter elements compared to Si and therefore SEI growth results in a darker image compared to the brighter pristine electrode. It has been reported in the literature that a large part of the film growth on Si/C anodes is due to the formation of lithium silicates [158,159], which could also account for the LAM observed in the entropy/DVA analysis.

The SiO_x particle size range was determined by measuring all the coloured particles representing the element Si in a 2D EDX images, Fig. 2.16(g)-(h). The size range of the SiO_x particles was found between 1-9 µm, but it was difficult to assess pulverisation effects solely based on Fig. 2.16(g)-(i).

In contrast to the anode, no thickness changes were observed on the cathodes across pristine versus aged cells. There were also no obvious colour differences in the element distribution of EDX mapping shown in Fig. 2.17.

Scanning electron microscopy is a powerful tool for battery degradation analysis, however, its localised character, due to high magnification, can hinder the study comprehensiveness. To make the conclusions more robust and comprehensive, it would be desirable to examine many more samples harvested from diverse locations on the electrodes, but this was not possible within the time-frame of the current research. The SEM/EDX analysis was conducted with the help of Chris Salter and Oxford Materials Characterisation Service.

2.5 Conclusions

In this study of silicon-graphite/NCA Li-ion batteries, reaction entropy changes were analysed during calendar and cyclic ageing. Comparison of half- and full-cell entropy data revealed that the entropy measurements associated with the NCA cathode were almost uniform as a function of capacity, in contrast to anode entropy measurements. Thus the full-cell entropy measurements were dominated by anode-related features during both charge and discharge.

A significant difference between the measured entropy profiles during charge and discharge was found, indicating an 'entropy hysteresis' related to path-dependent reaction mechanisms in the electrode materials. Changes to the entropy hysteresis with age were used to infer qualitative changes to the cell material morphology.

For the calendar-aged cells, the entropy profile magnitudes remained almost unchanged with age, but slight shifts versus voltage were found. Additionally, the entropy hysteresis remained unchanged with age. These results likely imply that the microstructure of the electrode materials did not change substantially with age.

In contrast, in cycle-ageing data, our investigation revealed a decrease in entropy magnitude during discharge and an increase during charge, with greater shifts in the observable features as a function of voltage than were found during calendar ageing. The combination of the shift and amplitude change may be attributed to particle breaking and cracking induced by cycling, with concomitant microstructural changes to the anode material. It is hypothesised that the changes to graphite-related entropy features originate from microstructural defects. The overall increase in entropy hysteresis may be related to Si volume expansion effects, however further research is required to establish the exact dependency of entropy features on particle size and Si mass fraction.

A direct comparison between entropy profiling and DVA reveals that in general, both techniques highlight similar features of battery behaviour. Entropy profiling can

thus successfully track ageing markers such as LAM_{PE}, LAM_{NE} and LLI. Using these techniques, both DVA and entropy profiling highlighted LLI as the main degradation mode for calendar aged cells. Cycled cells on the other hand experienced LAM_{NE} and LAM_{PE} combined with LLI. Notably, the entropy magnitude was found to provide greater sensitivity to changes and features at some operating voltages, and these features are not accessible by DVA.

Further comparison of entropy profiling with ICA confirmed the LLI mode that was suggested from DVA, but also suggested an increase in the internal resistance. The R_{IR} of calendar-aged cells remained unchanged, therefore LLI was the sole degradation mode for this cell. However, a twofold increase in (R_{IR}) was revealed for the cycle aged cell. This corroborates well with other studies (i.e. [145]. Although some LAM information can be inferred from ICA, it is concluded that more (quantitative) insight may be achieved from DVA and entropy plots against capacity. Table 2.2 summarised the capabilities of entropy profiling against DVA and ICA.

The fact that entropy profiling reflects microscopic changes happening within electrode, on top of ageing markers, makes it unique noninvasive tool among ICA and DVA. It appears that the entropy change curve is more sensitive to anode phase transformations than the DVA curve. However its application is challenging, as discussed below.

Table 2.2: Degradation mechanisms identification summary for entropy profiling, ICA and DVA for studied NCA/Gr-Si cell.

Degradation modes	Entropy vs voltage	Entropy vs capacity	ICA (vs voltage)	DVA (vs capacity)
Capacity decrease	NA	Entropy profile horizontally shifts towards lower capacities	NA	DVA profile horizontally shifts towards lower capacities
$LAM_{PE,\ NE}$	Same principle as ICA, but in practice too difficult to be practical	Cathode/anode peak (dS_4/dS_3) shifts towards lower capacities $Q_{LAM,PE} = Q_{max} - Q_{dS4}$ $Q_{LAM,NE} = Q_{dS3} - Q_0$	Horizontal shift of ICA peaks and/or peaks decrease/area under peak decrease	Cathode/anode peak (D_4/D_3) shifts towards lower capacities $Q_{LAM,PE} = Q_{full} - Q_{D4}$ $Q_{LAM,NE} = Q_{D3} - Q_0$
LLI (balancing changes)	S_2 stable while S_3 shifts towards higher potentials resulting in the expansion of the S_2-S_3 segment	$Q_{balance} = Q_{full} - Q_{dS3}$	ICA peaks shift towards higher voltages/ inconsistent shift	$Q_{balance} = Q_{full} - Q_{D3}$
Morphology changes: eg. particle cracking	Characteristic entropy features fade	Characteristic entropy features fade	NA	NA

2.6 Limitations and further work

2.6.1 Limitations

A limitation of the entropy profiling technique is its requirement for a specialised measurement setup and a trade-off between data resolution and the length of testing. To accelerate entropy measurement, cells must be placed in a fluid medium with a high heat transfer coefficient to promote fast ($\sim$ 10 min) and uniform heat exchange. Typically, DVA/ICA measurements use a C/20 current, resulting in an experimental time of $\sim$20 h, not including preparation time. Entropy profiling meanwhile requires 80 min per SOC point evaluation. Consequently, in 20 h window, it is possible to evaluate only 15 SOC points. While this resolution may detect general entropy changes due to ageing, it may not provide sufficient detail to identify specific degradation markers. At the same time, the presented 20 min intervals per each temperature change here is probably excessive, given temperature stabilisation was reached after

$\sim$7 min. As a result, using 10 min intervals instead could enable the evaluation of 30 SOC points within the typical time frame required for DVA/ICA measurements. The evaluation at certain SOC ranges could be optimised by focusing on specific characteristic features and reducing the resolution in other areas. In this manner, entropy profiling can be compared to ICA and DVA in terms of time commitment, but the requirement for a specialised setup cannot be avoided.

Another disadvantage of discontinuous entropy measurement is that, as the battery ages and resistance increases, the endpoints become inaccessible earlier as the cutoff voltage is reached sooner. If no adjustment or optimisation strategy is applied, the measurement window becomes smaller.

Another challenge faced by entropy profiling, as well as ICA and DVA, is the use of extracted information about degradation mechanisms. In real-world applications, the information must be stored and perhaps presented in the form of lookup tables and compared regularly with measured data. This suggests that entropy profiling might be better suited for grid applications, which provide a more controlled and reliable environment for more accurate measurements.

2.6.2 Further work

Further work should focus on exploring the relationship between entropy and morphological changes. This research would enhance the understanding of microscopic changes without the need for cell tear-down, surpassing the capabilities of DVA degradation diagnosis. In addition to the information about phase transitions obtained from OCP vs capacity data, it would involve correlating particle size, electrode porosity, and entropy magnitude and shape.

The limited availability of literature measuring the entropy of batteries with silicon-doped anodes highlights the need for further research to confirm the findings of this study. Additionally, while this study confirmed the use of entropy profiling to

extract degradation markers following Keil's procedure [80], its applicability to other battery chemistries needs to be verified.

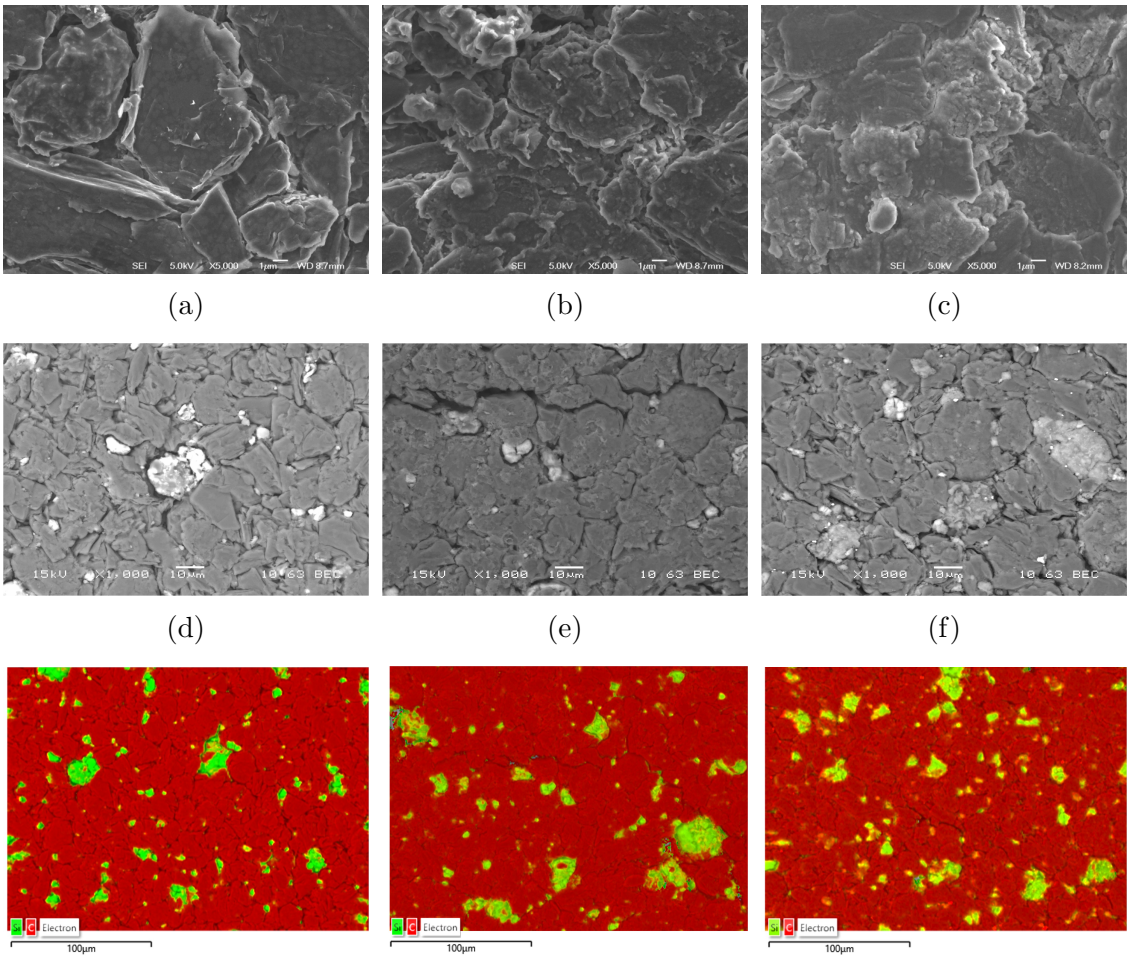

Figure 2.16: SEM and EDX images of Gr/Si anode harvested from a full cell. First row: SEM images for (a) pristine (b) calendar aged (c) cycle aged. Second row: BSE-SEM images for (d) pristine e) calendar aged (f) cycle aged. Third row: EDX maps for (g) pristine (h) calendar aged and (i) cycle aged cell for identification of Si (green) and Gr (red).

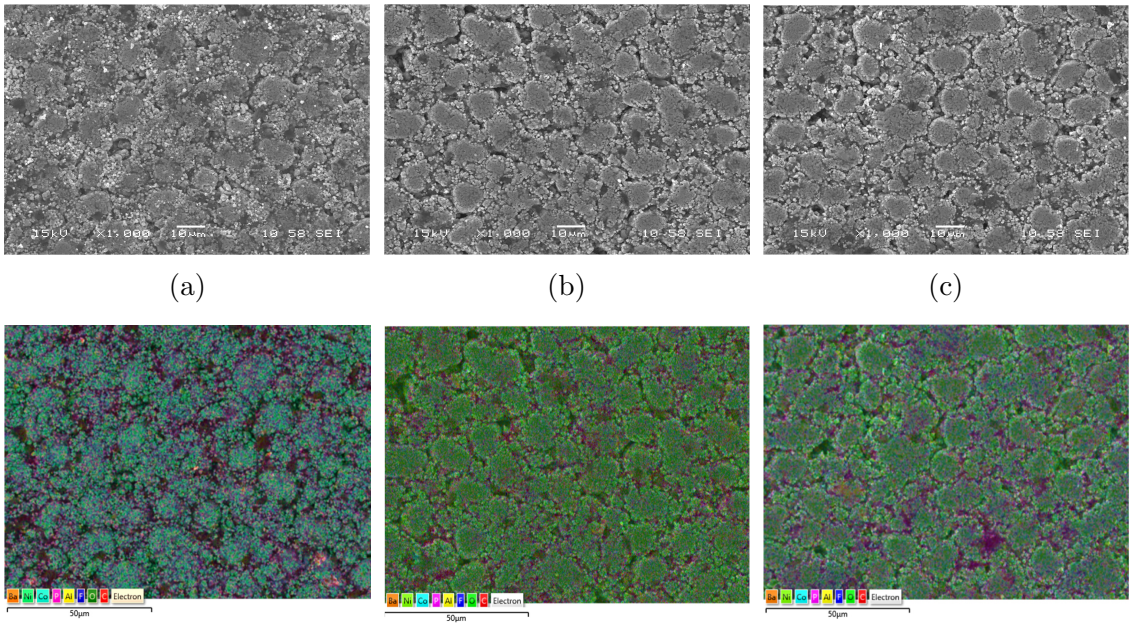

(a) (b) (c)

(d) (e) (f)

Figure 2.17: SEM and EDX images of an NCA cathode harvested from a full cell. First row: BSE-SEM images for (a) pristine b) calendar aged (c) cycle aged cell. Second row: EDX maps for (d) pristine (e) calendar aged and (f) cycle aged cell.

Chapter 3

Degradation-adaptive single particle model

Building on the ageing results found in the previous chapter, Chapter 3 now presents a comparative study of changes in a subset of battery electrochemical parameters throughout life, considering the same NCA/Gr-Si cells as before. Can periodic parameter updates throughout battery life replace the direct inclusion of degradation models? The goal of the study is to identify the main degradation modes that occur and to track transport and kinetics changes throughout battery lifetime by adjusting model parameters. It is concluded that the parameters impacted by ageing include diffusion time, stoichiometry, active material volume fraction and kinetic rate constant. The impact of this work is two-fold. Firstly, it is demonstrated how the SPM can be used to accurately simulate both pristine and aged cell voltage responses if the model parameters are updated accordingly. From a BMS perspective, this ensures accurate state of charge, power etc. estimation throughout life, and maximum use of available capacity. Secondly, this study provides qualitative insight into the impact of ageing on model parameters, which may inform safety issues such as increased heat generation.

3.1 Introduction

The limitations of currently used battery models and state observers often result in a lithium-ion battery not being utilised to its full potential [100]. This becomes more pronounced as the battery ages, because most predictive models use parameters obtained from a brand new cell. Additionally, aged cells may experience increased heat generation leading to safety concerns and higher cooling system energy consumption.

Electrochemical continuum models based on porous-electrode theory provide a good representation of the internal processes of a battery, including the conservation of mass and charge in the electrodes and electrolyte, energy conservation, and reaction kinetics [19]. Estimating some electrochemical model parameters can be achieved through thorough tear-down procedures. However, reparametrisation of model parameters as a battery ages is almost impossible in commercial cells, because half cell potentials change with respect to one another and commercial batteries do not typically contain reference electrodes.

Conventionally, degradation effects can be included in the existing models by coupling them with specific degradation mechanisms models [160] such as SEI growth [68], lithium plating [161], cracks propagation [162], LAM [163], electrolyte oxidation [164], loss of ionic contact [165]. However, this approach adds complexity to the model and requires accurate assumptions/prior knowledge/quantification about specific degradation mechanisms. While this is useful to understand the degradation processes, the onboard application in the EV requires a simpler approach. Therefore, this chapter focuses on a comparative ageing study of changes in a subset of parameters of an electrochemical model as a battery ages, aiming to identify the main degradation modes tracking transport and kinetics changes throughout lifetime.

Table 3.1: Summary of controlled environmental degradation conditions, end of life (EOL) capacity, and capacity fade across groups A-C. Initial capacity for all cells was 3.40 Ah.* 3 months rest due to COVID-19 lab closure.

Cell Group	Degradation conditions	EOL capacity	Calculated capacity fade
A	35 months storage at ∼50 % SOC and 10 ℃	3.38 Ah	0.6%
B	18 months of storage at 50 % SOC and 10 °C, 12 months calendar ageing at 75 % SOC, 45 °C , with 3 months rest at 23 °C in-between*, 5 months storage at ∼50 % SOC and 10 ℃	3.14 Ah	7.6%
C	18 months of storage at 50 % SOC and 10 ℃, 9 months continuous 2A charge-discharge CC cycling at 45 ℃, with 3 months rest at 23 °C in-between* 5 months storage at ∼50 % SOC and 10 ℃	2.67 Ah	21.5%

3.2 Experimental

3.2.1 Degradation procedure

The same group of NCA/Gr-Si cells as described in Chapter 2 was used in this study. The full accelerated ageing procedure is described in Chapter 2, Section 2.2.3, with the resultant capacity loss and ageing conditions summarised in Table 3.1.

3.2.2 Parametrisation

Battery tear-down and a set of standardised parametrisation procedures described in [83] were also performed to obtain additional electrode specific electrochemical parameters required for the model. Half-cells described in Section 2.2.2.2 were subjected to a galvanostatic intermittent titration test (GITT) consisting of 600 s long 1.25 A current pulses with 2 h rest periods between pulses, at zero current. All of the resulting model parameters for a pristine cell are summarised in Table 3.3.

3.2.3 Training and validation data collection

Before and after ageing, all groups of cells were subjected to non-destructive characterisation tests to enable model parametrisation. A C/20 constant current (CC)

Table 3.2: List of experiments for model parameterisation, training, validation and the heat study.

Experiment	**Purpose**
C/20 CC discharge	Calculate cell capacity
GITT	Estimate solid diffusion constant
Artemis motorway drive cycle	Model training
C/2 CC discharge	Model validation
C/1 and C/3	Heat study

discharge was used to calculate cell capacity. This was followed by GITT consisting of 600 s long C/10 current pulses with 2 h rest periods between pulses, at zero current. Upon completion of the ageing protocol, one cell from each group was chosen at random as representative for that group and used for the model parametrisation and heat study. An Artemis motorway drive cycle [166] scaled for maximum 1C current was used for model parameter estimation, C/2 CC discharge test was used for model validation and 1C and C/3 CC discharge tests were used for the heat generation study. The tests are summarised in Table 3.2.

The experiments were conducted using a Maccor 4200 series battery cycler, with temperature measured on the surface of each cell with T-type thermocouples (±0.5 °C, RS Pro). The thermocouples were calibrated against an Omega P-M series RTD (class A) in a thermal bath (Julabo 900 F). For temperature stability, all cells were placed in a thermal chamber set for 20 °C. To avoid uneven forced convection the thermal chamber fan was switched off throughout duration of all tests except the GITT.

3.3 Modelling approach

To gain a better understanding of the influence of ageing on an electrochemical model, a simulation of an isothermal SPM was undertaken using COMSOL with MATLAB LiveLink. The SPM was selected for its ability to provide a simplified yet accurate representation of electrochemical processes, with reduced number of parameters re-

Table 3.3: Summary of pristine cell parameter estimates; Ψ_+ and Ψ_- are positive and negative electrode parameters respectively.

Parameter	Description	Ψ_+	Ψ_-	Method
	Parameters that are assumed constant throughout life			
L	Coating thickness (μm)	71.5	83.3	Measured (per side)
A	Electrode active area (m^2)	0.036285	0.036285	Measured
R_p	Mean particle radius (μm)	1.2	1	Measured
α	Charge transfer coefficient (−)	0.5	0.5	Assumed
c^{max}	Maximum concentration of Li in solid material (mol/m^3)	48000	31398	Theoretical/estimated
	Initial values of parameters subsequently tracked with ageing			
D	Diffusion coefficient (m^2/s)	1.9e-16	function	Estimated from GITT
x	Stoichiometry at 100% SOC (−)	0.26	0.74	Estimated
ε_s	Active material volume fraction (−)	0.8	0.875	Measured
k	Kinetic rate constant (m/s)	5.5e-11	5.5e-11	Optimised

quired. The mathematical description of the model is available in section 3.3.1, below. The aim is to identify the main degradation modes appearing in each group of cells and track battery ageing via model parameter adjustment.

3.3.1 Single particle model equations

In SPM, the transport of lithium into the electrode active material is based on Fickian diffusion,

$$\frac{\partial c(r,t)}{\partial t} = \frac{1}{r^2}\frac{\partial}{\partial r}\left(r^2 D_s \frac{\partial c(r,t)}{\partial r}\right), \tag{3.1}$$

where D_s is the solid diffusion coefficient, c is the degree of lithiation, t is time and r is a spherical coordinate. At particle centre, $r = 0$, and at particle surface, $r = R_p$. There are Neumann boundary conditions,

$$\left.\frac{\partial c(r,t)}{\partial r}\right|_{r=0} = 0, \tag{3.2}$$

$$D_s \left.\frac{\partial c(r,t)}{\partial r}\right|_{r=R_p} = -J(t), \tag{3.3}$$

with the uniform initial condition

$$c(r,0) = c_0, \tag{3.4}$$

where J is the molar flux expressing the rate of the lithium (de)intercalation reaction. In the SPM, molar fluxes are directly related to the applied current (I),

$$J\left(t\right) = \frac{I\left(t\right)}{Fa_{\mathrm{v}}L}, \tag{3.5}$$

where L is the coating thickness and a_{v} is specific active surface area,

$$a_{\mathrm{v}} = \frac{3\varepsilon_{\mathrm{s}}}{R_{\mathrm{p}}}. \tag{3.6}$$

The solid-phase intercalation overpotential is described by the Butler-Volmer equation,

$$J\left(t\right) = Fi_0\left(t\right)\left(\exp\left(\frac{\alpha_- F\eta\left(t\right)}{RT}\right) - \exp\left(\frac{-\alpha_+ F\eta\left(t\right)}{RT}\right)\right). \tag{3.7}$$

For Li-ion cells the electrochemical reactions are relatively efficient, hence it is commonly assumed for the reaction to be symmetrical, which results in $\alpha_- = \alpha_+ = 0.5$, and Eq. (3.7) can be rewritten for overpotential η, as

$$\eta\left(t\right) = 2\frac{RT}{F}\sinh^{-1}\left(\frac{FJ(t)}{2i_0\left(t\right)}\right). \tag{3.8}$$

Here J is molar flux, i_0 is the exchange current density, F is Faraday's constant and R is the gas constant. The exchange current density depends on initial electrolyte concentration (c_1^0), surface lithium concentration in solid phase, maximum (also reference) lithium concentration in solid phase ($c^{\max}$), and kinetic rate constant (k),

$$i_0\left(t,c\right) = Fk\sqrt{c_1^0}\sqrt{c^{\mathrm{s}}\left(t\right)}\sqrt{c^{\max} - c^{\mathrm{s}}\left(t\right)}. \tag{3.9}$$

Finally, the cell voltage expression is given by

$$E(t) = E_{\text{OCP,+}}(x_+(t)) - E_{\text{OCP,-}}(x_-(t)) + \eta_+(t) - \eta_-(t), \tag{3.10}$$

where $x_\pm$ refers to the surface stoichiometry of each particle, defined $x_\pm = c^{\text{s}}/c^{\text{max}}$, and subscript '$\pm$' refers to positive and negative electrode.

3.3.2 Diffusion time

The literature shows that all standard battery electrochemical models (SPM [25], SPM with electrolyte [19], DFN [24]) are sensitive to the selected solid diffusion coefficient values. In most of these models the diffusion coefficient is taken as a constant [19, 29, 167], however, in some cases it is even adjusted between datasets to match the experimental data [29]—this does not necessarily have physical grounds since one does not generally expect diffusion time to change with C-rate. An additional complication to the state of charge dependency of diffusion is battery ageing. With the irreversible morphological changes experienced by the particles (e.g., cracking or volume expansion) the Fickian diffusion coefficient is expected to change as well. To explore the value of a degradation- and SOC-varying diffusion coefficient, we assume here that diffusion coefficient is a function of stoichiometry, and we introduce a diffusion ageing parameter to account for any diffusive or morphological changes induced by ageing.

A direct comparison of relaxation times of the investigated cells (Fig. 3.1) suggests that the diffusion time may increase as cell ages. To quantify the increase of the relaxation times, a common condition was imposed on all cells, namely a cell was considered to reach pseudo-thermodynamic equilibrium if its voltage change is less than 10 mV/h. The time needed to reach this condition by a reference cell is approximately 1 h, while for a cyclic-aged cell this duration increases by 2.5 times, as

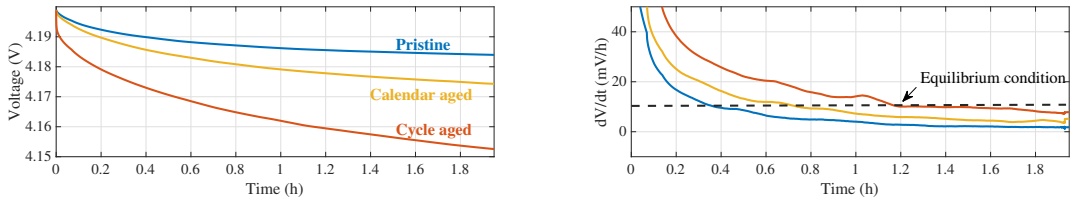

(a) (b)

Figure 3.1: (a) Voltage relaxation profile and (b) voltage change following 0.5C CCCV charge at 20 ℃ for pristine, calendar aged and cycle aged cells.

shown in Fig. 3.1.

Conventionally, Fickian diffusion is described by a diffusion timescale, which may be estimated, via some modelling assumptions, from GITT measurements, potentiostatic intermittent titration tests (PITT) or electrochemical impedance spectroscopy (EIS). Other approaches involve Bayesian estimation [168], and direct model fitting to the experimental data [169]. In this work, Sand's approach [170] is considered. For individual electrodes, characteristic diffusion time constant t_D can be estimated from GITT data, according to

$$\frac{1}{t_D} = \left(\frac{D_\mathrm{s}}{R_\mathrm{p}^2}\right) = \frac{4}{\pi}\left(\frac{I}{3\varepsilon_\mathrm{s} F A L}\frac{\mathrm{d}E_\mathrm{OCP}/\mathrm{d}c}{\mathrm{d}E/\mathrm{d}\sqrt{t}}\right)^2, \tag{3.11}$$

where D_s is diffusion coefficient, R_p is effective particle radius, A is electrode plate area, L is electrode thickness, F is Faraday constant, E_OCP is open circuit potential, c is lithium concentration, I is applied current, E is measured voltage, and t is time.

However, for the analysis of full cells' response, a different metric, not requiring half-cell specific parameters is needed. For this reason only term $\left(\frac{\mathrm{d}E_\mathrm{OCP}/\mathrm{d}c}{\mathrm{d}E/\mathrm{d}\sqrt{t}}\right)^2$ from Eq. (3.11) is used for pristine and aged cells comparison. The results are plotted in Fig. 3.2 for pristine, calendar and cycle aged cells. Observations indicate that the profile of the time constant of calendar-aged cells exhibits a similar magnitude and shape to that of pristine cells. However, it appears to be compressed along the capacity axis, which can be attributed to electrode balancing changes (confirmed with

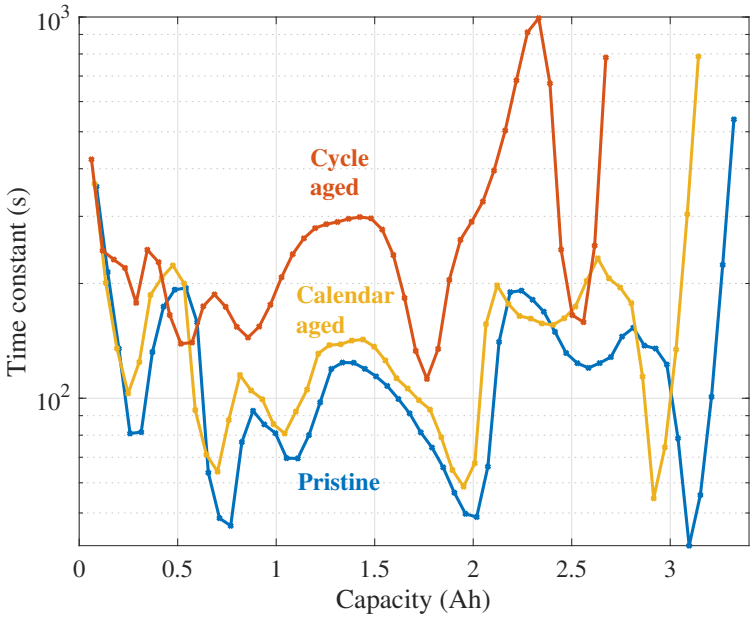

Figure 3.2: Diffusion time profiles for pristine, calendar-aged and cycle-aged cells.

DVA). In contrast, for the cycled aged group there is both a horizontal compression and a large increase in the magnitude of the characteristic time constant, reflecting longer relaxation times that could be caused by ageing. This points that diffusion time is an important ageing parameter, although it is often assumed constant in the literature [19] [29] [167].

Additionally, Fig. 3.2 reveals a strong dependency of diffusion time constant on SOC. However, it is important to note that the method used for estimating characteristic time constant may be affected by OCP gradients, and as they tend to zero the voltage change with respect to concentration drops to zero, making diffusion time constant unindentifiable [40].

3.3.2.1 Half cell diffusion coefficient estimation

By using Eq. 3.11 and taking electrode-specific parameters from Table 3.3, it is possible to estimate the diffusion coefficient for a pristine anode and cathode. Based on the graphite to silicon proportion in the anode composition (90 wt % Gr and 10 wt

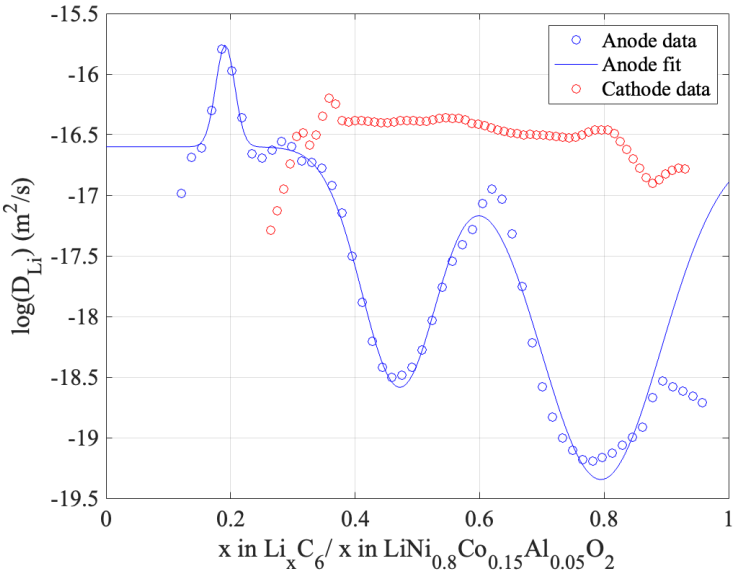

Figure 3.3: In blue colour - GITT measurement and fit of diffusion for the anode, using graphite particle radius of 1 um. In red colour - GITT measurement of NCA cathode, using NCA particle radius of 1.2 um.

%), an assumption is made that anode particle size is reflected mainly by graphite and any expansion effects are neglected. To account for variations across the SOC range, the diffusion coefficient for both anode and cathode is plotted with respect to the degree of lithiation in Fig. 3.3.

Here MATLAB curve-fitting toolbox was used to define the diffusion coefficient function for the anode, with the resultant fit illustrated in Fig. 3.3. The fitted empirical anode diffusion coefficient as a function of stoichiometry (x) is given by:

$$D_{-} = c_0 + a_1 \exp\left(-\frac{(x-b_1)^2}{c_1}\right) + a_2 \exp\left(-\frac{(x-b_2)^2}{c_2}\right) + a_3 \exp\left(-\frac{(x-b_3)^2}{c_3}\right), \tag{3.12}$$

with $a_1 = -1.975$, $a_2 = -2.746$, $a_3 = 0.8401$, $b_1 = 0.4712$, $b_2 = 0.7948$, $b_3 = 0.1914$, $c_0 = -16.6$, $c_1 = 0.007297$, $c_2 = 0.01883$, $c_3 = 0.0004597$.

The diffusion coefficient function for the NCA cathode exhibits significantly smaller variation across the degree of lithiation, therefore, it is assumed constant in this study. The resultant cathode diffusion coefficient constant and anode diffusion coefficient

function are then used as a direct input to the model. Given the observed increase in diffusion time for cycle-aged cells, an additional diffusion ageing parameter, λ_{D_-}, is introduced. The scaling factor λ_{D_-} premultiplies the D_- term in the model and effectively, any change in diffusivity, particle size or both caused by ageing manifests in a λ_{D_-} change.

It is worth noting that the effects of the characteristic volume expansion/contraction of silicon [66], are not included in the SPM particle definition (particle radius assumed constant). However, the volumetric changes are reflected in the measured OCP of the anode.

3.3.3 Selection of parameters to track during ageing

To choose the most appropriate parameter subset for tracking during ageing, the initial quantification of the degradation modes experienced by each group of cells conducted in Chapter 2 was used. The full range of the DVA ageing markers was shown already in Fig. 2.12, and a simplified version of this figure, showing only the resulting markers, is attached below.

In the case of the calendar-aged cells, the capacity fade Q_{full} seems to be caused mostly by loss of lithium inventory (LLI) [154], which manifests in electrode balancing changes $Q_{\text{LLI balance}}$ that shift the stoichiometry of the cell $x_{\pm}$. Based on Fig. 3.2, the diffusion time λ_{D} does not significantly change during calendar ageing. The kinetic rate is assumed constant with SOC, and equal in both anode and cathode—it is expected to change with calendar ageing at elevated temperatures due to SEI side reactions. Therefore, the *tracked ageing parameters* for calendar aged cell were selected to be the stoichiometry at 100 % SOC x_+ and x_- and the kinetic reaction rate constant k_-.

In contrast, for the cycled group of cells in Fig. 3.4 we observe a substantial decrease in anode capacity $Q_{\text{LAM,NE}}$, resulting from loss of the active material (LAM)

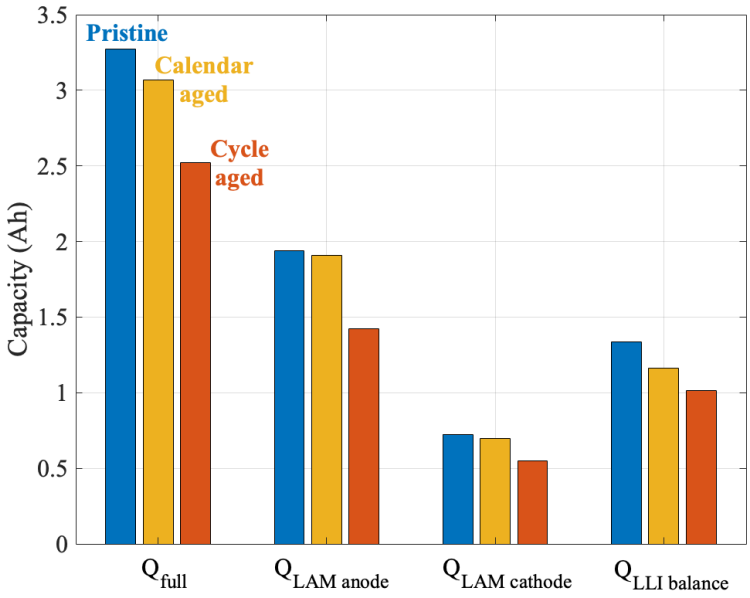

Figure 3.4: Ageing markers extracted from DVA of charge data for pristine cells at beginning of life, plus calendar- and cycle-aged cells at end of life. The evolution of these ageing markers across all reference performance tests is available Chapter 2

[61] which decreases the accessible area on the electrode. Since A_- and $\varepsilon_{s,-}$ are linked geometrically (for a constant effective particle radius), according to Eq. (3.6), we therefore assume that only $\varepsilon_{s,-}$ changes.

The reason for the loss of active material was not identified, but one explanation involves changes in the particle size [146]. Interestingly, Fig. 3.2 shows a substantial magnitude change in the diffusion time for the cycle-aged cells—this could be influenced by particle morphology changes. The specific reason cannot be unequivocally identified, but λ_{D_-} is expected to change. Additionally, an electrode balancing shift $\mathrm{Q}_{\mathrm{LLI\ balance}}$ is observed, therefore changes in x_+ and x_- are expected for the cycle-aged cells. Fig. 3.4 also shows a decrease in cathode capacity $\mathrm{Q}_{\mathrm{LAM,PE}}$, however, both electrode parameters cannot be simultaneously fitted uniquely. Based on more severe degradation experienced by the anode, confirmed in Chapter 2 it is assumed here that only the anode parameters are changing, while cathode parameters are held constant. In summary, the *tracked ageing parameters* for the cycle-aged cells are the

diffusion ageing factor λ_{D}, stoichiometries at 100% SOC x_+ and x_-, kinetic reaction rate constant k_-, and active material volume fraction $\epsilon_{\mathrm{s,-}}$.

3.3.4 Parameter optimisation

To track the subset of ageing parameters discussed in the previous section, we minimised the cost function given by Eq. (3.13)—this is a standard least-squares minimisation problem solved with MATLAB `lsqnonlin`, aiming to identify the parameters that give the optimal fit between model simulated and experimentally measured battery voltage. The optimisation problem can be written as

$$\begin{aligned} \min_{\theta} \sum_{i=1}^{N} \left(E_i^{\mathrm{sim}} - E_i^{\mathrm{exp}}\right)^2, \\ \theta = \{\theta_1, \theta_2, \ldots \theta_n\}, \\ \theta_k^l \leqslant \theta_k \leqslant \theta_k^u, \end{aligned} \tag{3.13}$$

where the superscripts sim and exp represent simulation and experimental measurements. The index i corresponds to the entries in time t of the experimental and simulated voltages, and N is the number of measurement points i for each experiment. Parameters were constrained between upper and lower bounds. For each group of cells, the optimised parameter sets are

$$\theta_{\mathrm{pristine}} = \{x_+, x_-, k_-\}, \tag{3.14a}$$

$$\theta_{\mathrm{calendar}} = \{x_+, x_-, k_-\}, \tag{3.14b}$$

$$\theta_{\mathrm{cycle}} = \{x_+, x_-, k_-, \varepsilon_{\mathrm{s}-}, \lambda_{D_-}\}. \tag{3.14c}$$

3.4 Heat balance

The secondary objective of this chapter was to offer a qualitative understanding of how battery ageing affects heat generation. The battery heat generation problem is treated separately to the electrochemical model, given that inclusion of thermal dependency in the SPM requires an assumption about temperature evolution over battery ageing and significantly increases the number of parameters in the model. Therefore, a simplified heat balance relation is used to track reversible and irreversible heat contributions changes across battery lifetime. The use of a zero-dimensional (i.e. lumped) thermal model is reasonable since the cells are in a thermal chamber with the fan turned off, which results in a low heat exchange with the environment. Therefore, as discussed in Brosa Planella et al. [26], the heat transfer within the cell is fast in comparison to the heat transfer to the environment, and the temperature gradients in the cell are negligible (i.e. low Biot number).

To understand how the heat signature changes over the battery lifetime, both reversible and irreversible thermal contributions are investigated. The irreversible heat defined in this work describes the reaction heat (Q_{irr}) as a lumped enthalpy of reaction, enthalpy of mixing and enthalpy of phase change. The Q_{irr} is calculated from the potential difference

$$Q_{\text{irr}} = I(E - E_{\text{OCP}}). \tag{3.15}$$

The irreversible heat can be further decomposed into ohmic heat (Q_{ohm}), and reaction contributions. To calculate the ohmic heat, the following equation is used ,

$$Q_{\text{ohm}} = I^2 R_{\text{ohm}}. \tag{3.16}$$

The ohmic resistance was derived using the same methodology as described in Section

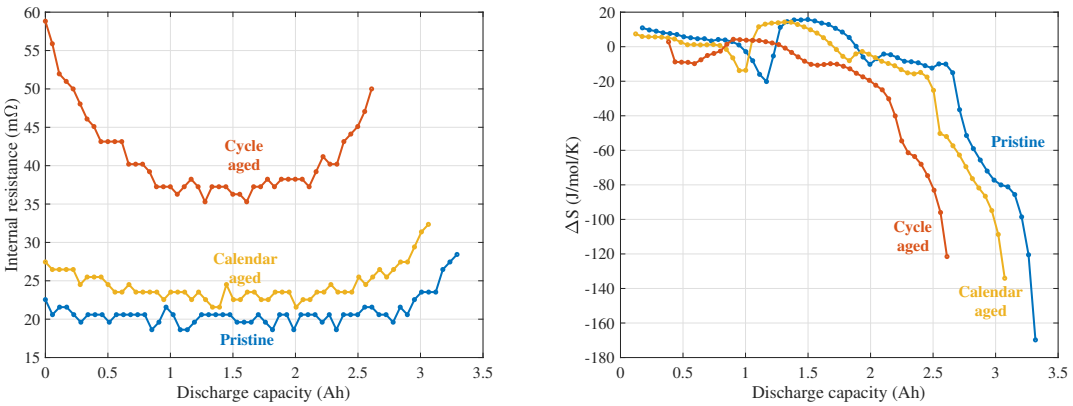

(a) (b)

Figure 3.5: (a) Internal resistance calculated based on initial (1 s) voltage drop following applied current pulse from the GITT for pristine, calendar aged and cycle aged cells. (b) Total cell entropy with respect to discharge capacity for pristine, calendar aged and cycle aged cells.

2.3.2.6, however here different equipment was used (outlined in Section 3.2.3), as well as cells were subjected to additional 5 months of storage. Extracted values of the internal resistance R_{ohm} for all cells are shown in Fig. 3.5a.

For the pristine cell, the R_{ohm} values remain relatively constant throughout the SOC, with a slight increase observed at the beginning and end of discharge. The calendar aged cell exhibits a similar profile, but with a slight increase in magnitude from 20 mΩ to 23 mΩ at 50 % SOC. The R_{ohm} profile of the cycle aged cell is significantly different from the pristine case. At around 50 % SOC the R_{ohm} has doubled in magnitude. Additionally, at the beginning of discharge, the R_{ohm} value increased from approximately 22 mΩ to 60 mΩ. The increase in internal resistance is likely due to the LAM and SEI growth given the battery cycling history at elevated temperatures.

One implication of such a significant increase in internal resistance is a rise in the irreversible heating for aged cells. Secondly, the upper voltage limit of the cell is reached faster. Consequently, to achieve the fully charged state using a CCCV profile, a longer CV phase is required. In addition to extending the charging time, maintaining the battery at a higher voltage is an additional stress factor. As shown

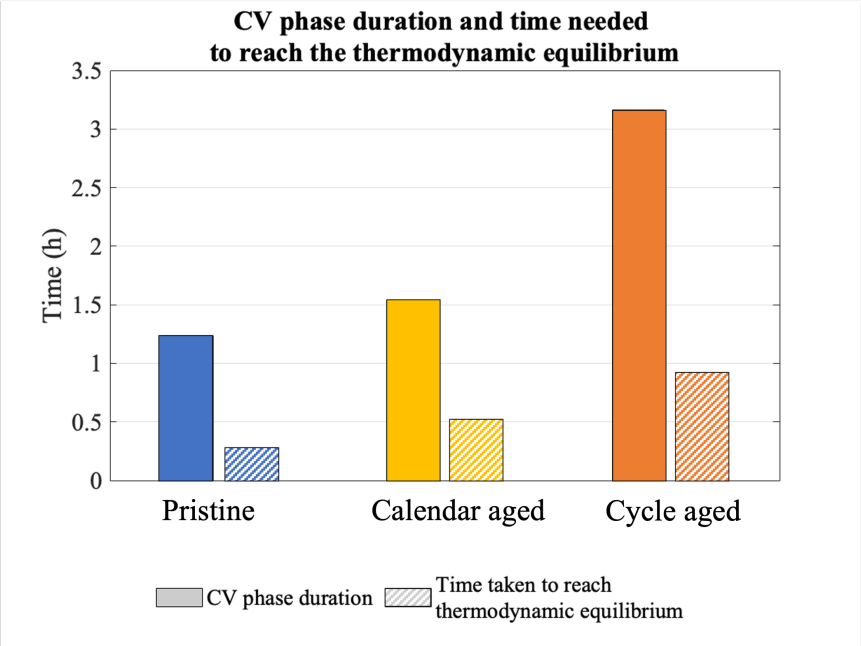

Figure 3.6: Comparison of CV phase duration and the time needed to reach thermodynamic equilibrium after 0.5C CCCV charge at 20 °C for pristine, calendar aged and cycle-aged cells.

in Fig. 3.6, the CV phase lasts 2.5 times longer for the cycled cell compared to the pristine cell. Furthermore, the increase in the CV phase duration is correlated with the time required for the battery to reach an equilibrium condition (in this study defined as $\mathrm{dV/dt} < 10\,\mathrm{mV}$) due to the increase in the diffusion time.

The second source of heat in the heat balance Eq. (1.3) comes from the entropy change. The entropy change relates to the reversible heat through the following expression:

$$Q_{\mathrm{rev}} = IT\frac{\Delta S}{nF}, \tag{3.17}$$

where ΔS is the reaction entropy (as previously discussed). The comparison of pristine full cell reaction entropy change against calendar aged and cycle aged cells is shown in Fig. 3.5b. The magnitude is comparable between the pristine and calendar aged cells, and therefore it is expected that the entropic contributions will be similar for of these both cells.

Table 3.4: Heat balance equation parameters.

Symbol	Description	Value	Unit
h	heat transfer coefficient	10	$\mathrm{W/m^2/K}$
A	cooling area	0.00418	$\mathrm{m^2}$
Cp	specific heat capacity	2700	J/kg/K

The heat transfer to the surrounding environment (Q_{conv}) is described by Eq. (3.18), where heat transfer coefficient h takes a value of $10\,\mathrm{W/m^2/K}$ to account for a natural convection in a closed thermal chamber; A describes cell cooling area, T is a measured temperature at the surface of the cell, and T_{ref} is a reference temperature. Heat of radiation is neglected. The parameters used for simulation are given in Table 3.4.

$$Q_{\mathrm{conv}} = -hA(T - T_{\mathrm{ref}}) \tag{3.18}$$

3.5 Results and discussion

Following the optimisation procedure, a set of *tracked ageing parameters* was extracted for each cell and is summarised in Table 3.5. Simulated voltages match well with the training dataset, with low root mean squared errors (RMSE), see Fig. 3.7. To validate the model, the parameters from Table 3.5 were used as input to the model and a new scenario was simulated; 2C CC discharge. The results are shown in Fig. 3.8, with the voltage RMSE ranging between 24 mV to 27 mV between data-sets.

In the case of the calendar aged cell, which experienced LLI, as expected, the stoichiometric limit on the anode decreased. Additionally, the kinetic rate constant decreased, suggesting an increase in either specific surface area, resistance, or both. The increase in resistance may have been caused by SEI growth. The cycle-aged cell experienced a decrease in active material volume fraction, corresponding to a loss of

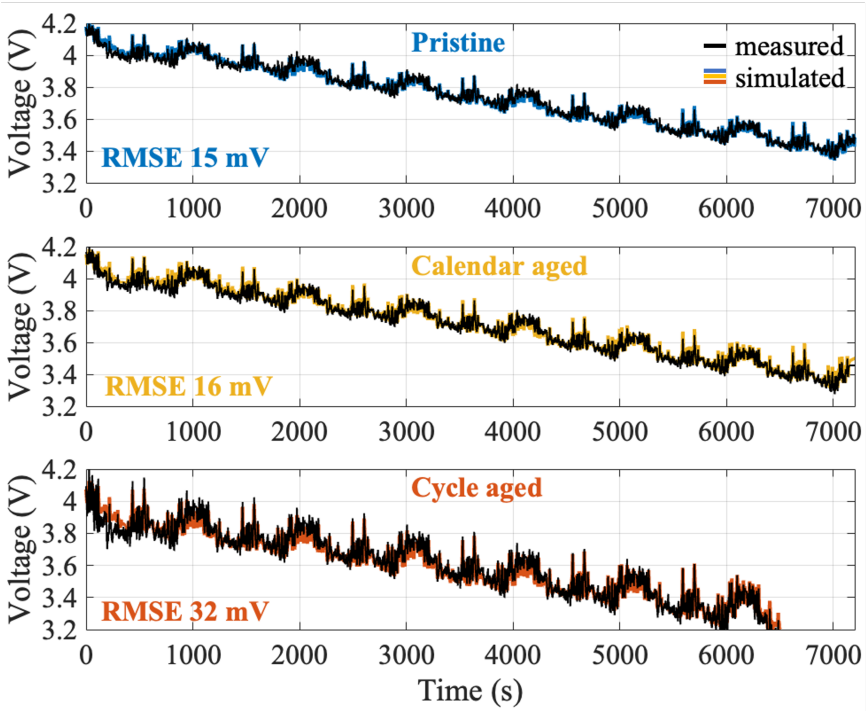

Figure 3.7: Model training - Artemis motorway drive cycle voltage simulation results for pristine, calendar-aged and cycled-aged cells.

active material in the anode and a stoichiometric shift due to LLI. Diffusion time and kinetic overpotential both increased with cyclic ageing. The voltage prediction accuracy decreased in the cycle aged cell, possibly due to cathode degradation which is not accounted for in the model. Nonetheless, model accuracy remained at an acceptable level. To highlight the importance of changing parameters during ageing, a model response using pristine reference parameters was simulated and compared to the cycled cell, and the RMSE increased to 178 mV.

The results of the heat balance simulations using CC discharge for pristine and aged cells at 1C and C/3 are shown in Fig. 3.9. The isolated heat profiles indicate a noticeable increase in both entropy and reaction heating due to overpotentials at the end of discharge. The constant applied current results in a consistent ohmic heating profile with a slight increase at the end of discharge. However, for the cycle-aged cell, the substantial increase in internal resistance at the start of discharge leads to an initial increase in ohmic heating, as seen in Fig. 3.9e. For the pristine cell

Table 3.5: Optimisation parameters results for groups pristine, calendar aged and cycle aged cells. The [-] denotes an unchanged value (reference value).

Optimisation parameter	Pristine	Calendar aged	Cycle aged
x_-	0.74	0.7	0.7
x_+	0.26	0.27	0.35
$\varepsilon_{s,-}$	0.875	-	0.7
k_-	5.8e-11	4e-11	2.8e-11
λ_{D-}	1	-	0.7

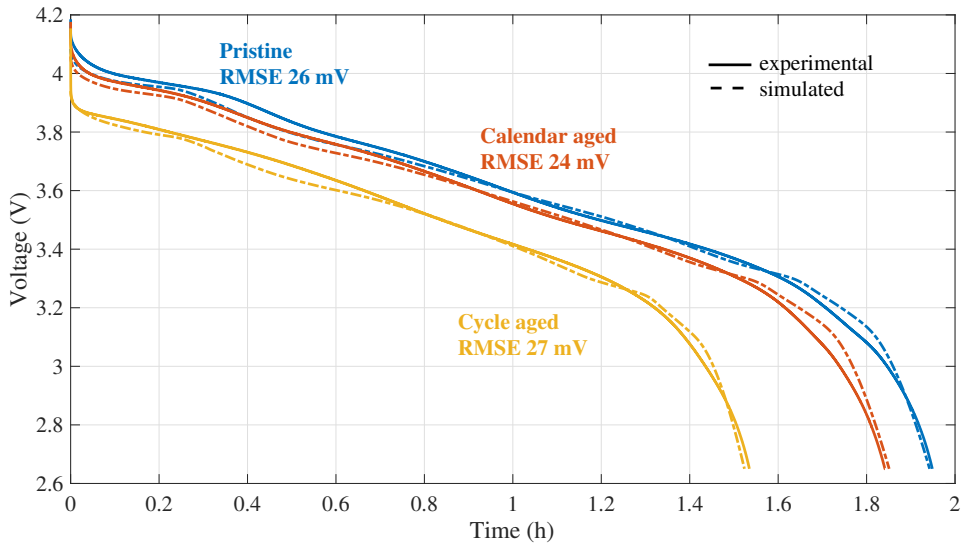

Figure 3.8: Model validation - C/2 CC discharge voltage simulation results for pristine, calendar-aged and cycled-aged cells.

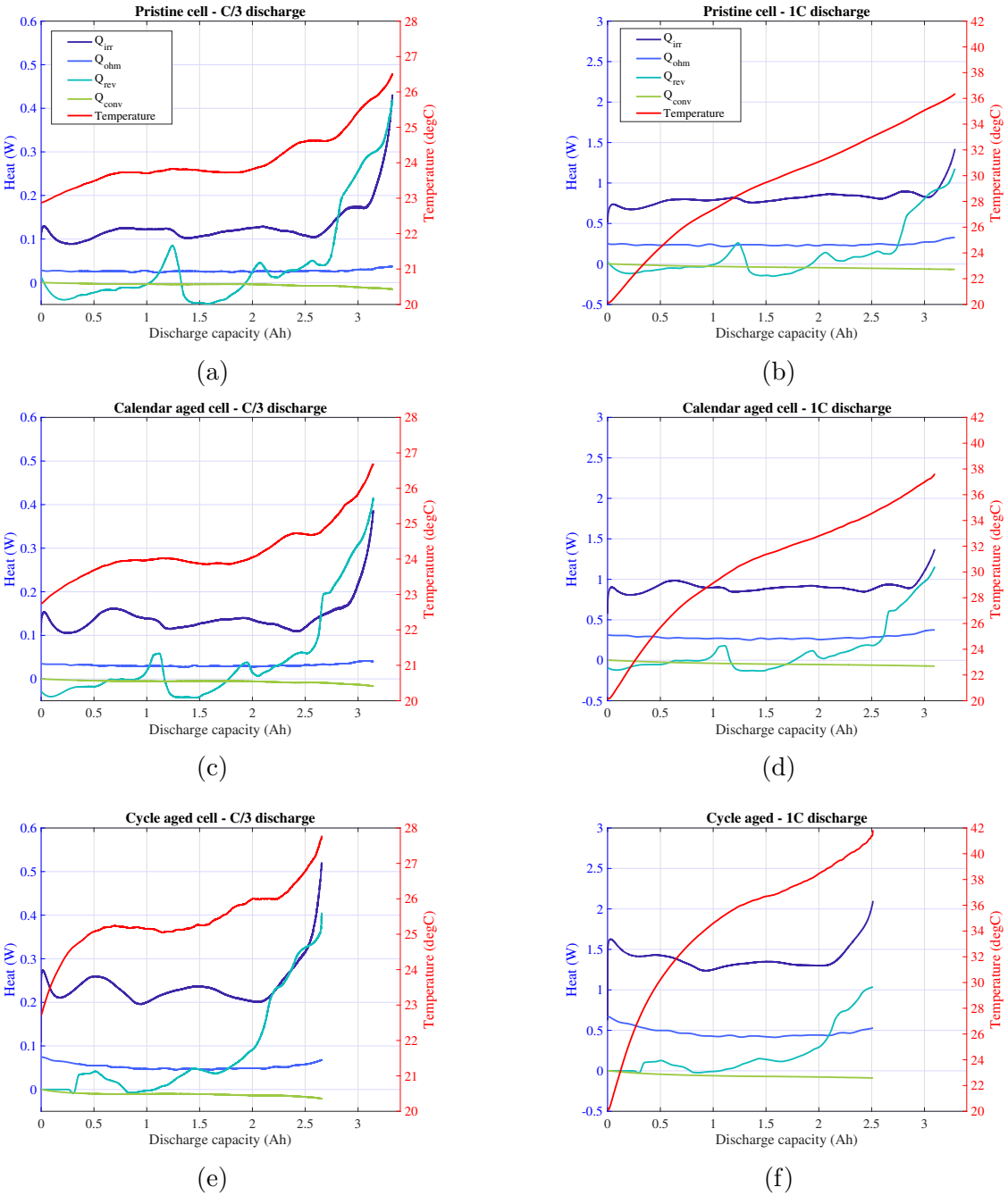

Figure 3.9: Heat generation across $C/3$ discharge (first column) (a), (c), (e) and across $1C$ discharge (second column) (b), (d), (f) for pristine, calendar aged and cycled aged cells.

at a 0.3C discharge rate, the cooling effect of entropy is evident in the temporary drop in cell temperature. As the entropy becomes more negative for the aged cell, the resultant temperature profile becomes smoother due to the reduced total cooling effect on the cell. At a 1C discharge rate, the entropy contribution is too small to have a noticeable effect on the battery temperature curve. The difference between the maximum temperatures between pristine and aged cells during a 0.3C discharge is only 1 °C, but this difference increases to 5 °C (36 °C for pristine and 41 °C for cycle-aged) during a 1C discharge.

In Fig. 3.10 the reversible and irreversible heat contributions are compared. The calendar-aged cell performance is nearly the same as the pristine cell group, even though the parameter optimisation revealed a decrease in k_{-}. The kinetic rate constant is directly linked to the irreversible heat generation, which is the main contributor to the total heat generation in the cells. The reversible heat in contrast contributes only 18% of total heat generation at C/3. The proportion of reversible heating decreases with C-rate increase. Cycle-aged cells experienced ≈50% rise in irreversible heat generation during 1C discharge, demonstrating the significant impact of ageing on battery thermal performance. Changes in irreversible heating with cycle age are discussed in Chapter 2, and although (for discharge) the absolute value of the entropic heat increases with cyclic ageing, the irreversible heat rise is significantly higher, making the entropic contribution relatively smaller than in a pristine cell. The rise in irreversible heating is attributed to the significant decrease in k_{-}.

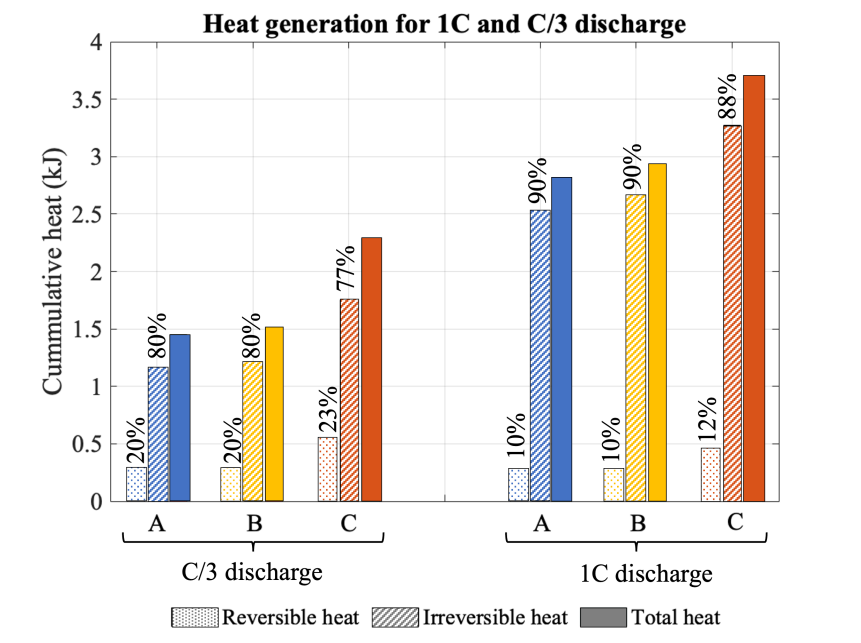

Figure 3.10: Heat generation across pristine, calendar-aged and cycle-aged cells for C/3 and 1C discharge.

3.6 Conclusions

This chapter examined the impact of calendar and cycling ageing on the transport and heat generation of an NCA/Gr-Si cell. To achieve this, two batches of cells underwent accelerated ageing procedures and reference parameters were obtained through separate battery tear-down and half-cell construction. A number of parameters were found to change with ageing: diffusion time, stoichiometry, active material volume fraction, and kinetic rate constant. It was necessary to limit degradation to one electrode only, due to the parameters of both electrodes being unidentifiable without a reference electrode. To account for diffusion changes as the battery ages, an additional diffusion ageing parameter is introduced. For the calendar aged cell, the adjustable anodic parameters effectively became the stoichiometry and kinetic rate constant. For the cycled aged cell, the adjustable anodic parameters were the active material volume fraction, kinetic rate constant, stoichiometry, and diffusion coefficient. To improve model identifiability, the diffusion in the anode was taken as a function of

lithiation.

The optimal values for all control parameters were obtained from an optimisation set to minimise the error between a simulated and experimental voltages. The model showed good fit of the measured output across all cells, with the RMSE ranging from 15 mV for pristine to 32 mV for cycled cell.

The main degradation mode revealed for the calendar-aged group was LLI, which resulted in a stoichiometric shift. This was accompanied by a decrease in kinetic rate, perhaps caused by anode SEI growth or geometry changes. No significant changes in diffusion time for this group were noticed. There was a negligible change in the heat generation between the pristine and the calendar-aged cell. On the other hand, the cycle-aged group experienced a decrease in the active material volume fraction, corresponding to LAM in the anode, and a stoichiometric shift due to LLI. Both diffusion time and kinetic overpotential increased with cyclic ageing. This was accompanied by ≈50% rise in irreversible heating.

Overall, we conclude that the accuracy of SPM voltage prediction can be maintained at an acceptable level throughout the battery lifetime if the parameters are updated accordingly.

3.7 Limitations and future work

While the parameter update was successful in the presented study, it is a much more challenging task in an EV or other application. Firstly, it is necessary to make an appropriate assumption to identify the dominant degradation mechanism, which often is coupled with another degradation mode. Although in this study the degradation on the anode was assumed to be prevalent, cathodic changes also happen which further complicates parameter identifiability, especially in later life. Additionally, in an EV application, multiple cells are stacked together, which are likely to undergo

inhomogeneous degradation, and so single-cell parameter adjustment might not be effective to capture the pack behaviour.

The idea presented in this chapter can be extended in two distinct ways with differing goals. Firstly, a more precise model, such as the "many-particle model" by Kirk et al. [171], could be utilised to account for the Si-doped anode. This way, perhaps more information could be learnt from tracking a more accurate representation of kinetic and transport changes over the battery lifetime.

The second approach addresses the applicability problem in an EV application. Here a simpler model than the SPM might be favoured. The equivalent circuit model, which is already used in most onboard battery management systems is a good candidate. Given different parameters used in an ECM, perhaps less information about transport and kinetics can be extracted directly, however, the identifiability challenges of an electrochemical model are avoided and the parameter updates with battery age could be performed without prior analysis of degradation modes.

Chapter 4

High C-rate modelling

This chapter extends the electrochemical modelling approach introduced in Chapter 2 by incorporating a more complex model, and thermal coupling to electrochemical properties. The focus is placed on high current conditions, with the objective of accurate prediction of battery states at 10C, relevant for fast charging. A pseudo-3D continuum thermal-electrochemical model for large-format pouch cells, adapted from Lin et al. [20], was tested following the Chu et al. [37] parametrisation method. For model parametrisation and validation, experimental data was collected from an 8 Ah LFP/Gr pouch cell, cycled at rates from 1C to 10C. An infrared camera was used to record temperature across the cell surface. During the study, it was discovered that the chosen parametrisation method was useful for extracting several variables, but it was unable to capture solid-state diffusion. When this parameter was included in the optimisation procedure, it resulted in a simulation of a solid diffusion-limited process that was unrealistic for the selected cell given its high power capabilities. Based on the tests performed, we concluded that the high-power cell used here did not experience solid diffusion limitations, unlike in the preceding study of Lin et al. [20] that used a similar cell but optimised for energy density rather than power density. Therefore, by combining the parameters returned by the optimiser and assuming infinitely fast

solid-state diffusion, we were able to simulate the model up to 10C CC and achieve accurate voltage and temperature predictions. These results demonstrate that, for a cell optimised for high power (e.g., having thin electrodes), a relatively simple electrochemical model may be used to give accurate predictions of performance, so long as temperature is also modelled, and key properties such as conductivities are a function of temperature.

4.1 Introduction

One significant barrier to widespread adoption of EVs is the issue of charge times. While fast charging may seem like an obvious solution for reducing charging times and removing range anxiety for EV users, it can create a host of challenges when viewed through the lens of battery modelling and management.

The first challenge for high C-rate applications is the (in)ability of a cell to accept charge because some internal limit has been reached. Depending on the cell design, high currents may induce certain limiting conditions. The most common is an electrolyte diffusion-limited process, also known under the name diffusion-limited current. This limitation is encountered when the electrolyte Li+ concentration close to a current collector decreases to zero [172]. The limiting current I_{lim} in Eq. (4.1) from [172] is influenced by several key design parameters, including electrode thickness L, electrolyte effective diffusivity $D_{\text{l,eff}}$, and initial electrolyte concentration c_{l}^0,

$$I_{\text{lim}} = \frac{2zFD_{\text{l,eff}}c_{\text{l}}^0}{L}. \tag{4.1}$$

It can be easily deduced from this that a thick electrode optimised for energy density will encounter a limiting current at lower C-rates than a thin electrode, but this is not the only consideration. During high-rate charging, lithiation of the anode may consume all the lithium ions in the electrolyte around the anode particles (and

vice versa for discharge and cathode), which causes sudden drop in ionic conductivity and effectively cell voltage [173].

A further limitation may happen when the surface concentration of lithium in the particles is either 0 or 100%. The implication is that if the lithiation current at a particle is slower than the diffusion flux can supply, then the surface concentration will eventually reach the limit [173]. When surface concentration reaches 100% on the anode, lithium plating is likely. This is a solid-diffusion-limited process.

Cell modelling that accounts for these limitations becomes even more challenging, and the literature presenting cases above 6C is heavily limited [57, 174]. However, if EVs were to be charged fast (i.e. <10 min), accurate modelling at these high currents is necessary. An additional implication of high currents is increased cell heating. Temperature dependency is commonly accounted for via an Arrhenius relationship for the solid diffusion, electrolyte diffusion, kinetic rate constant and electrolyte conductivity, which further complicates the models. This chapter, therefore, aims to bridge this gap and investigate effective modelling approaches at high C-rates, up to 10C.

4.2 Experimental

To investigate modelling capabilities and limitations at high C-rates, a high-power A123 Systems LFP/Gr 8 Ah pouch cell was selected as the test subject in this chapter. The selected cell was capable of charging at 20C maximum continuous current and discharging at 50C maximum continuous current according to the manufacturer. The cell had the same format, manufacturer and chemistry type as the cell studied in Lin et al. [20]. However, the electrodes were thinner, enabling faster diffusion, at the expense of lower capacity.

4.2.1 Pouch cell disassembly

A pristine cell was fully discharged to 0 V at C/10 constant current and disassembled in an Argon-filled glovebox (Inert PureLab HE). A micrometer with 0.001 mm resolution and ±0.002 mm accuracy was used to measure the current collector thicknesses as well as the coating thicknesses of the electrode materials harvested from the full-cell. The thicknesses were determined by taking an average of five samples from different locations on the electrode.

4.2.2 Experimental setup

An Ivium Octoboost 16000 battery cycler was used for cell cycling, with six 16 A channels connected in parallel to give a total current up to 96 A. A 16 mm^2 wires (CEF) were used for the connections from the cell to each channel to ensure negligible heating of the wires. Two copper bars with large thermal mass were connected to the cell terminals to act as heat sinks. The battery cell holder was manufactured from an acrylic sheet to support free heat dissipation from the largest cell faces. The acrylic frame also acted as an electrical insulator near the tabs and provided very low heat convection at the points of contact with the battery (the known thermal conductivity of the frame was 0.17 W/m/K). To ensure good electrical contact between the tabs

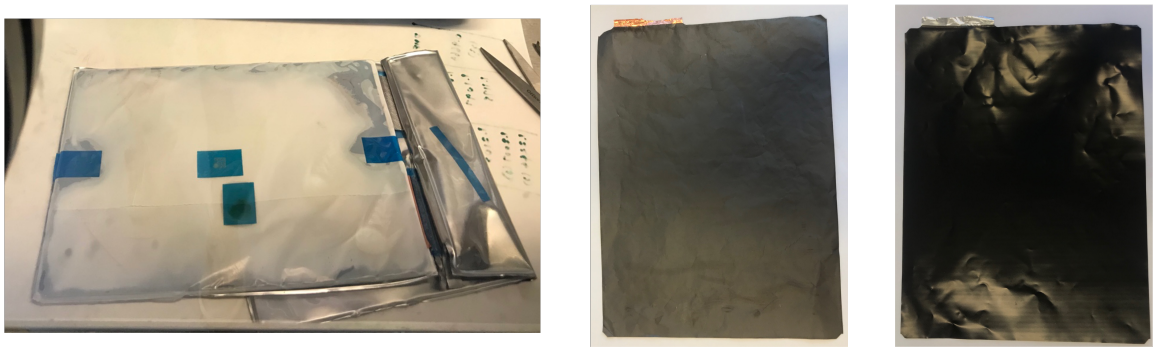

(a) (b) (c)

Figure 4.1: A123 Systems cell tear-down. (a) Pouch disassembly inside the glove box, (b) Gr anode (c) LFP cathode.

and the copper bars, a supporting bar was used to compress the bottom and top acrylic frames.

A thermal imaging camera (FLIR A35sc) was used to perform lock-in thermography alongside measurements of current and voltage, following the procedure proposed by Chu et al. [37]. The camera was positioned at a distance of 0.78 m from the cell surface, as shown in Fig. 4.2. The cell surface was coated with black paint (KRYLON) with known emissivity (0.95-0.97) to eliminate any thermal reflections. In order to provide absolute accuracy, the reference background ambient temperature was subtracted from the IR camera readings based on an independent temperature measurement with an RTD sensor (Omega P-M series class A, $\pm$ 0.1 °C), located behind the reference felt square in the image, shown in Fig. 4.2.

Temperature data from the IR camera was spatially smoothed using the MATLAB function `imgaussfilt`, a 2-D Gaussian filtering method. Fig. 4.3 shows a comparison of the original (unsmoothed) data, and `imgaussfilt`-smoothed data.

The training data for model parametrisation included 2C and 4C square wave tests with 100 s excitation periods (this will be referred to as 4C100 s), and 8C square wave tests with 50 s period (this will be referred to as 8C50 s), performed at 50% SOC. However, it was found that the temperature rise resulting from the 2C pulse was small and insufficient to give a good signal-to-noise ratio using the thermal camera, therefore only the 4C and 8C pulse data sets were used for fitting. The independent validation data set (not used for model parametrisation) consisted of 2C, 4C, 6C, 8C and 10C constant current charge (from 0% SOC to 100% SOC) and discharge (from 100% SOC to 0% SOC).

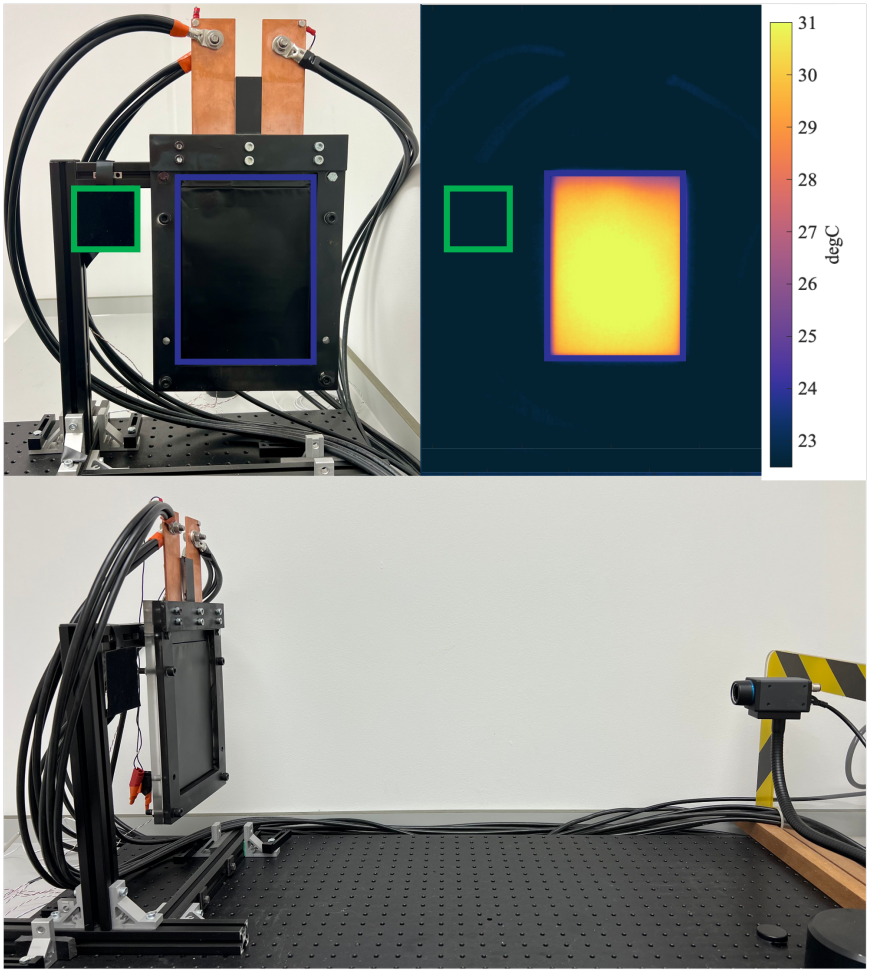

Figure 4.2: Experimental setup. Top picture on the left shows cell holder and tab connections. Cell marked in purple and reference temperature square marked in green. On the right, IR camera reading of the same image. Bottom image shows FLIR camera facing surface of the cell.

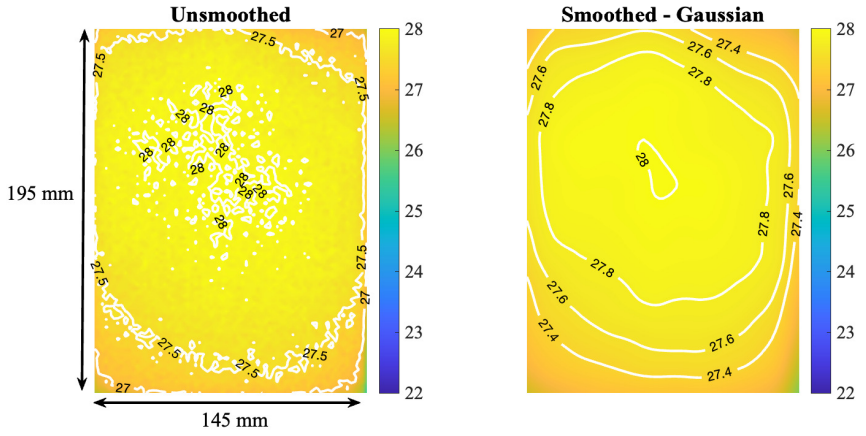

Figure 4.3: Cell surface temperature at the end of 10C CC charge phase. (a) unfiltered IR camera reading. (b) data smoothed with MATLAB `imgaussfilt` with a sigma value of 3.

4.3 Pseudo-3D thermal-electrochemical model

To gain insight into the battery performance during high C-rates, a physics-based model was selected. Additionally, in order to model thermal gradients across the battery surface, the model needed to be resolved in more than one dimension. However, these two requirements substantially increase the computational effort required for the simulation. Therefore, simplification methods from two consecutive previous studies were used—by Chu et al. [37] and Lin et al. [20], who proposed cell layer homogenisation and two types of unique 3D continuum thermal-electrochemical models that are relevant here. The models enabled accurate voltage and temperature predictions at 4C but also substantial model reduction that improved computation speed. This study aims to build on the work by Chu et al. [37] and Lin et al. [20] and verify that the model performance at higher C-rates for selected high-power cells is still reasonable.

4.3.1 Model description

The pseudo-3D continuum thermal-electrochemical model is described as follows. At the microscale level, within the particles, the conservation of species in the solid phase follows

$$\frac{\partial c}{\partial t} = \frac{D_\mathrm{s}}{r^2}\frac{\partial}{\partial r}\left(r^2\frac{\partial c}{\partial r}\right). \tag{4.2}$$

Here c is Li concentration in the solid and D_s is the solid state diffusion coefficient and the boundary conditions are no-flux at the centre of the particle

$$\left.\frac{\partial c}{\partial r}\right|_{t,0} = 0, \tag{4.3}$$

and is coupled with a macroscopic problem through boundary conditions

$$D_\mathrm{s}\left.\frac{\partial c}{\partial r}\right|_{t,r_0} = \frac{i}{F}. \tag{4.4}$$

An important simplification is made in this model, namely, solid diffusion time is assumed to be the same on both electrodes, since there is no reference electrode measurement. The conservation of charge in the solid phase follows

$$\nabla \cdot \overrightarrow{i_\mathrm{s}} = -a_\mathrm{v} i, \tag{4.5}$$

$$\overrightarrow{i_\mathrm{s}} = -\sigma \nabla \phi_\mathrm{s}, \tag{4.6}$$

where i_s is the exchange current density, and the subscript 's' refers to the solid phase; a_v is the surface-area-to-volume ratio, i is the reaction current density, σ is the solid phase conductivity and ϕ_s is the electrical potential in the solid phase. Electrolyte charge balance is conventionally expressed with

$$\overrightarrow{i_\mathrm{l}} = -\kappa \nabla \phi_\mathrm{l} + \frac{2\kappa RT}{F}\left(1 + \frac{\partial \ln f}{\partial \ln cl_0}\right)(1 - t_+)\,\nabla \ln c_\mathrm{l} \tag{4.7}$$

where $\left(1+\frac{\partial \ln f}{\partial \ln cl_0}\right)$ denotes the thermodynamic factor, but with $\nabla c_l = 0$, the above equation simplifies to

$$\overrightarrow{i_{\mathrm{l}}} = -\kappa \nabla \phi_{\mathrm{l}}. \tag{4.8}$$

At each point in the electrolyte, the molar flux is related to the current in the electrolyte

$$\boldsymbol{\nabla} \cdot \overrightarrow{i_{\mathrm{l}}} = a_{\mathrm{v}} i. \tag{4.9}$$

Kinetics is usually expressed with the exponential Butler-Volmer relation Eq. (3.7), but in this model, the linearised Butler-Volmer equation is used to calculate the electrochemical (de)intercalation rate at solid/solution interface i. Nonlinear Burlter-Volmer equation was tried in place of 4.10 but similarly to Chu et al. [37], it was found to have negligible effect on the simulation results.

$$i = \frac{i_0 F \eta}{RT} \tag{4.10}$$

The reaction rate is assumed to be the same on both electrodes. The overpotential η that drives the charge transfer is calculated from

$$\eta = \phi_{\mathrm{s}} - \phi_{\mathrm{l}} - E_{\mathrm{OCP}}, \tag{4.11}$$

where E_{OCP} marks the open circuit potential. Instead of using half-cell OCP curves, the model describes the terminal voltage with a single OCP curve for a full cell. The terminal voltage E is defined as

$$E = E_{\mathrm{OCP}} + \eta_{+} - \eta_{-}, \tag{4.12}$$

where overpotential subscripts '+,-' refer to the anode and cathode. During the square-wave excitation simulations used for parameter estimation, the OCP (E_{OCP})

satisfies

$$E_{\mathrm{OCP}} = E_{\mathrm{OCP}}(q) + k_{\mathrm{u}}(q - q_0) + \frac{\Delta S}{F}(T - T_{\mathrm{ref}}) + V_{\mathrm{hys}} \cdot \mathrm{sgn}(I), \tag{4.13}$$

where, k_{u} is the OCP gradient with respect to fractional SOC at q_0, where q_0 is the average fractional state of charge of the whole pouch cell. ΔS is entropy change, V_{hys} is OCP hysteresis at q_0, which is measured experimentally between OCP charge and discharge curves ,and q is effective SOC at the particle surface. During constant current discharge and charge simulations, used for validation, the linearised OCP curve in Eq. (4.13) was substituted with full-cell experimental pseudo-OCP discharge data in the nonlinear form

$$E_{\mathrm{OCP}} = E_{\mathrm{OCP}}(q, T) + \frac{\Delta S(q)}{F}(T - T_{\mathrm{ref}}). \tag{4.14}$$

Here, the conventional cathode OCP was substituted with full-cell pseudo-OCP, while the anode OCP was set to ground (0 V). E_{OCP} and ΔS come from experiments measured separately for charge and discharge, therefore hysteresis term V_{hys} is not used in Eq. (4.14). Initial Li concentrations, active material volume fractions, average particle radii and other assumed properties are summarised in Table 4.1.

Two model parameters, κ and i_0, were assumed to exhibit temperature dependency. The ionic conductivity was assumed to change linearly with temperature,

$$\kappa(T) = \kappa_{\mathrm{ref}} + \alpha_{\kappa}(T - T_{\mathrm{ref}}), \tag{4.15}$$

while the exchange current density was assumed to change exponentially with temperature following an Arrhenius relationship [37],

$$i_0(T) = i_{0,\mathrm{ref}} \exp\left[\frac{-E_{\mathrm{i0}}}{R}\left(\frac{1}{T} - \frac{1}{T_{\mathrm{ref}}}\right)\right]. \tag{4.16}$$

The activation energy for the exchange current density is E_{i0}, and κ_{ref} and $i_{0,\mathrm{ref}}$ are the ionic conductivity and exchange current density at ambient temperature, respectively. Temperature coupling was performed through the local energy balance

$$\tilde{C}_{\mathrm{p}}\frac{\partial T}{\partial t} = \nabla\cdot(k\nabla T) + \sigma\nabla\phi_{\mathrm{s}}\cdot\nabla\phi_{\mathrm{s}} + \kappa\nabla\phi_{\mathrm{l}}\cdot\nabla\phi_{\mathrm{l}} + ai\eta + aiT\Delta S. \tag{4.17}$$

Here $\tilde{C}_{\mathrm{p}}$ is the effective local volumetric heat capacity, k is the effective thermal conductivity, σ is the solid phase conductivity and ϕ_{s} is the electrical potential in the solid phase. κ is the effective ionic conductivity of the liquid, and ϕ_{l} is electrical potential in liquid. a is the pore surface area per unit electrode volume, i is the current density across the pore surface, T is the measured temperature and ΔS is the reaction entropy of the electrode.

The boundary conditions on the cell surface follow Newton's law of cooling [20]

$$-\left(\overrightarrow{n}\cdot k\nabla T\right)|_{t,\mathrm{pouch}} = h(T|_{t,\mathrm{pouch}} - T_{\mathrm{ref}}), \tag{4.18}$$

where h is the heat transfer coefficient and T_{ref} is the ambient temperature.

The model was implemented in COMSOL, following the layer homogenisation approach proposed by Chu et al. [37], in which N cell layers are homogenised into one representative layer in a resultant pseudo-3D space. To account for the number of layers through the thickness of the cell, the following scaling was applied to the solid phase conductivity and liquid ionic conductivity parameters:

$$\sigma_{\mathrm{N}} = \sigma_1 N^2, \quad \sigma_{\mathrm{cc,N}} = \sigma_{1,\mathrm{cc}} N^2, \quad \kappa_{\mathrm{N}} = \kappa_1 N^2, \quad \kappa_{\mathrm{sep,N}} = \kappa_{1,\mathrm{sep}} N^2, \tag{4.19}$$

Chu et al. [37] explain that in order to create material characteristics invariant between one-layer and N-layer cells, the respective parameters in the one-layer cell need to be multiplied by a factor of N^2. More details on the derivation of Eq. (4.19)

Table 4.1: Summary of A123 Systems LFP/Gr cell parameter estimates at 50% SOC; Ψ_+ and Ψ_- are positive and negative electrode parameters respectively.

Parameter	Description	Ψ_+	Ψ_-	Method
L	Coating thickness (μm)	31.8	17.3	Measured (per side)
$c^{\max}$	Maximum concentration of Li in solid material (mol/m^3)	14500	26612	Assumed
R_p	Particle radius (µm)	5		From Lin et al. [20]
σ	Solid-phase conductivity (S/m)	50		From Lin et al. [20]
ε_s	Active material volume fraction (−)	0.5		From Lin et al. [20]
C_p	Solid phase heat capacity (W/m/K)	2000		From Chu et al. [37]
t_+	Transference number (−)	0.363		From Lin et al. [20]
c_l^0	Initial electrolyte concentration (mol/l)	1.2		From Lin et al. [20]

can be found in [37]. The A123 Systems 8 Ah cell tear-down revealed that the number of cell layers in our study was $N = 52$. It is important to note that if $D_\mathrm{l} \to \infty$, scaling of D_l is not necessary. However, if a finite value of D_l was assumed, to satisfy the non-dimensional limiting current defined in Eq. (4.1), D_l should also scale by N.

4.3.2 Parameter estimation

The battery model parameters listed in Eq. (4.20) were identified through an optimisation routine implemented in MATLAB with forward simulations in COMSOL via MATLAB's LiveLink connection.

$$\theta = \begin{bmatrix} ai_0 & Ei_0 & \kappa_\mathrm{ref} & \alpha_\kappa & k_\mathrm{U} & \tau_\mathrm{D} & \Delta S & \frac{h}{Cp} & k \end{bmatrix}^\mathrm{T}. \tag{4.20}$$

Here τ_D is the diffusion time ($\tau_\mathrm{D} = \frac{R_\mathrm{p}^2}{D_\mathrm{s}}$), and $\frac{h}{Cp}$ is the heat transfer velocity. Parameters were identified by minimising both the battery surface temperature and output voltage errors between the model and data using maximum likelihood estimation (MLE), which is a statistical method used to estimate the parameters of a probability distribution, given a set of observed data [175]. The procedure detailing parameter optimisation is attached in Appendix C.

The computer used for forward simulations was a high-performance LENOVO ThinkPad X1 Extreme Gen 5, 12th Gen Intel Core i7, 2400 MHz with 14 cores. The speed of a single forward evaluation was ≈ 9.8 min. To shorten the computation time, dynamic mode decomposition (DMD), a data-driven method, was used to simulate only a portion of the necessary timespan and extrapolate the remaining data.

4.3.2.1 Dynamic mode decomposition (DMD)

The DMD is a technique used to reduce the dimensionality of a system. It achieves this by identifying a set of dominant modes, each of which corresponds to a fixed oscillation frequency and growth/decay rate. When applied to linear systems, these modes and frequencies can be used to estimate the modes and eigenvalues of the composition operator (also known as the Koopman operator) [176]. Following the approach proposed by Kanbur et al. [177], the data takes the form of a snapshot matrix X_1^N

$$X_1^N = \begin{bmatrix} | & | & & | \\ x_1 & x_2 & \cdots & x_N \\ | & | & & | \end{bmatrix} \tag{4.21}$$

where $x_i \in \mathbb{R}$ is the i-th snapshot of the field, and $X_1^N \in \mathbb{R}^{MxN}$. The system states are pixels outputted from the IR camera image (75 x 91), taken at a fixed time step of 1 s. A matrix is formed by rearranging the pixels into a column vector $M = 6825$. These snapshots are assumed to be related via a linear mapping (A) that defines a linear dynamical system, $x_{i+1} = Ax_i$. The output of the DMD process is the eigenvalues

and eigenvectors of A.

$$\underbrace{\begin{bmatrix} | & | & & | \\ x_2 & x_3 & \cdots & x_N \\ | & | & & | \end{bmatrix}}_{X_2^N} = A \underbrace{\begin{bmatrix} | & | & & | \\ x_1 & x_2 & \cdots & x_{N-1} \\ | & | & & | \end{bmatrix}}_{X_1^{N-1}} \tag{4.22}$$

Here we used $N_{\text{pred}} = 2500$ to guess until the 2500 s. More information about the DMD method can be found in Appendix D.

4.4 Simulation I: Results and discussion

4.4.1 Parameter estimates from square wave excitation

The results of the 4C and 8C square wave measurements and simulations with optimal parameters are plotted in Fig. 4.4. It is observed that both voltage and average surface temperature profiles fit well throughout the 4C and 8C pulses. Voltage and surface temperature RMS errors for the 4C simulation were 5.3 mV and 0.08 °C respectively. At 8C, the RMS errors increased to 9.96 mV and 0.18 °C, which is still perceived as a good accuracy at such a high current. The parameters found through the optimisation process are summarised in Table 4.2. The previous results from Lin et al. [20] and Chu et al. [37] are included for comparison purposes.

All optimal parameter estimates were expected to remain similar across C-rates. However, a substantial difference was noted as a function of C-rate for the volumetric exchange current density and electrolyte ionic conductivity values. Both of these parameters contribute to the ohmic drop, which results in heat generation. The ai_0 increased with a higher C-rate, while κ decreased with a higher C-rate, which may indicate an identifiability problem. This will be discussed in the next section. The remaining parameters remained relatively stable across the C-rates. The k_{U} parameter

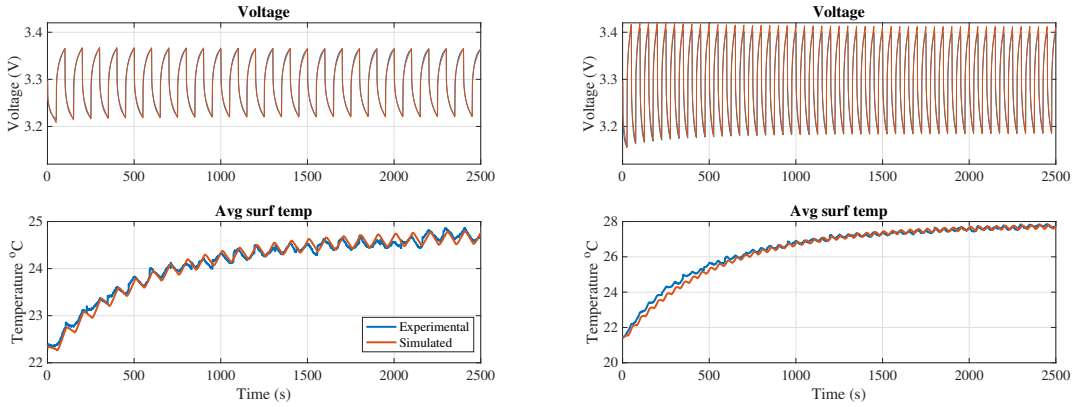

(a) (b)

Figure 4.4: Simulation results showing voltage and average surface temperature for (a) 4C and (b) 8C over 2500 s, square wave pulses.

returned an average value of 0.205 V, which was consistent with Lin et al. and Chu et al. [20, 37], however, the value is substantially higher than the expected physically meaningful value for this parameter. Based on Chu et al., the OCP linearisation, k_{U}, is supposed to represent the OCP slope [37], however at 50 % SOC, the experimental OCP slope for an LFP cell is ∼0.03 V. This may point towards potential problems with linearisation, where not all physical phenomena are accounted for, which in turn may affect the estimated values of other parameters.

The thermal parameters such as k, $\frac{h}{Cp}$, α_κ and Ei_0 take comparatively similar values to the study by Lin et al. [20]. However, entropy change values were considerably higher than found in previous studies (7.7 J/mol/K) [20], and higher than in other literature on LFP/Gr cell ΔS ≈20 J/K/mol [73, 178]. The unrealistically high value of ΔS could indicate that the assumed value for solid phase heat capacity was too high.

A further difference was noted in estimated diffusion time, which was ∼ 5 times longer than in Lin et al. [20]. This finding was unexpected, given that the cell in this study had the same surface area, but substantially thinner electrodes than in Lin et al., therefore diffusion time was expected to be shorter. The effect of diffusion

Table 4.2: Output parameters from 4C100 s and 8C 50 s square wave optimisation at 50 % SOC. The last two columns include results presented by Chu et al. [37] (streamlined model) and Lin et al. [20] (the same model as used in this study), 20 Ah A123 Systems LFP pouch cell at the same conditions, namely 50 % SOC 4C100 s pulse.

Parameter	Description	4C pulse	8C pulse	Avg	Chu et al. [37]	Lin et al. [20]
ai_0	Volumetric exchange current density (A/cm^3)	1.35	2.54	1.92	120	1.8
Ei_0	Activation energy of i_0 (kJ/mol)	37.2	38	37.6	30.6	29.2
κ	Electrolyte ionic conductivity (S/m)	0.025	0.015	0.02	0.019	0.043
α_κ	Temperature coefficient of κ (mS/m/K)	3.5	1.5	2.5	2.0	2.7
k_U	Open circuit potential gradient (V)	0.19	0.22	0.205	0.22	0.24
τ_D	Diffusion time $\frac{R_\mathrm{p}^2}{D_\mathrm{s}}$ (s)	2477	2634	2555	-	590
ΔS	Entropy change (J/mol/K)	32	30.4	31.2	7.7	7.7
v	Heat transfer velocity $\frac{h}{Cp}$ (µm/s)	5.3	5.3	5.3	5.2	5.06
k	Effective thermal conductivity (W/m/K)	1.05	1.1	1.075	72	1.2

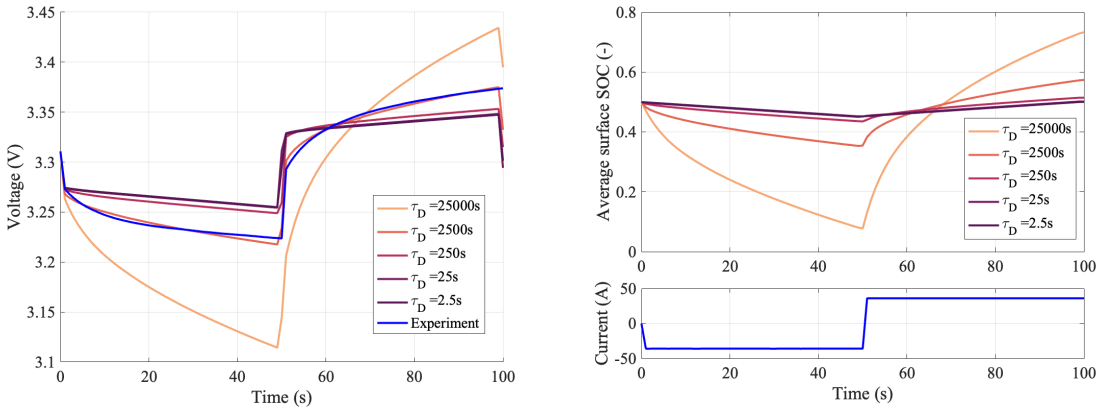

(a) (b)

Figure 4.5: Visualisation of the impact of change in diffusion time on (a) simulated voltage and (b) simulated average surface SOC.

time on the linearised model is shown in Fig. 4.5. It can be seen that the shorter the diffusion time, the 'flatter' the pulse voltage response. Slower diffusion times result in a rounder, larger voltage profile. Judging solely on the voltage profile in Fig. 4.5(a), the diffusion time of ∼2500 s provides the best fit to experiment. However, when comparing against the simulated average SOC of an electrode (in this case plotted for the anode) in Fig. 4.5(b), an important phenomenon becomes visible. For slower diffusion times, average surface SOC falls significantly below 5 % of its nominal value (0.5). The ratio of surface concentration (c^s) to average concentration (c^avg) becomes

a parameter that can help identify whether there are solid diffusion limitations.

$$c_{\text{lim}} = \frac{c^{\text{s}}}{c^{\text{avg}}} \tag{4.23}$$

From Fig. 4.5(b) with a value of $\tau_{\text{D}} = 2500\,\text{s}$ found by the optimiser, a significant solid diffusion limitation is observed, which was not expected for a power cell at 4C. This is likely caused by a failure of parameter identifiability or an overspecified model. The average surface SOC profile illustrated in Fig. 4.5(b) suggests that a very fast diffusion time is required for the solid diffusion limitation not to occur i.e. $<250\,\text{s}$. However, this in turn drives the voltage profile to be flatter and increases the voltage error, which adversely affects the optimiser objective. It seems therefore, that for the linearised model used and the power cell used, the inclusion of τ_{D} as a parameter to be estimated may lead to an inability to identify τ_{D}, and may have biased the results of estimating ai_0 and κ. However, it seems that the instantaneous voltage drop is matched well by the optimised ai_0 and κ parameters and is not affected by a change in τ_{D} parameter.

4.4.2 Validation with 2C-10C CC full charge/discharge

To investigate further the impact of $\tau_{\text{D}} = 2500\,\text{s}$, the same set of parameters (i.e., the average parameters from Table 4.2) was used to investigate the model performance during constant current charge and discharge, ranging from 2C to 10C. The results of these simulations are shown in Fig. 4.6, and it is visible that all simulations terminated prematurely. This shows that, under constant current full charge or discharge, the long diffusion time is unrealistic.

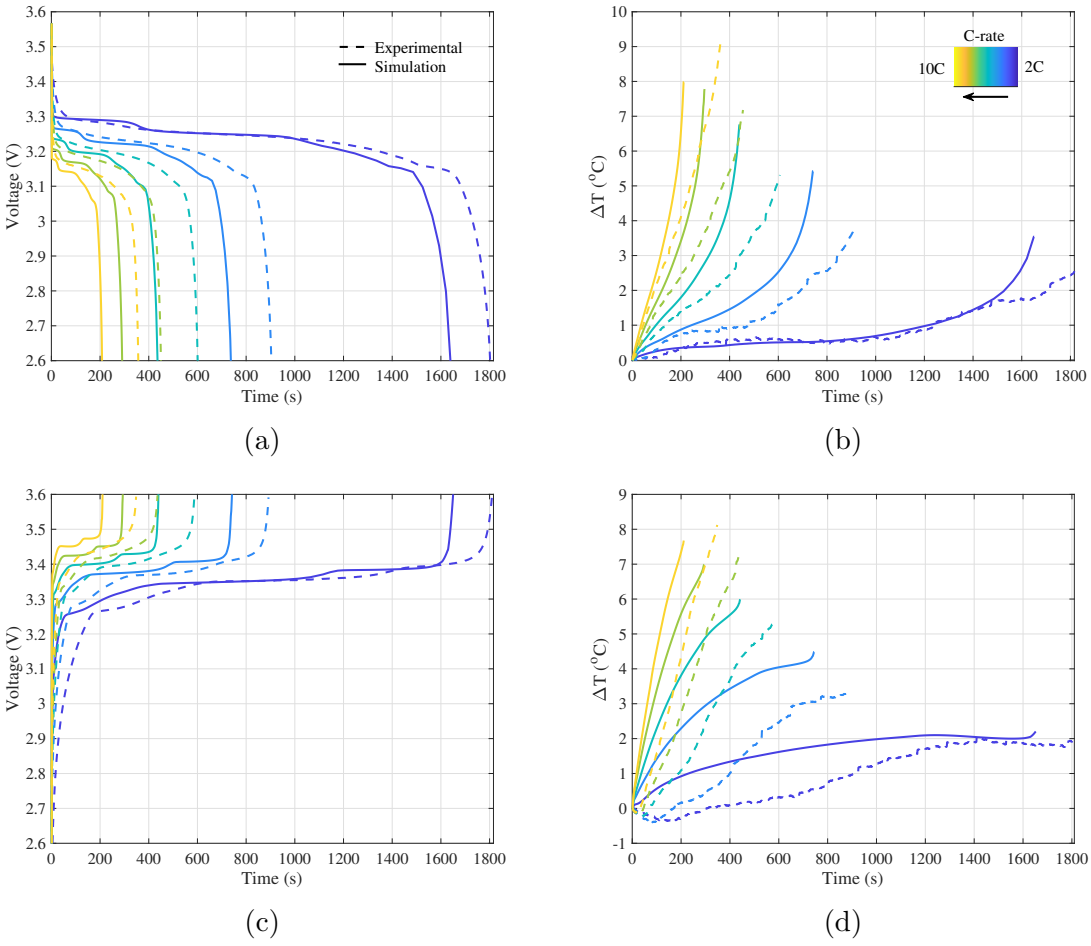

Figure 4.6: Simulation results across 2C-10C constant current discharge (a)-(b) and charge (c)-(d), with the assumption of τ_{D} 2500 s.

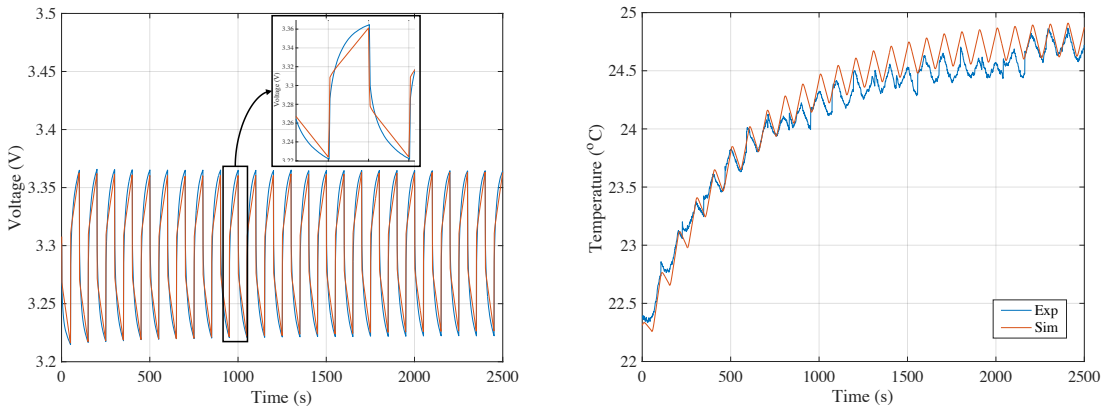

(a) (b)

Figure 4.7: Comparison between simulation and experimental results showing (a) voltage and (b) average surface temperature for 4C square wave pulse over 2500 s.

Table 4.3: Fitted parameters from the previous 4C pulse simulation including diffusion ('Sim I 4C pulse'), and the 4C pulse simulation when $D_s \to \infty$ ('Sim II 4C pulse'). The last two columns include comparison results by Chu et al. [37] (streamlined model) and Lin et al. [20].

Parameter	Description	Sim I 4C pulse	Sim II 4C pulse	Chu et al. [37]	Lin et al. [20]
ai_0	Volumetric exchange current density (A/cm^3)	1.35	1.12	120	1.8
Ei_0	Activation energy of i_0 (kJ/mol)	37.2	30.89	30.6	29.2
κ	Electrolyte ionic conductivity (S/m)	0.025	0.021	0.019	0.043
α_κ	Temperature coefficient of κ (mS/m/K)	3.5	2.5	2.0	2.7
k_U	Open circuit potential gradient (V)	0.19	0.55	0.22	0.48
τ_D	Diffusion time $\frac{R_p^2}{D_s}$ (s)	2477	-	-	590
ΔS	Entropy change (J/mol/K)	32	33.14	7.7	7.7
v	Heat transfer velocity $\frac{h}{Cp}$ (µm/s)	5.3	5.3	5.2	5.06
k	Effective thermal conductivity (W/m/K)	1.05	1.21	72	1.2

4.5 Simulation II: Results and discussion

4.5.1 Parameter estimates from square wave excitation

Given the unrealistically long solid diffusion time found in the above Section 4.4, it does not make sense to try to fit the diffusion time parameter for this cell and this dataset, so we now explore setting $D_s \to \infty$ in order to assume fast diffusion, and then refitting the other model parameters. The resultant voltage and average surface temperature fits from this process are shown in Fig. 4.7, with corresponding optimal parameter values summarised in Table 4.3.

Fig. 4.7(a) shows the voltage response to a 4C100 s square wave pulse at 50% SOC. With solid diffusion dynamics removed (i.e., assumed fast), although general trends and the outer envelope are correct, the 'curvature' of the voltage response cannot be fitted particularly accurately and the RMSE on voltage has increased to 19.4 mV. The parameter k_{U} compensates partially for this effect by taking a higher value ($k_{\mathrm{U}} = 0.48$), and the voltage response takes a more triangular shape. As already mentioned in Section 4.4, k_{U} takes an unrealistically high value for the local OCP slope that it is theoretically supposed to represent ($\sim$0.03 V for LFP cells). The fact that slow diffusion gave a better fit to the voltage response during local square wave cycling (in the previous section), but also caused poor performance during full CC charge-discharge, suggests that either there is a parameter idenfiability issue and/or the model is making some incorrect assumptions about the underlying thermal-electrochemical behaviour.

In the absence of diffusion overpotential, both κ and ai_0 took slightly smaller values (Table 4.3). As a result, the average surface temperature RMSE increased slightly from 0.08 °C to 0.13 °C. The remaining parameters in Table 4.3 are similar to the previous simulation.

4.5.2 Validation with 2C-10C CC full charge/discharge

To verify whether the $D_{\mathrm{s}} \to \infty$ assumption is correct, the new parameters of Table 4.3 were used for 2C-10C CC full charge and discharge simulations and compared to independent measurements. The results are illustrated in Fig. 4.8, where the top row corresponds to discharge, and the bottom row corresponds to charge. With both solid and electrolyte diffusion limitations removed, the cell reaches cut-off voltage when the average SOC reaches 0 %. While the lower C-rate simulations are matched well to measurements, for both voltage and average surface temperature, as the C-rate increases, the simulated data begins to deviate from the experimental results,

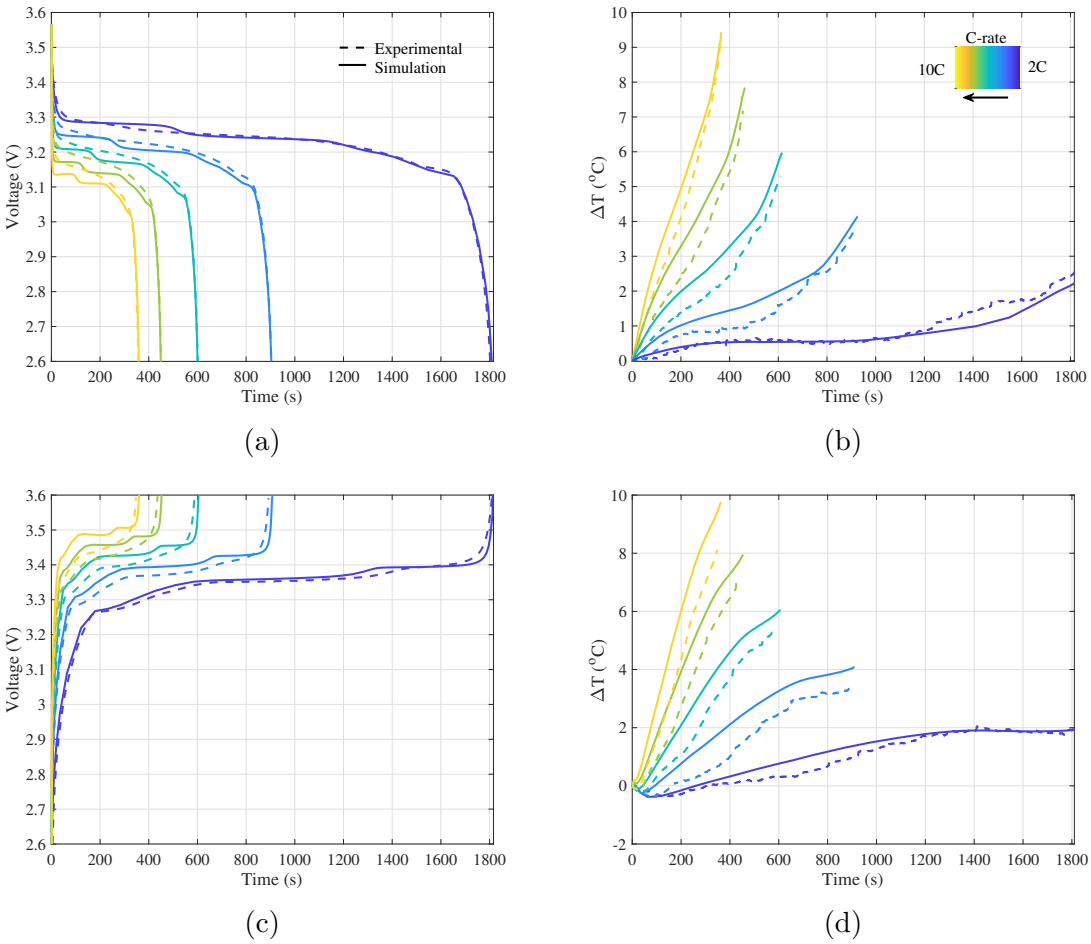

Figure 4.8: Simulation and experimental results across 2C-10C constant current discharge (a)-(b) and charge (c)-(d), with the assumption of $\tau_D \rightarrow \infty$ and all other parameters constant as fitted in Table 4.3.

particularly during charging. Specifically, during charging the simulated voltage is overestimated, which leads to excessive thermal prediction. Additionally, for charge, the simulation slightly overrun the experimental time (the cut-off voltage limit was reached several seconds after the actual experiment was completed). Although a very small effect, this might indicate that for charge, a limiting condition was reached that was not present during discharge, or that there was some small error in parameter(s).

Given that cell internal resistance has been shown to vary with SOC [179], for improved accuracy, the ai_0 parameter can be adjusted for the beginning of CC charge

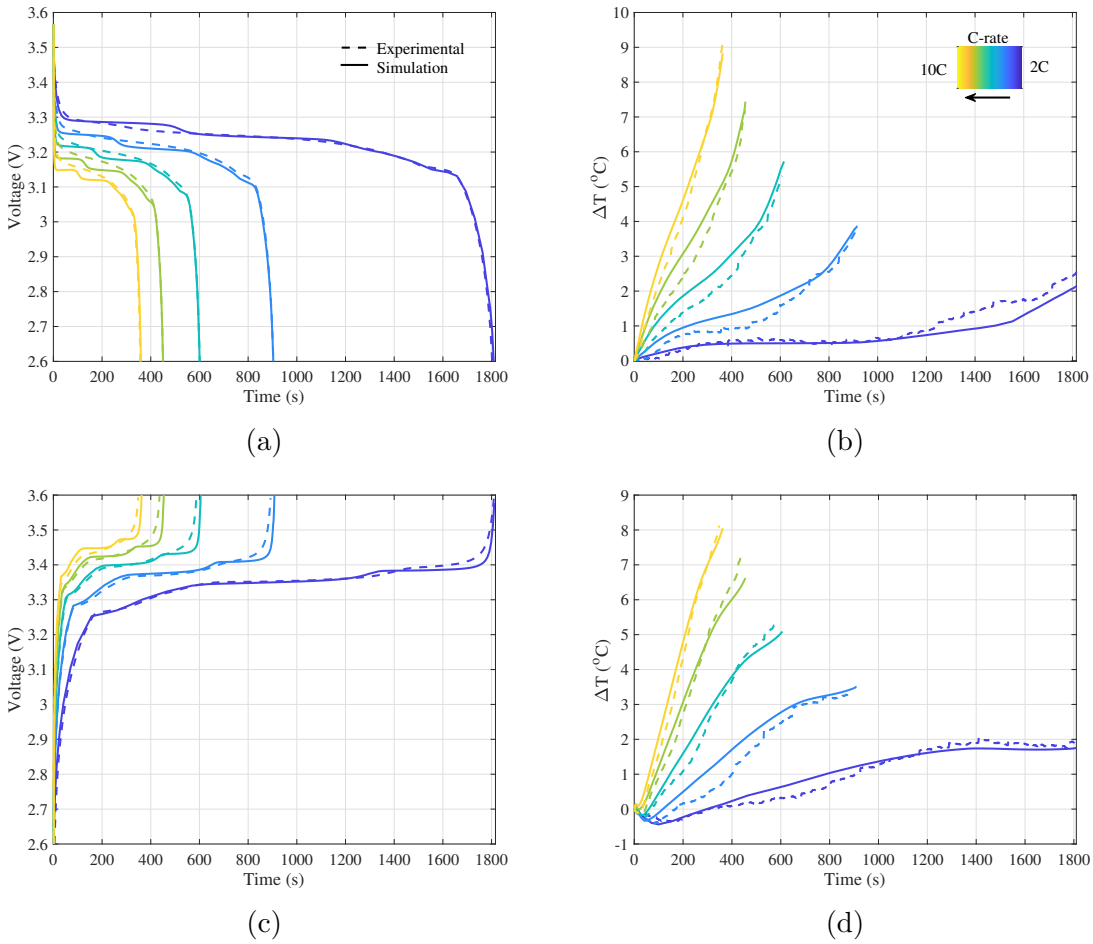

Figure 4.9: Simulation and experimental results across 2C-10C constant current discharge (a)-(b) and charge (c)-(d), with the assumption of $\tau_D \to \infty$. $ai_0 = 1.12\,\mathrm{A/cm^3}$ at 100 % SOC and $ai_0 = 1.95\,\mathrm{A/cm^3}$ at 0 % SOC.

(0 % SOC) and beginning of CC discharge (100 % SOC), giving the improved comparative results shown in Fig. 4.9. The optimal value of ai_0 is found by following the same optimisation routine as in Section 4.3.2, however this time, the only adjustable parameter is ai_0 and it is constrained to be the same for all 2C-10C CC datasets so that a single value of ai_0 is found for all datasets. This procedure is performed separately for charge and discharge, and the optimal values found are $ai_0 = 1.12\,\mathrm{A/cm^3}$ at 100 % SOC and $ai_0 = 1.95\,\mathrm{A/cm^3}$ at 0 % SOC. Here, Fig. 4.9(a) and (c) show voltage profiles across these new 2C-10C simulations, with a higher level of accuracy between model and data compared with Fig. 4.8, even at 10C. Similarly, in Fig. 4.9(b) and

(d) the average surface temperature simulation results reveal a good resemblance to experiments. However, certain differences are still noted. Specifically, given the low internal resistance of the power cell used here, the entropic contributions to temperature become more apparent than in comparable energy cells. A characteristic cooling behaviour can be observed at the beginning of the charge, as well as in the middle proportion of discharge. In these regions, entropy change becomes positive (resulting in cell cooling). This cooling behaviour is only partially fitted by the model, which suggests that more accurate entropy data, over the full SOC range, may be needed.

Similarly to Lin et al. [20], no substantial errors in voltage or temperature response were observed due to the assumption of linearised kinetics. Given the low internal resistance cell used in this study, the resultant voltage drop due to reaction kinetics caused by the 8C pulse here was less than the voltage drop caused by a 4C pulse for the cell studied by Lin et al. [20].

Temperature gradients across the cell surface at the end of the CC charge using model with adjusted ai_0 are illustrated in Fig. 4.10. The readings from the IR camera are shown on the left hand side, and the model simulation results are on the right hand side. The contour plots reveal a certain discrepancy between experimental hot-spot shape and location compared with simulations. This could be due to assumed boundary conditions or due to the assumed effective heat capacity of the solid phase. The fact that average surface temperature was underestimated by the model is also reflected in Fig. 4.10. Here the maximum value of the simulated hot spot at 10C charge was 0.39 °C lower than the experimentally observed value. The largest absolute temperature error, however, is visible for the 8C case, where the error reaches almost 1 °C.

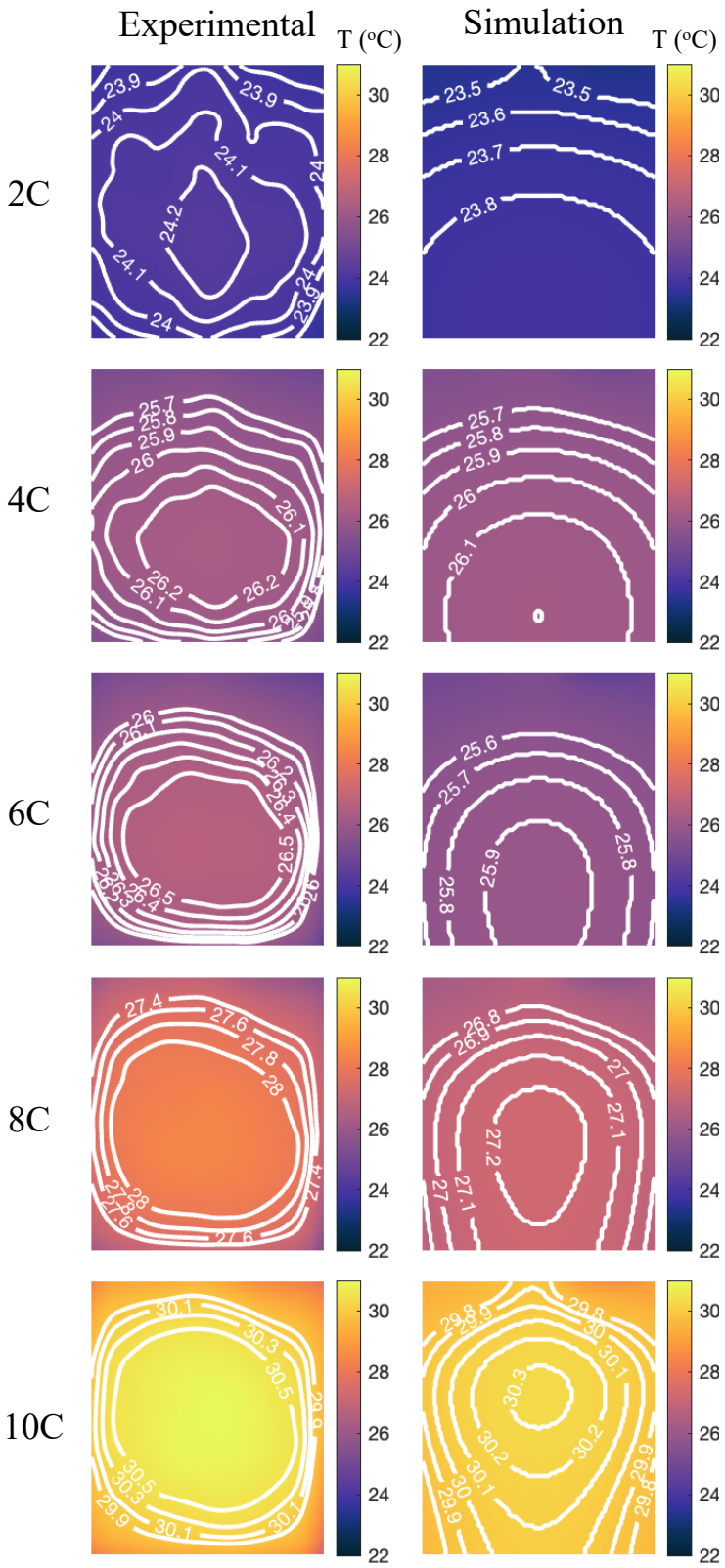

Figure 4.10: Surface temperature change at the end of CC charge, when $ai_0 = 1.95\,\mathrm{A/cm^3}$.

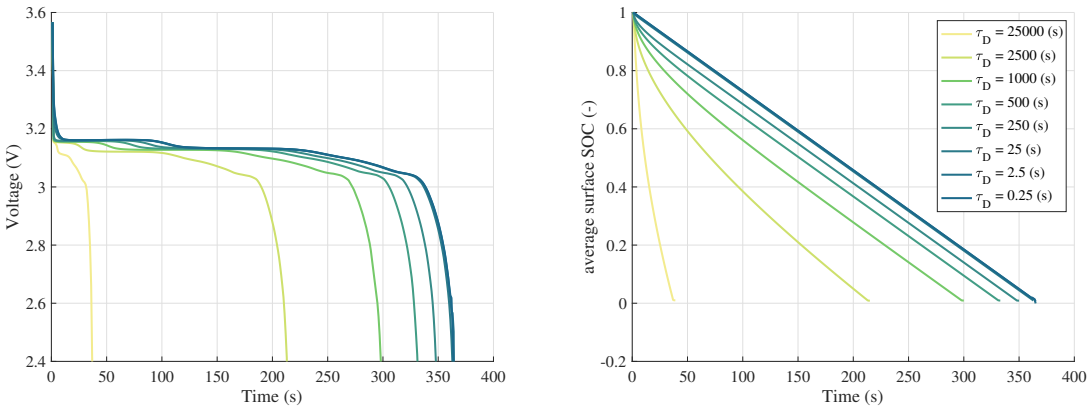

(a) (b)

Figure 4.11: Figure presents an impact of solid diffusion time ranging from 0.25 s to 25 000 s on (a) cell voltage and (b) average surface concentration during 10C discharge.

.

4.6 Solid and liquid diffusion limiting factors

The model here assumed fast electrolyte diffusion D_l, but for more energy-dense cells, this assumption could be limiting. Both solid and liquid diffusion times impact the accessibility of available energy in the cell. Whichever time is longer will limit cell performance, under-using cell electrodes. In a solid diffusion-limited process (already discussed in section 4.4.1) very slow diffusion times can lead to surface SOC reaching its limit sooner than average SOC (0% or 100 %) in the particles, which results in a sudden overpotential increase. The impact of diffusion time on simulated voltage and surface concentration is illustrated in Fig. 4.11. As can be seen, for the model considered here (using parameters Table 4.3), if $D_\mathrm{s} \leq 25\,\mathrm{s}$ then there is negligible diffusion overpotential, but with $D_\mathrm{s} > 25\,\mathrm{s}$ there is a much steeper decrease in surface SOC, leading to premature cut-off of discharge and possibly issues such as undissolved Li being deposited (plated) at the electrode surface during charging.

Similarly to solid diffusion time, electrolyte diffusion time can be calculated for each element in the cell as

$$\tau_{Dl_{\mathrm{a,c,s}}} = \frac{L^2_{\mathrm{a,c,s}}}{D_\mathrm{l}}, \tag{4.24}$$

where subscripts 'a,c,s' refer to the anode, cathode and separator respectively. Assuming similar porosities, this implies that the element with the largest thickness will experience the highest gradient of electrolyte concentration.

To study the impact of diffusion time on cell response, the same model as in Section 4.3.1 was used, this time with solid diffusion set to $\tau_{D_e} \to \infty$, and electrolyte diffusion coefficient varied from $5 \times 10^{-13}\,\mathrm{m^2/s}$ to $1 \times 10^{-7}\,\mathrm{m^2/s}$. The results are presented in Fig. 4.12, for both constant current and pulse cases. It can be seen that for $D_\mathrm{l} \geq 1 \times 10^{-9}\,\mathrm{m^2/s}$ the voltage response is almost unchanged, and there is no gradient in electrolyte concentration. A slower electrolyte diffusion time $D_\mathrm{l} = 1 \times 10^{-10}\,\mathrm{m^2/s}$, leads to a concentration gradient created across cell layers, which results in voltage drop, however, it does not lead to premature cell discharge. Once lower electrolyte diffusion coefficient values are considered ($D_\mathrm{l} < 1 \times 10^{-11}\,\mathrm{m^2/s}$), during a 10C discharge the electrolyte concentration reaches $0\,\mathrm{mol/m^3}$, which is a physical limit for cell operation (and would cause i_0 to drop if full Butler Volmer equation was used). Given that problem is solved in pseudo 3D, there is a possibility for local electrolyte depletion. The case presented is from a 1D line intersecting the middle of the cell (in the horizontal, y, and vertical, z, planes). The same values for D_l were compared with 4C100 s pulse at 50 % SOC voltage response data in Fig. 4.12 (b). It is visible that a decrease in electrolyte diffusion coefficient (i.e. increasing diffusion time) is associated with a gradual increase in overpotential. However, for a short duration of pulse, electrolyte concentration does not reach $0\,\mathrm{mol/m^3}$, and so the limiting condition is not reached. In the optimisation routine used in the previous section, both parameters κ and ai_0 were fitted to account for the voltage drop during the pulse. This means that if there was a voltage drop caused by electrolyte diffusion, it would not be possible to identify it, but it would have affected the output value of fitted parameters.

The two output measurements available from a cell, namely voltage and tem-

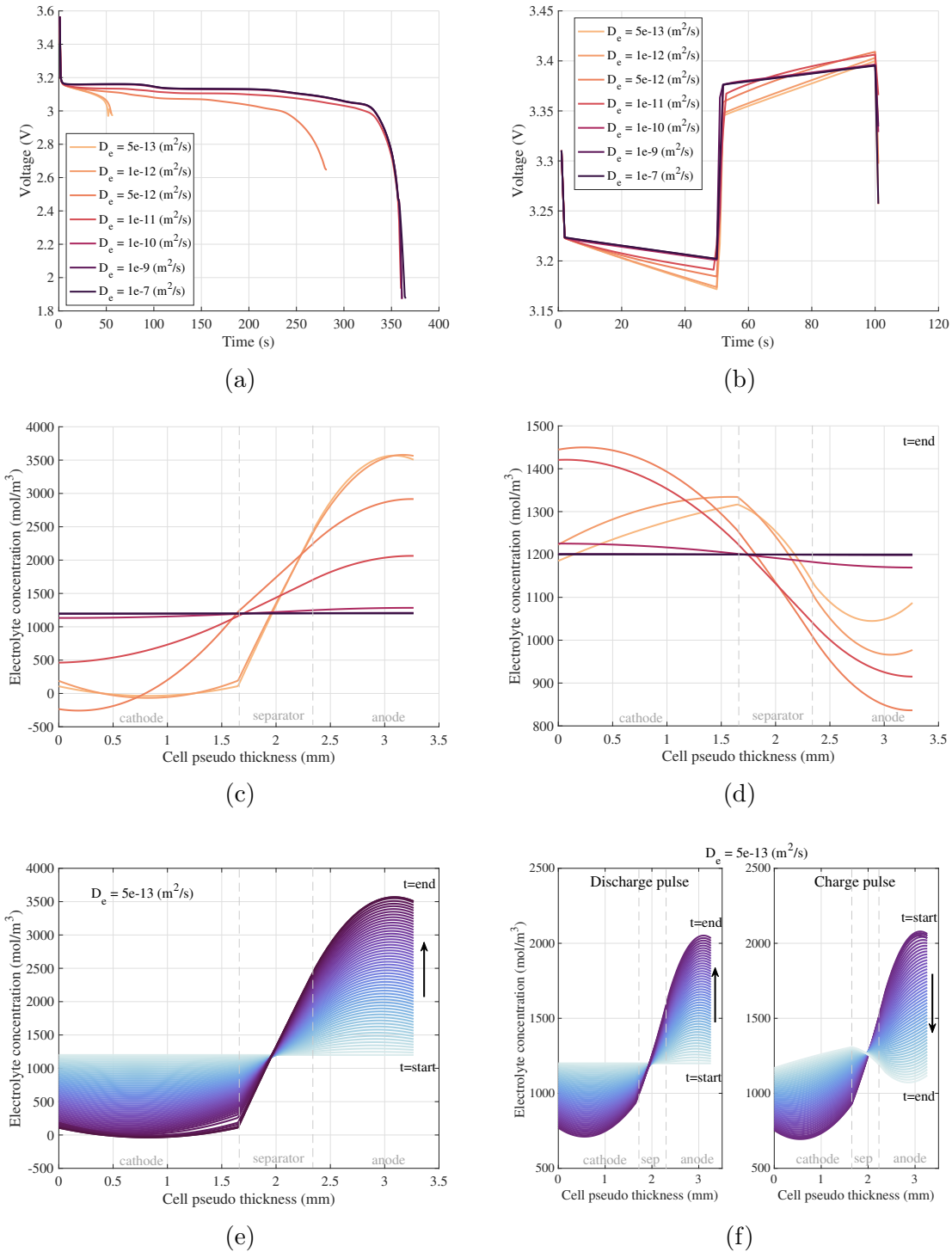

Figure 4.12: Electrolyte diffusion impact during 10C discharge (left column) and 4C100 s pulse at 50 % SOC (right column). Plots (a) and (b) show how variation of D_l influenced cell voltage, (c) and (d) electrolyte concentration at the last time step before simulation was terminated, (d) and (e) show electrolyte concentration variation in time for the specific case of the $D_l = 5 \times 10^{-13}\,\mathrm{m}^2/\mathrm{s}$.

perature, are not sufficient to distinguish between the electrolyte and solid diffusion limitations. Both result in increased overpotentials and subsequent premature end of (dis)charge. From a design standpoint, the two diffusion times (τ_{D_s} and τ_{D_l}) could be of similar magnitude in order to maximise electrodes' utilisation. A direct comparison is made here between the diffusion times of three different cells: the Samsung 35E energy cell introduced in Chapter 2, the A123 System high power cell used in this chapter, and an A123 Systems moderate performance cell used by Lin et al. [20]. A table detailing relevant parameters, i.e. individual element thicknesses as well as particle radii and effective diffusion times for the three discussed cells is summarised in Table 4.4. Given that the specific electrolyte was not known in all three cases, electrolyte diffusivity was assumed to be the same for all cells and taken as an average from the literature available in LiionDB at $1\,\mathrm{mol/m^3}$, namely $D_l = 4 \times 10^{-10}\,\mathrm{m^2/s}$ [180].

Table 4.4 highlights the differences in cell solid and liquid diffusion times across a pouch form factor power cell, energy cell and a cylindrical energy cell. For both the Samsung 35E cell and the 20 Ah A123 Systems cell, the electrolyte diffusion time is significantly faster than the solid diffusion time, therefore, the limitation comes from the solid material first. On the other hand, 8 Ah A123 Systems power cell illustrates an example of balanced solid and liquid diffusive times, where both τ_{D_l} and τ_{D_s} take similar value. Although there are other characteristic timescales that need to be considered when designing a cell (kinetic/intercalation reaction timescale [27, 42]), a comparison between the electrolyte and solid diffusion times could provide an indication of whether modelling of certain dynamics is necessary, or redundant.

4.7 Conclusions

This chapter analysed the response of a power cell to high C-rate cycling using a pseudo-3D continuum model in COMSOL, comparing measurements to simulations.

Table 4.4: Comparison of diffusion times for three cells: 8 Ah 123 Systems power dense pouch cell, 20 Ah 123 Systems energy dense pouch cell, and 3.4 Ah Samsung 35E energy dense cylindrical cell.

	8 Ah A123 Systems	20 Ah A123 Systems [20]	Samsung 35E
Anode thickness L_{anode} (µm)	17.3	40	83.3
Cathode thickness L_{cathode} (µm)	31.8	70	71.5
Anode particle radius $R_{\text{p,anode}}$ (µm)	5	5	1
Cathode particle radius $R_{\text{p,cathode}}$ (µm)	5	5	1.2
Anode diffusion coefficient $D_{\text{s, anode}}$ (m^2/s)	1.00E-11	5.00E-14	1.90E-16
Cathode diffusion coefficient $D_{\text{s, cathode}}$ (m^2/s)	1.00E-11	5.00E-14	1.90E-16
Electrolyte diffusion coefficient D_{l} (m^2/s)	4.00E-10		
Solid diffusion time $\tau_{D_{\text{s, anode}}} = \frac{R^2_{\text{p,anode}}}{D_{\text{s,anode}}}$ (s)	2.5	500	7578.9
Solid diffusion time $\tau_{D_{\text{s, cathode}}} = \frac{R^2_{\text{p,cathode}}}{D_{\text{s,cathode}}}$ (s)	2.5	500	5263.2
Electrolyte diffusion time $\tau_{D_{\text{l, anode}}} = \frac{L^2_{\text{anode}}}{D_{\text{l}}}$ (s)	0.8	4	17.3
Electrolyte diffusion time $\tau_{D_{\text{l, cathode}}} = \frac{L^2_{\text{cathode}}}{D_{\text{l}}}$ (s)	2.5	12.3	12.8

During the optimisation procedure several interesting challenges were identified.

The optimisation of parameters from pulse data returned diffusion times higher than physically possible to simulate the 10C CC full charge/discharge scenario, despite giving an accurate fit to the square charge/discharge data. This may suggest a limitation in the model assumptions or parametrisation procedure. Additionally, the OCP slope parameter k_{U} was found to be unrealistically high (though consistent with work of [20, 37]), which may suggest that certain unmodelled effects, such as voltage hysteresis or heterogeneities that break the modelling assumptions, are important.

Notwithstanding these limitations, the parameter optimisation routine yielded credible results for the thermal parameters and was able to fit accurately the instantaneous voltage drop following a current pulse. In the initial parameter estimation, the contribution of heat from the diffusion overpotential was relatively low compared to the total heat generated. This, combined with the very fast diffusion times needed to satisfy the CC validation data, led to a hypothesis that the diffusion time could be considered infinite/very fast for the studied power cell tested under the given conditions. This assumption was further tested by re-parameterising the model and checking again with CC full charge/discharge data ranging from 2C to 10C, and it was found that simulations of both voltages and surface temperatures were well-matched, with an average surface error of approximately 0.5 °C and a maximum of 1 °C.

In conclusion, a continuum thermally coupled electrochemical model with linearised kinetics and infinitely fast diffusion for both electrolyte and solid provided good accuracy for the power cell studied here, providing the most accurate thermal predictions to date at 10C and plausible estimates of model parameters from data. However, the model's accuracy could be further improved for example by considering the impact of heterogeneity across layers, or of voltage hysteresis. This means that more research and validation across multiple datasets is required to extend this work. An additional challenge in electrochemical and thermal modelling may arise when

dealing with solid or electrolyte-limited processes.

4.8 Limitations and Further work

4.8.1 Limitations

The first limitation of this study arises from the parametrisation procedure used. While the optimisation routine aimed to remove the need for more resource-and time-consuming experimental cell characterisation procedures, the presence of numerous optimisation parameters might lead to correlations among some, making their unique identification challenging. Additionally, the parameter representing the OCP slope was found to have a physically unrealistic value, which may suggest a limitation in the linearisation and homogenisation process and/or unmodelled physics present. While significant model reduction was achieved through the assumption of infinitely fast electrolyte diffusion, this assumption may not be applicable to cells with thicker electrodes—it must be remembered that the cell studied here has already been designed for high power usage. If electrolyte diffusion limitations were experienced by the cell, this effect would not have been recognised by the model (since electrolyte was not modelled), and the resultant voltage drop would instead be attributed to κ or ai_0 or another parameter. While the model reduces the number of parameters by assuming full-cell OCP instead of individual electrode half-cell OCPs, and by assigning a single kinetic rate and diffusion time for both electrodes, these simplifications mean that no information about single electrode performance (and limitation) can be drawn from the model—however, this is a fundamental limit without a reference electrode.

4.8.2 Further Work

To address these challenges, it would be beneficial to experimentally characterise the cell with a more invasive procedure, and compare parameter values obtained to those obtained here. Reducing the number of parameters to be fitted could also improve identifiability and solution time. Parameter sensitivity analysis should be performed to verify if all the parameters can be uniquely identified.

The observed disparity between the pulse voltage curvature, which requires a physical effect such as slow solid diffusion, and the full charge/discharge CC data, which requires fast diffusion, suggests the presence of unmodelled physics or limitations within the current model and its assumptions. Thus, investigating this phenomenon further is critical to gain a more comprehensive understanding of the underlying physical mechanisms at play. This work did not focus on the influence on the voltage response of the charge/discharge pulse duration during squarewave excitations, however, this should also be addressed, as well as considering a wider range of SOC points. A more comprehensive study is also required to address the poor identifiability of parameters at lower C-rates, where temperature rise is small.

Additional work could consider the optimal definition of cost functions used in parameter optimisation. In this work, a pixel-to-pixel comparison of temperature data was used for surface temperature. However, in Lin et al. [20] a temperature spatial concavity metric was proposed, where a correlation was made between concavity in one direction across the cell, and solid diffusion time value. While the evolution of the hotspot shape can be explained by the diffusion limitation causing increased heating, in this work, the shape of the hotspot was not affected by the solid diffusion time. This raises the question of whether concavity or a similar metric is necessary for diffusion parametrisation or if the shape and evolution of the hotspot are dictated by the boundary conditions and assumed heat capacity value.

Chapter 5

Conclusions

The aim of this thesis was to contribute to the development of advanced battery management systems for electric vehicles through improved degradation diagnosis/prognosis and cell modelling. Three pressing challenges in the EV world were identified and discussed in individual chapters:

- accurate diagnosis of battery ageing,
- effective inclusion of predicted degradation within the battery model,
- accurate prediction of internal battery internal states at high current rates (fast charge).

5.1 Contributions

5.1.1 Accurate diagnosis of battery ageing

Entropy profiling was proposed as an alternative method for degradation diagnosis. So far this method has not been quantitatively studied or compared to available state-of-the-art methods such as DVA/ICA, and work in this chapter has filled this gap.

For this investigation, NCA/Gr-Si cells were used and subjected to various ageing protocols. Periodic performance tests were conducted to record the state of the cells at different stages of the ageing process. The investigation revealed a difference in entropy profiles during charge and discharge, indicating an entropy hysteresis related to path-dependent reaction mechanisms in the electrode materials. Changes in entropy hysteresis with age inferred qualitative changes in cell material morphology. For calendar-aged cells, the entropy profile magnitudes remained almost unchanged with age, whereas in cycle-aged cells, there was a decrease in entropy magnitude during discharge and an increase during charge, indicating particle breaking and cracking induced by cycling.

The study compared entropy profiling with DVA and ICA, and showed that entropy profiling could successfully track ageing markers such as LAM_{PE}, LAM_{NE} and LLI, with greater sensitivity to changes and features at some operating voltages that are not accessible by DVA. This means that entropy profiling is a unique noninvasive tool that can be successfully used in degradation diagnosis. However, its application is impeded by practicality; a time-consuming process with a demanding setup.

5.1.2 effective inclusion of predicted degradation within the battery model

Conventionally, some degradation effects can be incorporated into existing models by coupling them with specific degradation mechanism models. However, this approach requires more complex models, accurate assumptions, and prior knowledge of duty cycles and the environment. Consequently, this approach leads to increased model complexity, which is unsuitable for BMS purposes. In this investigation, an alternative approach was proposed, in which the BMS periodically performs a numerical parameter re-evaluation over the battery's life instead of incorporating separate 'open-loop' degradation models.

In this investigation, the single particle model was used as a base model for which several parameters were found to change with ageing. These parameters included diffusion time, stoichiometry, kinetic rate constant, and active material volume fraction. The decrease in the kinetic rate constant with cycling caused a substantial rise in irreversible heating. An increase in both kinetic overpotential and solid diffusion time led to an elongated CV phase since the cut-off voltage limit was reached sooner.

The impact of this work is two-fold. Firstly, it demonstrates how the SPM can accurately simulate both pristine and aged cell voltage responses if model parameters are updated accordingly. From a battery management system perspective, this ensures an accurate state of charge, power estimation, and maximum use of available capacity throughout the battery life. Secondly, this study provides qualitative insight into the impact of ageing on model parameters, which informs safety issues such as increased heat generation.

5.1.3 Accurate prediction of battery internal states at high current rates

This study aimed to fill the gap of battery modelling at high C-rates (10C target), especially during charging, and answer two questions:

- Is it possible to model accurately the internal states of the cell at high C-rate conditions with current battery models if the limiting condition is not reached?
- Is there an additional current dependency or dynamics, that become more prevalent with C-rate increase, that state-of-the-art models do not account for?

To address these questions, a high-power cell was tested up to 10C and modelled through a pseudo-3D multi-physics model. An optimisation approach was used to identify a number of thermal and electrochemical parameters including diffusion time. The optimisation yielded favourable results for the thermal parameters and was able

to fit the instantaneous voltage drop following a current pulse well, however, it led to an overestimation in diffusion time. The contribution of heat from the diffusion overpotential was relatively low compared to the total heat generated. This, combined with the significantly faster diffusion times needed to satisfy the validation data conditions, led to the assumption that the diffusion time could be considered almost infinitely fast for the power cell tested under the given conditions.

The continuum model with linearised kinetics and infinitely fast diffusion for both electrolyte and solid phases provided good accuracy (in terms of voltage and temperature outputs) for the studied power cell, even at 10C. This means that the additional complexity of existing models, for example the focus on 1D+1D DFN approaches, might be in the wrong place. Instead of adding more transport mechanisms, it has been shown here that long-range temperature variations and temperature dependence of parameters are particularly important for predicting large pouch cell behaviour. These results offer the most accurate thermal prediction to date at 10C. However, the model's accuracy could be further improved with a revised model and parametrisation procedure, to obtain better agreement between training and validation data.

5.2 Limitations and further work

While this thesis contributes to the understanding of cell degradation and thermal modelling and highlights the resultant implications for an EV BMS, it also reveals several avenues of research that remain unexplored.

5.2.1 Battery degradation diagnosis

Proposed in Chapter 2, entropy profiling for the diagnosis of battery health proved as informative as DVA and ICA in degradation mode identification. However, there are still unanswered questions, and future work should focus on exploring the relation-

ship between entropy and morphological changes. This research could enhance our understanding of microscopic changes without requiring cell tear-down, surpassing the capabilities of DVA degradation diagnosis. Specifically, it would involve correlating particle size and electrode porosity with entropy magnitude and shape. Due to the challenges posed by entropy measurement, there is a need for an improved technique that is time-efficient and easily implementable in a varied environment. Such a technique would benefit not only entropy use in degradation prognosis but also in thermal modelling.

Integrating degradation information into a BMS is not a straightforward task. The periodic SPM parameter update method proposed in Chapter 3 was successful in the presented study, but it may face challenges in real EV applications. In addition to the prevalent anode degradation found in this study, cathodic changes can also occur, further complicating parameter identification. The model used assumed no electrolyte dynamics, however with battery ageing, electrolyte degradation may occur [181] and inflict limiting conditions on the cell, which could be otherwise attributed to an electrode. Therefore, it would be valuable to investigate model parameter updates with electrolyte inclusion.

In EV applications, multiple cells are stacked together, and they are likely to experience inhomogeneous degradation. Thus, adjusting parameters for a single cell may not be effective for the entire pack and may not be computationally feasible. While simpler models such as ECMs may be preferred for parameter updates in a BMS, finding an efficient method for updating the parameters for the entire pack remains a challenge.

5.2.2 Modelling at high C-rates

Literature on power cell modelling is lacking, and Chapter 4 has shown that not all dynamics and conclusions drawn from thicker electrode cells are necessarily applicable

to high-power cell applications. More research should focus on informing decisions about which dynamics to model and which ones to exclude. A useful metric for this could be the identification of limiting conditions and an assessment of which condition occurs first (if any) in a given application, but this would need further research.

Numerous studies have emphasised the importance of the solid diffusion coefficient change with lithiation, which was also investigated in Chapter 3. However, when more attention was focused on the solid diffusion problem in Chapter 4, it was revealed that its functional dependency on lithiation has a negligible impact on simulated voltage (if solid diffusion limiting condition is not reached) but adding the dependence on lithiation increases model complexity and solution time. Current techniques for solid diffusion coefficient estimation are limited, and more research is required to improve and harmonise these techniques. Additionally, more thought should be given to a general consideration of whether lithiation-dependence improves model accuracy or provides model redundancy. With the increasing production rate of cells and increased amount of variants available on the market, improvement in characterisation techniques (either experimental or parameter fitting) is sought.

References

[1] M. E. Wojtala, A. A. Zülke, R. Burrell, M. Nagarathinam, G. Li, H. E. Hoster, D. A. Howey, and M. P. Mercer, "Entropy Profiling for the Diagnosis of NCA/Gr-SiOx Li-Ion Battery Health," *Journal of The Electrochemical Society*, vol. 169, no. 10, p. 100527, 2022.

[2] M. E. Wojtala, F. B. Planella, A. A. Zulke, H. E. Hoster, and D. A. Howey, "Investigating changes in transport, kinetics and heat generation over nca/gr-siox battery lifetime," in *2022 IEEE Vehicle Power and Propulsion Conference (VPPC)*, pp. 1–6, IEEE, 2022.

[3] M. E. Wojtala, A. A. Zulke, R. Burrell, M. P. Mercer, H. Hoster, and D. Howey, "Entropy hysteresis during lithiation/delithiation of nca/gr-si battery subjected to accelerated calendar ageing and cycle ageing," in *Electrochemical Society Meeting Abstracts 241*, pp. 528–528, ECS, 2022.

[4] M. E. Wojtala, V. Kumptepeli, C. W. Monroe, and D. A. Howey, "Li-ion battery in high c-rate conditions: im-proving the temperature prediction," in *ModVal 2023-19th Symposium on Fuel Cell and Battery Modeling and Experimental Validation*, p. 39, ModVal, 2023.

[5] A. A. Zulke, M. Wojtala, H. E. Hoster, and D. Howey, "Tracking thermodynamic changes due to cycling and calendar ageing of commercial high-energy

li-ion cells: Effects of relaxation periods," in *Electrochemical Society Meeting Abstracts PRiME 2020*, pp. 104–104, ECS, 2020.

[6] J. Lin, H. N. Chu, K. Thu, M. Wojtala, F. Gao, and K. J. Chua, "Novel battery thermal management via scalable dew-point evaporative cooling," *Energy Conversion and Management*, vol. 283, p. 116948, 2023.

[7] P. J. Osswald, M. Del Rosario, J. Garche, A. Jossen, and H. E. Hoster, "Fast and Accurate Measurement of Entropy Profiles of Commercial Lithium-Ion Cells," *Electrochimica Acta*, vol. 177, pp. 270–276, 2015.

[8] H. A. Gabbar, A. M. Othman, and M. R. Abdussami, "Review of Battery Management Systems (BMS) Development and Industrial Standards," *Technologies*, vol. 9, no. 2, p. 28, 2021.

[9] F. Baronti, C. Bernardeschi, L. Cassano, A. Domenici, R. Roncella, and R. Saletti, "Design and safety verification of a distributed charge equalizer for modular li-ion batteries," *IEEE Trans. Industr. Inform.*, vol. 10, no. 2, pp. 1003–1011, 2014.

[10] A. Barré, B. Deguilhem, S. Grolleau, M. Gérard, F. Suard, and D. Riu, "A review on lithium-ion battery ageing mechanisms and estimations for automotive applications," *J. Power Sources*, vol. 241, pp. 680–689, 2013.

[11] M. Lucu, E. Martinez-Laserna, I. Gandiaga, and H. Camblong, "A critical review on self-adaptive Li-ion battery ageing models," *J. Power Sources*, vol. 401, pp. 85–101, 2018.

[12] M. Muratori, M. Alexander, D. Arent, M. Bazilian, P. Cazzola, E. M. Dede, J. Farrell, C. Gearhart, D. Greene, A. Jenn, M. Keyser, T. Lipman, S. Narumanchi, A. Pesaran, R. Sioshansi, E. Suomalainen, G. Tal, K. Walkowicz, and

J. Ward, "The rise of electric vehicles—2020 status and future expectations," *Prog. Energy*, vol. 3, no. 2, p. 022002, 2021.

[13] V. Sulzer, P. Mohtat, A. Aitio, S. Lee, Y. T. Yeh, F. Steinbacher, M. U. Khan, J. W. Lee, J. B. Siegel, A. G. Stefanopoulou, and D. A. Howey, "The challenge and opportunity of battery lifetime prediction from field data," *Joule*, vol. 5, no. 8, pp. 1934–1955, 2021.

[14] G. L. Plett, *Battery management systems, Volume II: Equivalent-circuit methods*. Artech House, 2015.

[15] M. Doyle, T. F. Fuller, and J. Newman, "Modeling of Galvanostatic Charge and Discharge of the Lithium/Polymer/Insertion Cell," *Journal of The Electrochemical Society*, vol. 140, no. 6, pp. 1526–1533, 1993.

[16] T. F. Fuller, M. Doyle, and J. Newman, "Simulation and optimization of the dual lithium ion insertion cell," *Journal of the electrochemical society*, vol. 141, no. 1, p. 1, 1994.

[17] F. Brosa-Planella, W. Ai, B. W, M, A. Gosh, I. Korotkin, S. Sahu, V. Sulzer, R. Timms, T. G. Tranter, M. Zyskin, S. J. Cooper, J. S. Edge, J. M. Foster, M. Marinescu, B. Wu, and G. Richardson, "A continuum of physics-based lithium-ion battery models reviewed Progress in Energy OPEN ACCESS A continuum of physics-based lithium-ion battery models reviewed," *Progress in Energy*, vol. 4, 2022.

[18] J. Li, N. Lotfi, R. G. Landers, and J. Park, "A Single Particle Model for Lithium-Ion Batteries with Electrolyte and Stress-Enhanced Diffusion Physics," *Journal of The Electrochemical Society*, vol. 164, no. 4, pp. A874–A883, 2017.

[19] S. G. Marquis, V. Sulzer, R. Timms, C. P. Please, and S. J. Chapman, "An asymptotic derivation of a single particle model with electrolyte," *Journal of The Electrochemical Society*, vol. 166, no. 15, pp. A3693–A3706, 2019.

[20] J. Lin, H. N. Chu, D. A. Howey, and C. W. Monroe, "Multiscale coupling of surface temperature with solid diffusion in large lithium-ion pouch cells," *Communications Engineering*, vol. 1, no. 1, pp. 1–10, 2022.

[21] Y. K. Lee, J. Song, and J. Park, "Multi-scale coupled mechanical-electrochemical modeling for study on stress generation and its impact on multi-layered electrodes in lithium-ion batteries," *Electrochimica Acta*, vol. 389, p. 138682, 2021.

[22] L. M. Morgan, M. P. Mercer, A. Bhandari, C. Peng, M. M. Islam, H. Yang, J. Holland, S. W. Coles, R. Sharpe, A. Walsh, *et al.*, "Pushing the boundaries of lithium battery research with atomistic modelling on different scales," *Progress in Energy*, vol. 4, no. 1, p. 012002, 2021.

[23] R. Romagnoli, L. D. Couto, A. Goldar, M. Kinnaert, and E. Garone, "A feedback charge strategy for Li-ion battery cells based on Reference Governor," *Journal of Process Control*, vol. 83, pp. 164–176, 2019.

[24] S. Park, D. Kato, Z. Gima, R. Klein, and S. Moura, "Optimal Experimental Design for Parameterization of an Electrochemical Lithium-Ion Battery Model," *Journal of The Electrochemical Society*, vol. 165, no. 7, pp. A1309–A1323, 2018.

[25] A. M. Bizeray, J. H. Kim, S. R. Duncan, and D. A. Howey, "Identifiability and Parameter Estimation of the Single Particle Lithium-Ion Battery Model," *IEEE Transactions on Control Systems Technology*, pp. 1–16, 2018.

[26] F. Brosa Planella, M. Sheikh, and W. Widanage, "Systematic derivation and validation of a reduced thermal-electrochemical model for lithium-ion batteries using asymptotic methods," *Electrochimica Acta*, vol. in press, 2021.

[27] A. M. Bizeray, J. H. Kim, S. R. Duncan, and D. A. Howey, "Identifiability and Parameter Estimation of the Single Particle Lithium-Ion Battery Model," *IEEE Transactions on Control Systems Technology*, vol. 27, no. 5, pp. 1862–1877, 2019.

[28] S. J. Moura, F. B. Argomedo, R. Klein, A. Mirtabatabaei, and M. Krstic, "Battery state estimation for a single particle model with electrolyte dynamics," *IEEE Transactions on Control Systems Technology*, vol. 25, no. 2, pp. 453–468, 2017.

[29] C. H. Chen, F. Brosa Planella, K. O'Regan, D. Gastol, W. D. Widanage, and E. Kendrick, "Development of Experimental Techniques for Parameterization of Multi-scale Lithium-ion Battery Models," *Journal of The Electrochemical Society*, vol. 167, no. 8, p. 080534, 2020.

[30] M. Ecker, T. K. D. Tran, P. Dechent, S. Käbitz, A. Warnecke, and D. U. Sauer, "Parameterization of a Physico-Chemical Model of a Lithium-Ion Battery," *Journal of The Electrochemical Society*, vol. 162, no. 9, pp. A1836–A1848, 2015.

[31] C. Pastor-Fernández, T. F. Yu, W. D. Widanage, and J. Marco, "Critical review of non-invasive diagnosis techniques for quantification of degradation modes in lithium-ion batteries," *Renewable and Sustainable Energy Reviews*, vol. 109, no. April, pp. 138–159, 2019.

[32] A. Nyman, M. Behm, and G. Lindbergh, "Electrochemical characterisation and modelling of the mass transport phenomena in LiPF6-EC-EMC electrolyte," *Electrochimica Acta*, vol. 53, no. 22, pp. 6356–6365, 2008.

[33] M. D. Galluzzo, W. S. Loo, A. A. Wang, A. Walton, J. A. Maslyn, and N. P. Balsara, "Measurement of Three Transport Coefficients and the Thermodynamic Factor in Block Copolymer Electrolytes with Different Morphologies," *Journal of Physical Chemistry B*, vol. 124, no. 5, pp. 921–935, 2020.

[34] A. A. Wang, T. Hou, M. Karanjavala, and C. W. Monroe, "Shifting-reference concentration cells to refine composition-dependent transport characterization of binary lithium-ion electrolytes," *Electrochimica Acta*, vol. 358, p. 136688, 2020.

[35] I. Y. Shilov and A. Lyashchenko, "Activity coefficient modeling for aqueous aluminum salt solutions in terms of the generalized debye–hückel theory," *Russian Journal of Inorganic Chemistry*, vol. 64, pp. 1186–1189, 2019.

[36] G. GirishKumar, W. H. Bailey, B. K. Peterson, and W. J. Casteel, "Electrochemical and spectroscopic investigations of the overcharge behavior of stabilife electrolyte salts in lithium-ion batteries," *Journal of The Electrochemical Society*, vol. 158, no. 2, p. A146, 2010.

[37] H. N. Chu, S. U. Kim, S. K. Rahimian, J. B. Siegel, and C. W. Monroe, "Parameterization of prismatic lithium–iron–phosphate cells through a streamlined thermal/electrochemical model," *Journal of Power Sources*, vol. 453, p. 227787, 2020.

[38] X. Y. Qiu, Q. C. Zhuang, Q. Q. Zhang, R. Cao, P. Z. Ying, Y. H. Qiang, and S. G. Sun, "Electrochemical and electronic properties of LiCoO 2 cathode investigated by galvanostatic cycling and EIS," *Physical Chemistry Chemical Physics*, vol. 14, no. 8, pp. 2617–2630, 2012.

[39] A. Aitio, S. G. Marquis, P. Ascencio, and D. Howey, "Bayesian parameter estimation applied to the li-ion battery single particle model with electrolyte dynamics," *IFAC-PapersOnLine*, vol. 53, no. 2, pp. 12497–12504, 2020.

[40] A. Aitio, *Bayesian methods for battery state of health estimation.* PhD thesis, University of Oxford, 2023.

[41] S. J. Moura, N. A. Chaturvedi, and M. Krstić, "Adaptive partial differential equation observer for battery state-of-charge/state-of-health estimation via an electrochemical model," *J. Dyn. Syst. Meas. Control Trans. ASME*, vol. 136, no. 1, pp. 1–11, 2014.

[42] Y. Kuhn, H. Wolf, A. Latz, and B. Horstmann, "Bayesian Parameterization of Continuum Battery Models from Featurized Electrochemical Measurements Considering Noise**," *Batteries and Supercaps*, vol. 6, no. 1, 2023.

[43] Y. Zhu and C. Wang, "Galvanostatic intermittent titration technique for phase-transformation electrodes," *Journal of Physical Chemistry C*, vol. 114, no. 6, pp. 2830–2841, 2010.

[44] R. Jung, F. Linsenmann, R. Thomas, J. Wandt, S. Solchenbach, F. Maglia, C. Stinner, M. Tromp, and H. A. Gasteiger, "Nickel, Manganese, and Cobalt Dissolution from Ni-Rich NMC and Their Effects on NMC622-Graphite Cells," *Journal of The Electrochemical Society*, vol. 166, no. 2, pp. A378–A389, 2019.

[45] J. Newman and W. Tiedemann, "Potential and Current Distribution in Electrochemical Cells: Interpretation of the Half-Cell Voltage Measurements as a Function of Reference-Electrode Location," *Journal of The Electrochemical Society*, vol. 140, no. 7, pp. 1961–1968, 1993.

[46] B. J. Lanterman, A. A. Riet, N. S. Gates, J. D. Flygare, A. D. Cutler, J. E. Vogel, D. R. Wheeler, and B. A. Mazzeo, "Micro-Four-Line Probe to Measure

Electronic Conductivity and Contact Resistance of Thin-Film Battery Electrodes," *Journal of The Electrochemical Society*, vol. 162, no. 10, pp. A2145–A2151, 2015.

[47] C. Capiglia, Y. Saito, H. Kageyama, P. Mustarelli, T. Iwamoto, T. Tabuchi, and H. Tukamoto, "7 Li and 19 F diffusion coefficients and thermal properties of non-aqueous electrolyte solutions for rechargeable lithium batteries," *Journal of Power Sources*, vol. 81-82, pp. 859–862, 1999.

[48] P. de Maria, A. Fontana, S. Frascri, G. Gargaro, D. Spinelli, and M. O. Tinti, "Effect of the addition of electrolytes on the partition coefficients, activity coefficients, and acid dissociation constants of carnitine and its acetyl and propionyl derivatives," *Journal of pharmaceutical sciences*, vol. 83, no. 5, pp. 742–746, 1994.

[49] G. White, A. Hales, Y. Patel, and G. Offer, "Novel methods for measuring the thermal diffusivity and the thermal conductivity of a lithium-ion battery," *Applied Thermal Engineering*, vol. 212, p. 118573, 2022.

[50] L. Rao and J. Newmann, "Heat Generation Rate and General Energy Balance for insertion battery systems," *Journal of The Electrochemical Society*, vol. 144, no. 8, p. 399, 1997.

[51] B. Shabani and M. Biju, "Theoretical modelling methods for thermal management of batteries," *Energies*, vol. 8, no. 9, pp. 10153–10177, 2015.

[52] R. Richardson, *Impedance-based battery temperature monitoring.* PhD thesis, University of Oxford, 2016.

[53] X. Lin, H. Fu, H. E. Perez, J. B. Siege, A. G. Stefanopoulou, Y. Ding, and M. P. Castanier, "Parameterization and observability analysis of scalable battery clus-

ters for onboard thermal management," *Oil & Gas Science and Technology–Revue d'IFP Energies nouvelles*, vol. 68, no. 1, pp. 165–178, 2013.

[54] C. Forgez, D. Vinh Do, G. Friedrich, M. Morcrette, and C. Delacourt, "Thermal modeling of a cylindrical LiFePO4/graphite lithium-ion battery," *Journal of Power Sources*, vol. 195, pp. 2961–2968, may 2010.

[55] X. Li, F. He, and L. Ma, "Thermal management of cylindrical batteries investigated using wind tunnel testing and computational fluid dynamics simulation," *Journal of power sources*, vol. 238, pp. 395–402, 2013.

[56] R. Mahamud, *Advanced battery thermal management for electrical-drive vehicles using reciprocating cooling flow and spatial-resolution, lumped-capacitance thermal model*. PhD thesis, University of Nevada, Reno, 2011.

[57] Y. Zhao, Y. Patel, T. Zhang, and G. J. Offer, "Modeling the Effects of Thermal Gradients Induced by Tab and Surface Cooling on Lithium Ion Cell Performance," *Journal of The Electrochemical Society*, vol. 165, no. 13, pp. A3169–A3178, 2018.

[58] T. Evans and R. E. White, "A thermal analysis of a spirally wound battery using a simple mathematical model," *Journal of The Electrochemical Society*, vol. 136, no. 8, p. 2145, 1989.

[59] S. Al Hallaj, H. Maleki, J. S. Hong, and J. R. Selman, "Thermal modeling and design considerations of lithium-ion batteries," *Journal of Power Sources*, vol. 83, no. 1-2, pp. 1–8, 1999.

[60] H. N. Chu, *Characterization of coupled transport phenomena in large-format lithium-ion batteries*. PhD thesis, University of Oxford, 2021.

[61] C. R. Birkl, M. R. Roberts, E. McTurk, P. G. Bruce, and D. A. Howey, "Degradation diagnostics for lithium ion cells," *Journal of Power Sources*, vol. 341, pp. 373–386, 2017.

[62] K. Uddin, S. Perera, W. D. Widanage, L. Somerville, and J. Marco, "Characterising lithium-ion battery degradation through the identification and tracking of electrochemical battery model parameters," *Batteries*, vol. 2, no. 2, 2016.

[63] J. S. Edge, S. O'Kane, R. Prosser, N. D. Kirkaldy, A. N. Patel, A. Hales, A. Ghosh, W. Ai, J. Chen, J. Yang, S. Li, M. C. Pang, L. Bravo Diaz, A. Tomaszewska, M. W. Marzook, K. N. Radhakrishnan, H. Wang, Y. Patel, B. Wu, and G. J. Offer, "Lithium ion battery degradation: what you need to know," *Physical Chemistry Chemical Physics*, vol. 23, no. 14, pp. 8200–8221, 2021.

[64] C. Birkl, *Diagnosis and prognosis of degradation in lithium-ion batteries*. Thesis, The University of Oxford, 2017.

[65] D. Yu, M. Zhao, and H. Hoster, "Suppressing Vertical Displacement of Lithiated Silicon Particles in High Volumetric Capacity Battery Electrodes," *ChemElectroChem*, vol. 8, no. 2, pp. 1090–1095, 2015.

[66] E. Moyassari, T. Roth, S. Kücher, C.-C. Chang, S.-C. Hou, F. B. Spingler, and A. Jossen, "The Role of Silicon in Silicon-Graphite Composite Electrodes Regarding Specific Capacity, Cycle Stability, and Expansion," *Journal of The Electrochemical Society*, vol. 169, no. 1, p. 010504, 2022.

[67] S. Goutam, N. Omar, P. Van Den Bossche, and J. Van Mierlo, "Chapter Two - Review of Nanotechnology for Anode Materials in Batteries," in *Emerging Nanotechnologies in Rechargeable Energy Storage Systems* (L. M. Rodriguez-

Martinez and N. Omar, eds.), Micro and Nano Technologies, pp. 45–82, Boston: Elsevier, 2017.

[68] A. Wang, S. Kadam, H. Li, S. Shi, and Y. Qi, "Review on modeling of the anode solid electrolyte interphase (SEI) for lithium-ion batteries," *npj Computational Materials*, vol. 4, p. 15, dec 2018.

[69] M. Dubarry, V. Svoboda, R. Hwu, and B. Yann Liaw, "Incremental Capacity Analysis and Close-to-Equilibrium OCV Measurements to Quantify Capacity Fade in Commercial Rechargeable Lithium Batteries," *Electrochemical and Solid-State Letters*, vol. 9, no. 10, p. A454, 2006.

[70] M. Dubarry, C. Truchot, and B. Y. Liaw, "Synthesize battery degradation modes via a diagnostic and prognostic model," *Journal of Power Sources*, vol. 219, pp. 204–216, dec 2012.

[71] M. Berecibar, M. Dubarry, N. Omar, I. Villarreal, and J. V. Mierlo, "Degradation Mechanism Detection for NMC Batteries based on Incremental Capacity Curves," *World Electric Vehicle Journal*, vol. 8, no. 2, pp. 350–361, 2018.

[72] B. Wu, Z. Li, and J. Zhang, "Thermal Design for the Pouch-Type Large-Format Lithium-Ion Batteries I. Thermo-Electrical Modeling and Origins of Temperature Non-Uniformity," *Journal of The Electrochemical Society*, vol. 162, no. 1, pp. 181–191, 2015.

[73] J. P. Schmidt, A. Weber, and E. Ivers-Tiffée, "A novel and precise measuring method for the entropy of lithium-ion cells: deltaS via electrothermal impedance spectroscopy," *Electrochimica Acta*, vol. 137, pp. 311–319, 2014.

[74] J. P. Sullivan, K. R. Fenton, F. El, G. Marquez, C. T. Harris, C. Carl, N. S. Hudak, K. L. Jungjohann, C. J. Kliewer, K. Mccarty, A. H. Mcdaniel, G. Nagasubramanian, D. Joshua, A. A. Talin, C. M. Tenney, and K. R. Zavadil,

"The Science of Battery Degradation," Tech. Rep. January, Sandia National Laboratories, Livermore, 2015.

[75] K. Maher and R. Yazami, "A study of lithium ion batteries cycle aging by thermodynamics techniques," *Journal of Power Sources*, vol. 247, pp. 527–533, 2014.

[76] X. F. Zhang, Y. Zhao, Y. Patel, T. Zhang, W. M. Liu, M. Chen, G. J. Offer, and Y. Yan, "Potentiometric measurement of entropy change for lithium batteries," *Physical Chemistry Chemical Physics*, vol. 19, no. 15, pp. 9833–9842, 2017.

[77] M. Dubarry, C. Truchot, and B. Y. Liaw, "Synthesize battery degradation modes via a diagnostic and prognostic model," *Journal of Power Sources*, vol. 219, pp. 204–216, 2012.

[78] J. Schmitt, M. Schindler, and A. Jossen, "Change in the half-cell open-circuit potential curves of silicon–graphite and nickel-rich lithium nickel manganese cobalt oxide during cycle aging," *J. Power Sources*, vol. 506, p. 230240, 2021.

[79] I. Bloom, J. Christophersen, and K. Gering, "Differential voltage analyses of high-power lithium-ion cells 2. Applications," *J. Power Sources*, vol. 139, no. 1-2, pp. 304–313, 2005.

[80] P. Keil and A. Jossen, "Calendar Aging of NCA Lithium-Ion Batteries Investigated by Differential Voltage Analysis and Coulomb Tracking," *Journal of The Electrochemical Society*, vol. 164, no. 1, pp. A6066–A6074, 2017.

[81] E. Riviere, A. Sari, P. Venet, F. Meniere, and Y. Bultel, "Innovative Incremental Capacity Analysis Implementation for C/LiFePO4 Cell State-of-Health Estimation in Electrical Vehicles," *Batteries*, vol. 5, no. 2, p. 37, 2019.

[82] P. Keil, S. F. Schuster, J. Wilhelm, J. Travi, A. Hauser, R. C. Karl, and A. Jossen, "Calendar Aging of Lithium-Ion Batteries," *Journal of The Electrochemical Society*, vol. 163, no. 9, pp. A1872–A1880, 2016.

[83] A. Zülke, Y. Li, P. Keil, R. Burrell, S. Belaisch, M. Nagarathinam, M. P. Mercer, and H. E. Hoster, "High-Energy Nickel-Cobalt-Aluminium Oxide (NCA) Cells on Idle: Anode- versus Cathode-Driven Side Reactions," *Batteries and Supercaps*, vol. 4, pp. 1–15, 2021.

[84] B. Wu, V. Yufit, Y. Merla, R. F. Martinez-Botas, N. P. Brandon, and G. J. Offer, "Differential thermal voltammetry for tracking of degradation in lithium-ion batteries," *Journal of Power Sources*, vol. 273, pp. 495–501, jan 2015.

[85] Y. Merla, B. Wu, V. Yufit, N. P. Brandon, R. F. Martinez-Botas, and G. J. Offer, "Novel application of differential thermal voltammetry as an in-depth state-of-health diagnosis method for lithium-ion batteries," *Journal of Power Sources*, vol. 307, no. March, pp. 308–319, 2016.

[86] D. I. Stroe, M. Swierczynski, A. I. Stan, V. Knap, R. Teodorescu, and S. J. Andreasen, "Diagnosis of lithium-ion batteries state-of-health based on electrochemical impedance spectroscopy technique," *2014 IEEE Energy Conversion Congress and Exposition, ECCE 2014*, pp. 4576–4582, 2014.

[87] Y. Li, J. Guo, K. Pedersen, L. Gurevich, and D. I. Stroe, "Recent Health Diagnosis Methods for Lithium-Ion Batteries," *Batteries*, vol. 8, no. 7, 2022.

[88] E. Barsoukov and J. R. Macdonald, "Impedance spectroscopy theory, experiment, and," *Applications, 2nd ed.(Hoboken, NJ: John Wiley &Sons, Inc., 2005)*, 2005.

[89] M. E. Orazem and B. Tribollet, "Electrochemical impedance spectroscopy," *New Jersey*, vol. 1, pp. 383–389, 2008.

[90] J. P. Meyers, M. Doyle, R. M. Darling, and J. Newman, "The impedance response of a porous electrode composed of intercalation particles," *Journal of The Electrochemical Society*, vol. 147, no. 8, p. 2930, 2000.

[91] C. Pastor-Fernández, K. Uddin, G. H. Chouchelamane, W. D. Widanage, and J. Marco, "A Comparison between Electrochemical Impedance Spectroscopy and Incremental Capacity-Differential Voltage as Li-ion Diagnostic Techniques to Identify and Quantify the Effects of Degradation Modes within Battery Management Systems," *Journal of Power Sources*, vol. 360, pp. 301–318, 2017.

[92] L. Krause, L. Jensen, and J. Dahn, "Measurement of parasitic reactions in li ion cells by electrochemical calorimetry," *Journal of the Electrochemical Society*, vol. 159, pp. A937–A943, 01 2012.

[93] E. Bernardi, Dawn Pawlikowski and J. Newman, "A general energy balance for battery systems," *J. Electrochem. Soc*, vol. 132, no. 1, pp. 5–12, 1985.

[94] L. E. Downie, S. R. Hyatt, A. T. Wright, and J. R. Dahn, "Determination of the time dependent parasitic heat flow in lithium ion cells using isothermal microcalorimetry," *Journal of Physical Chemistry C*, vol. 118, no. 51, pp. 29533–29541, 2014.

[95] N. S. Hudak, L. E. Davis, and G. Nagasubramanian, "Cycling-Induced Changes in the Entropy Profiles of Lithium Cobalt Oxide Electrodes by Nicholas S. Hudak, Lorie E. Davis, and Ganesan Nagasubramanian Sandia National Laboratories Albuquerque, New Mexico, U.S.A.," tech. rep., Sandia National Laboratories, Albuquerque, 2014.

[96] S. Bach, J. P. Pereira-Ramos, N. Baffier, and R. Messina, "Thermodynamic data of electrochemical lithium intercalation in Li x Mn 2 O 4," *Electrochimica Acta*, vol. 37, no. 7, pp. 1301–1305, 1992.

[97] J. S. Hong, H. Maleki, S. Al Hallaj, L. Redey, and J. R. Selman, "Electrochemical-Calorimetric Studies of Lithium-Ion Cells," *J. Electrochem. Soc*, vol. 145, no. 5, pp. 1489–1493, 1998.

[98] G. Liu, M. Ouyang, L. Lu, J. Li, and X. Han, "Analysis of the heat generation of lithium-ion battery during charging and discharging considering different influencing factors," *Journal of Thermal Analysis and Calorimetry*, vol. 116, no. 2, pp. 1001–1010, 2014.

[99] K. E. Thomas, C. Bogatu, and J. Newman, "Measurement of the Entropy of Reaction as a Function of State of Charge in Doped and Undoped Lithium Manganese Oxide," *Journal of The Electrochemical Society*, vol. 148, no. 6, pp. 570–575, 2001.

[100] S. Wang, S. Jin, D. Deng, and C. Fernandez, "A critical review of online battery remaining useful lifetime prediction methods," *Front. Mech. Eng.*, vol. 7, pp. 719718–719737, 2021.

[101] G. Li and C. W. Monroe, "Multiscale Lithium-Battery Modeling from Materials to Cells," *Annu. Rev. Chem. Biomol. Eng.*, vol. 11, pp. 277–310, 2020.

[102] G. Assat, S. L. Glazier, C. Delacourt, and J. M. Tarascon, "Probing the thermal effects of voltage hysteresis in anionic redox-based lithium-rich cathodes using isothermal calorimetry," *Nat. Energy*, vol. 4, no. 8, pp. 647–656, 2019.

[103] M. P. Mercer, C. Peng, C. Soares, H. E. Hoster, and D. Kramer, "Voltage hysteresis during lithiation/delithiation of graphite associated with meta-stable carbon stackings," *J. Mater. Chem. A*, vol. 9, pp. 492–504, 2021.

[104] D. Allart, M. Montaru, and H. Gualous, "Model of lithium intercalation into graphite by potentiometric analysis with equilibrium and entropy change curves

of graphite electrode," *J. Electrochem. Soc.*, vol. 165, no. 2, pp. A380–A387, 2018.

[105] K. E. Thomas and J. Newman, "Heats of mixing and of entropy in porous insertion electrodes," *J. Power Sources*, vol. 119-121, pp. 844 – 849, 2003.

[106] Y. Reynier, J. Graetz, S. Tabitha, P. Rez, R. Yazami, and B. Fultz, "Entropy of Li intercalation in LixCoO2," *Phys. Rev. B*, vol. 70, p. 174304, 2004.

[107] M. P. Mercer, S. Finnigan, D. Kramer, D. Richards, and H. E. Hoster, "The influence of point defects on the entropy profiles of Lithium Ion Battery cathodes: a lattice-gas Monte Carlo study," *Electrochim. Acta*, vol. 241, pp. 141–152, 2017.

[108] M. P. Mercer, M. Otero, M. Ferrer-Huerta, A. Sigal, D. E. Barraco, H. E. Hoster, and E. P. M. Leiva, "Transitions of lithium occupation in graphite: A physically informed model in the dilute lithium occupation limit supported by electrochemical and thermodynamic measurements," *Electrochim. Acta*, vol. 324, p. 134774, 2019.

[109] A. Eddahech, O. Briat, and J. M. Vinassa, "Thermal characterization of a high-power lithium-ion battery: Potentiometric and calorimetric measurement of entropy changes," *Energy*, vol. 61, pp. 432–439, 2013.

[110] B. Manikandan, C. Yap, and P. Balaya, "Towards Understanding Heat Generation Characteristics of Li-Ion Batteries by Calorimetry, Impedance, and Potentiometry Studies," *Journal of The Electrochemical Society*, vol. 164, no. 12, pp. A2794–A2800, 2017.

[111] Y. Jiang, G. Offer, J. Jiang, M. Marinescu, and H. Wang, "Voltage hysteresis model for silicon electrodes for lithium ion batteries, including multi-step phase transformations, crystallization and amorphization," *J. Electrochem. Soc.*, vol. 167, no. 13, p. 130533, 2020.

[112] J. Yang, Z. Niu, G. Offer, J. Xuan, and H. Wang, "Insights into the Role of Silicon and Graphite in the Electrochemical Performance of Silicon/Graphite Blended Electrodes with a Multi-Material Porous Electrode Model," *Journal of The Electrochemical Society*, vol. 169, no. 2, p. 020568, 2022.

[113] F. Grimsmann, F. Brauchle, T. Gerbert, A. Gruhle, M. Knipper, and J. Parisi, "Hysteresis and current dependence of the thickness change of lithium-ion cells with graphite anode," *J. Energy Storage*, vol. 12, pp. 132–137, 2017.

[114] S. Schweidler, L. de Biasi, A. Schiele, P. Hartmann, T. Brezesinski, and J. Janek, "Volume Changes of Graphite Anodes Revisited: A Combined Operando X-ray Diffraction and In Situ Pressure Analysis Study," *J. Phys. Chem. C*, vol. 122, no. 16, pp. 8829–8835, 2018.

[115] T. Vorauer, P. Kumar, C. L. Berhaut, F. F. Chamasemani, P. H. Jouneau, D. Aradilla, S. Tardif, S. Pouget, B. Fuchsbichler, L. Helfen, S. Atalay, W. D. Widanage, S. Koller, S. Lyonnard, and R. Brunner, "Multi-scale quantification and modeling of aged nanostructured silicon-based composite anodes," *Communications Chemistry*, vol. 3, no. 1, pp. 1–11, 2020.

[116] G. M. Veith, M. Doucet, R. L. Sacci, B. Vacaliuc, J. K. Baldwin, and J. F. Browning, "Determination of the Solid Electrolyte Interphase Structure Grown on a Silicon Electrode Using a Fluoroethylene Carbonate Additive," *Scientific Reports*, vol. 7, no. 1, pp. 1–15, 2017.

[117] K. Kalaga, M. T. F. Rodrigues, S. E. Trask, I. A. Shkrob, and D. P. Abraham, "Calendar-life versus cycle-life aging of lithium-ion cells with silicon-graphite composite electrodes," *Electrochimica Acta*, vol. 280, pp. 221–228, 2018.

[118] M. Dubarry and D. Beck, "Analysis of Synthetic Voltage vs. Capacity Datasets for Big Data Li-ion Diagnosis and Prognosis," *Energies*, vol. 14, no. 9, 2021.

[119] I. Bloom, A. N. Jansen, D. P. Abraham, J. Knuth, S. A. Jones, V. S. Battaglia, and G. L. Henriksen, "Differential voltage analyses of high-power, lithium-ion cells 1. Technique and application," *J. Power Sources*, vol. 139, pp. 295–303, 2005.

[120] A. Zülke, Y. Li, P. Keil, and H. Hoster, "Communication—why high-precision coulometry and lithium plating studies on commercial lithium-ion cells require thermal baths," *J. Electrochem. Soc.*, vol. 166, no. 13, pp. A2921–A2923, 2019.

[121] S. Schlueter, R. Genieser, D. Richards, H. E. Hoster, and M. P. Mercer, "Quantifying structure dependent responses in Li-ion cells with excess Li spinel cathodes: matching voltage and entropy profiles through mean field models," *Phys. Chem. Chem. Phys.*, vol. 20, pp. 21417–21429, 2018.

[122] M. P. Mercer, S. Affleck, E. M. Gavilán-Arriazu, A. A. Zülke, P. A. Maughan, S. Trivedi, M. Fichtner, A. R. Munnangi, E. P. M. Leiva, and H. E. Hoster, "Sodiation of hard carbon: How separating enthalpy and entropy contributions can find transitions hidden in the voltage profile," *ChemPhysChem*, vol. 23, no. 5, p. e202100748, 2022.

[123] C. Didier, W. K. Pang, Z. Guo, S. Schmid, and V. K. Peterson, "Phase Evolution and Intermittent Disorder in Electrochemically Lithiated Graphite Determined Using in Operando Neutron Diffraction," *Chem. Mater.*, vol. 32, no. 6, pp. 2518–2531, 2020.

[124] K. G. Gallagher, D. W. Dees, A. Jansen, D. P. Abraham, and S. Kang, "A Volume Averaged Approach to the Numerical Modeling of Phase-Transition Intercalation Electrodes Presented for LixC6," *J. Electrochem. Soc.*, vol. 159, no. 12, pp. A2029–A2037, 2012.

[125] J. Lim, Y. Li, D. H. Alsem, H. So, S. C. Lee, P. Bai, D. A. Cogswell, X. Liu, N. Jin, Y. Yu, N. J. Salmon, D. A. Shapiro, M. Z. Bazant, T. Tyliszczak, and W. C. Chueh, "Origin and hysteresis of lithium compositional spatiodynamics within battery primary particles," *Science*, vol. 353, no. 6299, pp. 566–571, 2016.

[126] K. Ando, T. Matsuda, and D. Imamura, "Degradation diagnosis of lithium-ion batteries with a LiNi0.5Co0.2Mn0.3O2 and LiMn2O4 blended cathode using dV/dQ curve analysis," *Journal of Power Sources*, vol. 390, no. April, pp. 278–285, 2018.

[127] J. R. Dahn, "Phase diagram of LixC6," *Phys. Rev. B*, vol. 44, no. 17, pp. 9170–9177, 1991.

[128] K. Persson, V. A. Sethuraman, L. J. Hardwick, Y. Hinuma, A. Meng, Y. S.and van der Ven, V. Srinivasan, R. Kostecki, and G. Ceder, "Lithium diffusion in graphitic carbon," *J. Phys. Chem. Lett.*, vol. 1, no. 8, pp. 1176–1180, 2010.

[129] E. M. Gavilan-Arriazu, M. P. Mercer, O. A. Pinto, O. A. Oviedo, D. E. Barraco, H. E. Hoster, and E. P. M. Leiva, "Effect of temperature on the kinetics of electrochemical insertion of li-ions into a graphite electrode studied by kinetic monte carlo," *J. Electrochem. Soc.*, vol. 167, no. 1, p. 013533, 2019.

[130] G. Yinsheng, R. B. Smith, Z. Yu, D. K. Efetov, J. Wang, P. Kim, M. Z. Bazant, and L. E. Brus, "Li intercalation into graphite: Direct optical imaging and cahn–hilliard reaction dynamics," *J. Phys. Chem. Lett.*, vol. 7, no. 11, pp. 2151–2156, 2016.

[131] E. M. Gavilan-Arriazu, O. Pinto, B. A. López de Mishima, D. E. Barraco, O. A. Oviedo, and E. P. M. Leiva, "The kinetic origin of the daumas-hérold model

for the li-ion/graphite intercalation system," *Electrochem. commun.*, vol. 93, pp. 133–137, 2018.

[132] P. J. Osswald, S. V. Erhard, J. Wilhelm, H. E. Hoster, and A. Jossen, "Simulation and measurement of local potentials of modified commercial cylindrical cells," *J. Electrochem. Soc.*, vol. 162, no. 10, pp. A2099–A2105, 2015.

[133] J. Wilhelm, S. Seidlmayer, S. Erhard, M. Hofmann, R. Gilles, and A. Jossen, "In situ neutron diffraction study of lithiation gradients in graphite anodes during discharge and relaxation," *J. Electrochem. Soc.*, vol. 165, no. 9, pp. A1846–A1856, 2018.

[134] P. J. Osswald, S. V. Erhard, A. Rheinfeld, B. Rieger, H. E. Hoster, and A. Jossen, "Temperature dependency of state of charge inhomogeneities and their equalization in cylindrical lithium-ion cells," *J. Power Sources*, vol. 329, pp. 546–552, 2016.

[135] S. Müller, J. Eller, M. Ebner, C. Burns, J. Dahn, and V. Wood, "Quantifying inhomogeneity of lithium ion battery electrodes and its influence on electrochemical performance," *J. Electrochem. Soc.*, vol. 165, no. 2, pp. A339–A344, 2018.

[136] F. Grimsmann, T. Gerbert, F. Brauchle, A. Gruhle, J. Parisi, and M. Knipper, "Hysteresis and current dependence of the graphite anode color in a lithium-ion cell and analysis of lithium plating at the cell edge," *J. Energy Storage*, vol. 15, pp. 17–22, 2018.

[137] R. Yazami and Y. Reynier, "Thermodynamics and crystal structure anomalies in lithium-intercalated graphite," *Journal of Power Sources*, vol. 153, pp. 312–318, 2006.

[138] Y. Reynier, R. Yazami, and B. Fultz, "XRD evidence of macroscopic composition inhomogeneities in the graphite–lithium electrode," *J. Power Sources*, vol. 165, no. 2, pp. 616 – 619, 2007. IBA – HBC 2006.

[139] R. Burrell, A. Zulke, P. Keil, and H. Hoster, "Communication—Identifying and Managing Reversible Capacity Losses that Falsify Cycle Ageing Tests of Lithium-Ion Cells," *Journal of The Electrochemical Society*, vol. 167, no. 13, p. 130544, 2020.

[140] A. Grenier, H. Liu, K. M. Wiaderek, Z. W. Lebens-Higgins, O. J. Borkiewicz, L. F. Piper, P. J. Chupas, and K. W. Chapman, "Reaction heterogeneity in LiNi0.8Co0.15Al0.05O2 induced by surface layer," *Chem. Mater.*, vol. 29, no. 17, pp. 7345–7352, 2017.

[141] P. Xiao, T. Lv, X. Chen, and C. Chang, "LiNi0.8Co0.15Al0.05O2: Enhanced Electrochemical Performance from Reduced Cationic Disordering in Li Slab," *Sci. Rep.*, vol. 7, no. 1, pp. 1–8, 2017.

[142] A. J. Smith, P. Svens, M. Varini, G. Lindbergh, and R. W. Lindström, "Expanded In Situ Aging Indicators for Lithium-Ion Batteries with a Blended NMC-LMO Electrode Cycled at Sub-Ambient Temperature," *Journal of The Electrochemical Society*, vol. 168, no. 11, p. 110530, 2021.

[143] J. Moon, H. C. Lee, H. Jung, S. Wakita, S. Cho, J. Yoon, J. Lee, A. Ueda, B. Choi, S. Lee, K. Ito, Y. Kubo, A. C. Lim, J. G. Seo, J. Yoo, S. Lee, Y. Ham, W. Baek, Y. G. Ryu, and I. T. Han, "Interplay between electrochemical reactions and mechanical responses in silicon–graphite anodes and its impact on degradation," *Nature Communications*, vol. 12, no. 1, 2021.

[144] X. Zhang, D. Wang, X. Qiu, Y. Ma, D. Kong, K. Müllen, X. Li, and L. Zhi, "Stable high-capacity and high-rate silicon-based lithium battery anodes upon

two-dimensional covalent encapsulation," *Nat. Commun.*, vol. 11, no. 1, pp. 1–9, 2020.

[145] T. Raj, A. A. Wang, C. W. Monroe, and D. A. Howey, "Investigation of Path-Dependent Degradation in Lithium-Ion Batteries," *Batteries and Supercaps*, vol. 3, no. 12, pp. 1377–1385, 2020.

[146] X. Li, A. M. Colclasure, D. P. Finegan, D. Ren, Y. Shi, X. Feng, L. Cao, Y. Yang, and K. Smith, "Degradation mechanisms of high capacity 18650 cells containing Si-graphite anode and nickel-rich NMC cathode," *Electrochimica Acta*, vol. 297, no. 303, pp. 1109–1120, 2019.

[147] J. D. McBrayer, M. T. F. Rodrigues, M. C. Schulze, D. P. Abraham, C. A. Apblett, I. Bloom, G. M. Carroll, A. M. Colclasure, C. Fang, K. L. Harrison, G. Liu, S. D. Minteer, N. R. Neale, G. M. Veith, C. S. Johnson, J. T. Vaughey, A. K. Burrell, and B. Cunningham, "Calendar aging of silicon-containing batteries," *Nature Energy*, vol. 6, no. 9, pp. 866–872, 2021.

[148] M. N. Obrovac and V. L. Chevrier, "Alloy negative electrodes for Li-ion batteries," *Chem. Rev.*, vol. 114, no. 23, pp. 11444–11502, 2014.

[149] M. T. F. Rodrigues, J. A. Gilbert, K. Kalaga, and D. P. Abraham, "Insights on the cycling behavior of a highly-prelithiated silicon–graphite electrode in lithium-ion cells," *JPhys Energy*, vol. 2, no. 2, 2020.

[150] T. Zheng, J. N. Reimers, and J. R. Dahn, "Effect of turbostratic disorder in graphitic carbon hosts on the intercalation of lithium," *Phys. Rev. B*, vol. 51, pp. 734–741, 1995.

[151] T. Zheng and J. R. Dahn, "Effect of turbostratic disorder on the staging phase diagram of lithium-intercalated graphitic carbon hosts," *Phys. Rev. B*, vol. 53, pp. 3061–3071, 1996.

[152] V. A. Sethuraman, L. J. Hardwick, V. Srinivasan, and R. Kostecki, "Surface structural disordering in graphite upon lithium intercalation/deintercalation," *J. Power Sources*, vol. 195, no. 11, pp. 3655–3660, 2010.

[153] L. J. Hardwick, H. Buqa, and P. Novák, "Graphite surface disorder detection using in situ raman microscopy," *Solid State Ion.*, vol. 177, no. 26, pp. 2801–2806, 2006. Solid State Ionics 15: Proceedings of the 15th International Conference on Solid State Ionics, Part II.

[154] E. Sarasketa-Zabala, F. Aguesse, I. Villarreal, L. M. Rodriguez-Martinez, C. M. López, and P. Kubiak, "Understanding lithium inventory loss and sudden performance fade in cylindrical cells during cycling with deep-discharge steps," *Journal of Physical Chemistry C*, vol. 119, no. 2, pp. 896–906, 2015.

[155] M. Lewerenz, G. Fuchs, L. Becker, and D. U. Sauer, "Irreversible calendar aging and quantification of the reversible capacity loss caused by anode overhang," *J. Energy Storage*, vol. 18, pp. 149–159, 2018.

[156] A. Krupp, E. Ferg, F. Schuldt, K. Derendorf, and C. Agert, "Incremental capacity analysis as a state of health estimation method for lithium-ion battery modules with series-connected cells," *Batteries*, vol. 7, no. 1, pp. 1–13, 2021.

[157] C. Y. Chen, T. Sano, T. Tsuda, K. Ui, Y. Oshima, M. Yamagata, M. Ishikawa, M. Haruta, T. Doi, M. Inaba, and S. Kuwabata, "In situ scanning electron microscopy of silicon anode reactions in lithium-ion batteries during charge/discharge processes," *Sci. Rep.*, vol. 6, pp. 1–3, 2016.

[158] K. Richter, T. Waldmann, N. Paul, N. Jobst, R. G. Scurtu, M. Hofmann, R. Gilles, and M. Wohlfahrt-Mehrens, "Low-temperature charging and aging mechanisms of Si/C composite anodes in Li-Ion batteries: an operando neutron scattering study," *ChemSusChem*, vol. 13, no. 3, pp. 529–538, 2020.

[159] K. Richter, T. Waldmann, M. Kasper, C. Pfeifer, M. Memm, P. Axmann, and M. Wohlfahrt-Mehrens, "Surface film formation and dissolution in Si/C anodes of Li-Ion batteries: a glow discharge optical emission spectroscopy depth profiling study," *J. Phys. Chem C*, vol. 123, no. 31, pp. 18795–18803, 2019.

[160] J. M. Reniers, G. Mulder, and D. A. Howey, "Review and Performance Comparison of Mechanical-Chemical Degradation Models for Lithium-Ion Batteries," *Journal of The Electrochemical Society*, vol. 166, no. 14, pp. A3189–A3200, 2019.

[161] C. von Lüders, J. Keil, M. Webersberger, and A. Jossen, "Modeling of lithium plating and lithium stripping in lithium-ion batteries," *Journal of Power Sources*, vol. 414, no. October 2018, pp. 41–47, 2019.

[162] R. D. Deshpande and D. M. Bernardi, "Modeling solid-electrolyte interphase (sei) fracture: coupled mechanical/chemical degradation of the lithium ion battery," *Journal of The Electrochemical Society*, vol. 164, no. 2, p. A461, 2017.

[163] R. Narayanrao, M. M. Joglekar, and S. Inguva, "A phenomenological degradation model for cyclic aging of lithium ion cell materials," *Journal of the Electrochemical Society*, vol. 160, no. 1, p. A125, 2012.

[164] X. Lin, J. Park, L. Liu, Y. Lee, A. Sastry, and W. Lu, "A comprehensive capacity fade model and analysis for li-ion batteries," *Journal of The Electrochemical Society*, vol. 160, no. 10, p. A1701, 2013.

[165] C. Kupper, B. Weißhar, S. Rißmann, and W. G. Bessler, "End-of-life prediction of a lithium-ion battery cell based on mechanistic aging models of the graphite electrode," *Journal of The Electrochemical Society*, vol. 165, no. 14, p. A3468, 2018.

[166] Y. Liu, S. Martinet, C. Louis, A. Pasquier, P. Tassel, and P. Perret, "Emission characterization of in-use diesel and gasoline Euro 4 to Euro 6 passenger cars tested on chassis dynamometer bench and emission model assessment," *Aerosol and Air Quality Research*, vol. 17, no. 9, pp. 2289–2299, 2017.

[167] L. Xia, E. Najafi, Z. Li, H. J. Bergveld, and M. C. Donkers, "A computationally efficient implementation of a full and reduced-order electrochemistry-based model for Li-ion batteries," *Applied Energy*, vol. 208, no. May, pp. 1285–1296, 2017.

[168] A. Aitio, S. G. Marquis, P. Ascencio, and D. Howey, "Bayesian parameter estimation applied to the Li-ion battery single particle model with electrolyte dynamics," *arXiv*, 2020.

[169] S. Santhanagopalan, Q. Guo, and R. E. White, "Parameter Estimation and Model Discrimination for a Lithium-Ion Cell," *Journal of The Electrochemical Society*, vol. 154, no. 3, p. A198, 2007.

[170] W. Plieth, "Electrochemistry for materials science," *Elsevier*, 2008.

[171] T. L. Kirk, J. Evans, C. P. Please, and S. J. Chapman, "Modeling electrode heterogeneity in lithium-ion batteries: Unimodal and bimodal particle-size distributions," *SIAM Journal on Applied Mathematics*, vol. 82, no. 2, pp. 625–653, 2022.

[172] C. Heubner, M. Schneider, and A. Michaelis, "Diffusion-Limited C-Rate: A Fundamental Principle Quantifying the Intrinsic Limits of Li-Ion Batteries," *Advanced Energy Materials*, vol. 10, no. 2, 2020.

[173] M. J. Lain and E. Kendrick, "Understanding the limitations of lithium ion batteries at high rates," *Journal of Power Sources*, vol. 493, p. 229690, 2021.

[174] E. Prada, D. Di Domenico, Y. Creff, J. Bernard, V. Sauvant-Moynot, and F. Huet, " Simplified Electrochemical and Thermal Model of LiFePO 4 - Graphite Li-Ion Batteries for Fast Charge Applications ," *Journal of The Electrochemical Society*, vol. 159, no. 9, pp. A1508–A1519, 2012.

[175] S. R. Eliason, *Maximum likelihood estimation: Logic and practice*. Sage, 1993. 96.

[176] B. O. Koopman, "Hamiltonian systems and transformation in hilbert space," *Proceedings of the National Academy of Sciences*, vol. 17, no. 5, pp. 315–318, 1931.

[177] B. B. Kanbur, V. Kumtepeli, and F. Duan, "Thermal performance prediction of the battery surface via dynamic mode decomposition," *Energy*, vol. 201, p. 117642, 2020.

[178] K. Jalkanen, T. Aho, and K. Vuorilehto, "Entropy change effects on the thermal behavior of a LiFePO 4/graphite lithium-ion cell at different states of charge," *Journal of Power Sources*, vol. 243, pp. 354–360, 2013.

[179] D. Anseán, V. García, M. González, J. Viera, C. Blanco, and J. Antuña, "Dc internal resistance during charge: Analysis and study on lifepo 4 batteries," in *2013 World Electric Vehicle Symposium and Exhibition (EVS27)*, pp. 1–11, IEEE, 2013.

[180] A. Wang, S. O'Kane, F. B. Planella, J. Le Houx, K. O'Regan, M. Zyskin, J. S. Edge, C. Monroe, S. Cooper, D. A. Howey, *et al.*, "Review of parameterisation and a novel database (liiondb) for continuum li-ion battery models," *Progress in Energy*, 2022.

[181] M. Bauer, J. Harlow, T. Hynes, and J. R. Dahn, "Lithium-ion differential thermal analysis studies of the effects of long-term li-ion cell storage on electrolyte

composition and implications for cell state of health," *Journal of The Electrochemical Society*, 2023.

[182] J. L. Proctor, S. L. Brunton, and J. N. Kutz, "Dynamic mode decomposition with control," *SIAM Journal on Applied Dynamical Systems*, vol. 15, no. 1, pp. 142–161, 2016.

[183] S. L. Brunton, B. W. Brunton, J. L. Proctor, E. Kaiser, and J. N. Kutz, "Chaos as an intermittently forced linear system," *Nature communications*, vol. 8, no. 1, p. 19, 2017.

[184] M. B. Tanis-Kanbur, V. Kumtepeli, B. B. Kanbur, J. Ren, and F. Duan, "Transient prediction of nanoparticle-laden droplet drying patterns through dynamic mode decomposition," *Langmuir*, vol. 37, no. 8, pp. 2787–2799, 2021.

Appendix A: Deriving the link between entropy profiling and the differential voltage analysis

The open circuit potential is considered analytical and differentiable. While this condition is true throughout most of the OCP range, the abrupt energy changes accompanying phase transitions result in localised 'discontinuities' on the OCP curve across the degree of lithiation. This rapid change in the OCP gradient is commonly identified by the DVA as a peak on the dV/dQ curve. Because OCP is a function of both lithiation and temperature, discontinuities in x dimension propagate across the T plane (see Fig. A1). Therefore, computing $\frac{\partial \Delta S}{\partial x}$ allows for identification of the same discontinuities as DVA.

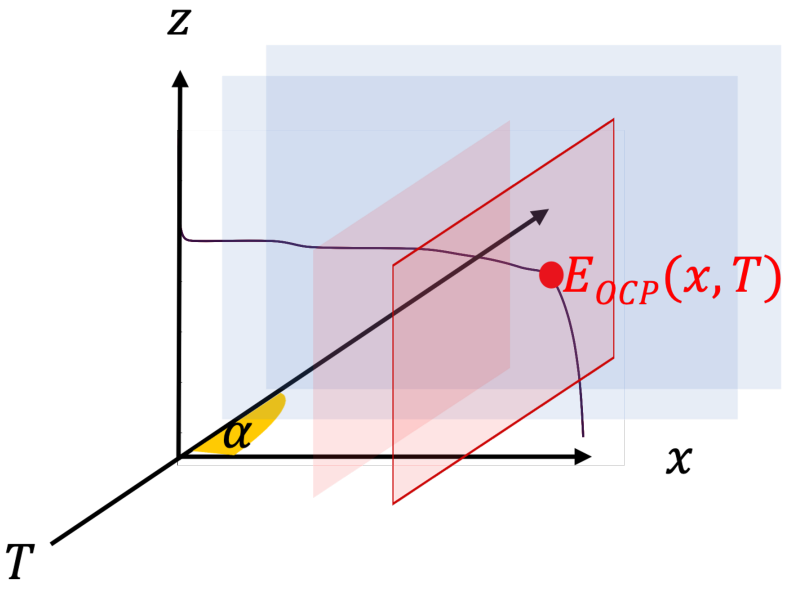

Figure A1: Graphical representation of the open circuit potential (z) dependency on temperature (T) and degree of lithiation (x). Angle α is arbitrary and assumed for visualisation purpose only.

To demonstrate a direct relation between the DVA and entropy change, following equation is derived:

$$\frac{d}{dQ}\left(\frac{\partial E_{\mathrm{OCP}}}{\partial T}\right) \approx \frac{d}{dQ}\left(\frac{dE_{\mathrm{OCP}}}{dT}\right) = \frac{d}{dT}\left(\frac{dE_{\mathrm{OCP}}}{dQ}\right), \tag{1}$$

where DVA is

$$DVA = \left(\frac{dE_{\mathrm{OCP}}}{dQ}\right). \tag{2}$$

Substituting molar entropy change $\frac{\partial \Delta S}{\partial x}$ and DVA into equation (1) gives

$$\frac{d}{dQ}\left(\frac{1}{nF}\frac{\partial\left(\Delta S\right)}{\partial x}\right) = \frac{d}{dT}\left(DVA\right). \tag{3}$$

Appendix B: Entropy estimation algorithm parameter study

Methods considered:

$$\text{Method 1:} \quad E_{\text{OCP,est}} = a + b \cdot \ln(t) \tag{4}$$

$$\text{Method 2:} \quad E_{\text{OCP,est}} = a \cdot e^{-b \cdot t} + c \tag{5}$$

$$\text{Method 3:} \quad E_{\text{OCP,est}} = \frac{a \cdot t}{b + t} + c \tag{6}$$

Table A1: Parameter values together with standard error for a selected point at around 50 % SOC, discharge, for a pristine cell.

Method	parameter value			parameter standard error		
	a	b	c	a	b	c
M1	0.0003313	3.7074226	-	0.0000036	0.0000112	-
M2	0.0382000	0.1302000	4.1229000	0.0005000	0.0033000	0.0002000
M3	525.0908726	-0.0000466	-520.9629492	0.0002537	0.0000028	0.0002537

Appendix C: Optimisation procedure

Given the need to optimise parameters simultaneously using both voltage and temperature measurements, a voltage cost function $J_{\mathrm{V,c}}$ and a temperature cost function $J_{\mathrm{T,c}}$ were used applying the maximum likelihood estimation [175]. The temperature function $J_{\mathrm{T,c}}$ is also assumed to consider average surface temperature $J_{\mathrm{Tavg,c}}$ as well as maximum surface temperature $J_{\mathrm{Tmax,c}}$ contributions. The objective functions are described below as

$$J_{\mathrm{V,c}} = \frac{1}{N_c} \sum_{i}^{N_c} \frac{\left(V_{c,i}^{\mathrm{exp}} - V_{c,i}^{\mathrm{sim}}\right)^2}{\Delta V_{\mathrm{max},c}^{\mathrm{exp}}}, \tag{7}$$

$$J_{\mathrm{Tavg,c}} = \frac{1}{N_c X_c Y_c} \sum_{i}^{N_c} \sum_{j}^{X_c} \sum_{k}^{Y_c} \frac{\left(T_{c,i,j,k}^{\mathrm{exp}} - T_{c,i,j,k}^{\mathrm{sim}}\right)^2}{\Delta T_{\mathrm{max},c}^{\mathrm{exp}}} \tag{8}$$

$$J_{\mathrm{Tmax,c}} = \frac{\left(T_{\mathrm{max,c,i}}^{\mathrm{exp}} - T_{\mathrm{max,c,i}}^{\mathrm{sim}}\right)^2}{\Delta T_{\mathrm{max},c}^{\mathrm{exp}}}, \tag{9}$$

$$J_{\mathrm{T,c}} = J_{\mathrm{Tavg,c}} + J_{\mathrm{Tmax,c}}. \tag{10}$$

$$J_{\mathrm{total,c}} = e^{z_1} J_{\mathrm{V,c}} + e^{z_2} J_{\mathrm{T,c}} - z_1 - z_2. \tag{11}$$

Here, subscript 'c' refers to the C-rate dataset used (4C or 8C pulse), i is the timestep (1 s), and j and k are pixel coordinates in the horizontal (X-axis) and vertical (Y-axis) directions respectively. The superscript 'exp' refers to experimental data, and 'sim' to simulated data; z is an inverse natural log of variance.

Due to the high computational cost of simulating this high-fidelity battery model, a surrogate optimisation technique using MATLAB function `surrogateopt` was employed to reduce the number of cost function evaluations required. The solver searches for the global minimum of the objective function, subject to predefined upper and lower bounds $\min_{\mathbf{x}} f(x)$, such that $lb \leq x \leq ub$. The optimisation was initially set to perform 100 evaluations choosing parameters at random. Subsequently, the adaptive algorithm was initialised, with optimiser performance illustrated in Fig. A2.

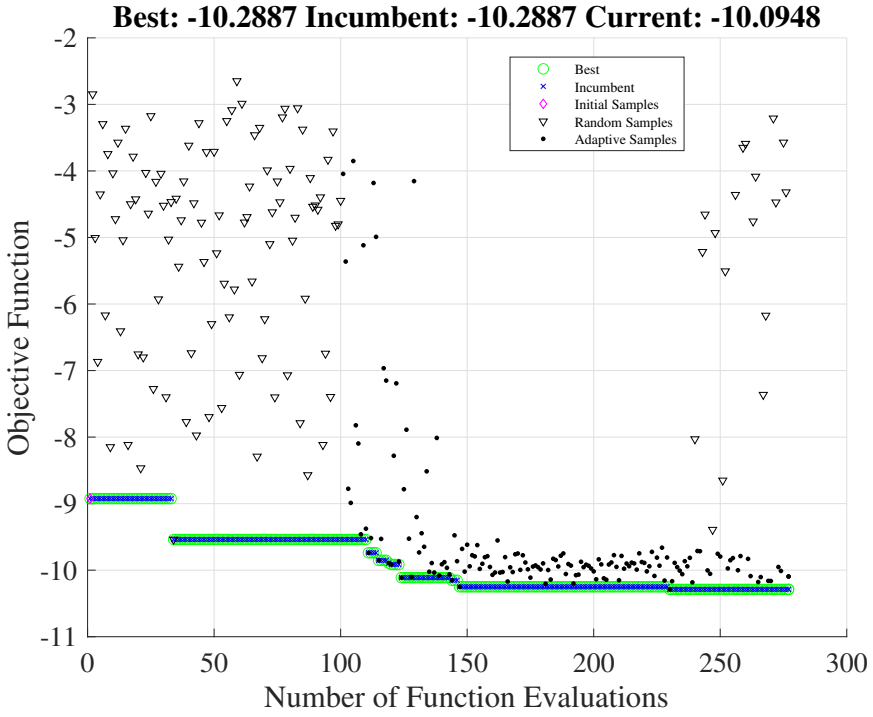

Figure A2: Optimisation cost function output using the 4C 100 s square wave excitation data at 50 % SOC. The first 100 iterations are performed through a random search, followed by an adaptive search.

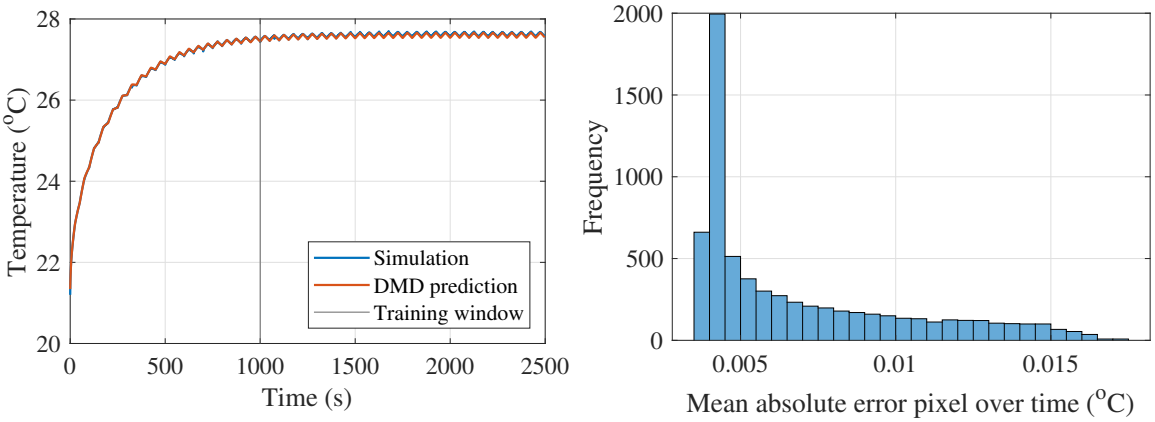

(a) (b)

Figure A3: Prediction results showing the performance of DMD for average surface temperature for 8C COMSOL simulation with arbitrary parameters (a) mean absolute error over time for the worst predicted pixel and (b) error histogram distribution for all pixels.

Appendix D: Dynamic mode decomposition

In Fig. A3, we demonstrate the performance of the above-given algorithm by predicting an 8C COMSOL simulation for an arbitrary step within the optimisation procedure. Prediction up to a time horizon of 1000 s shows great accuracy with very low error, therefore allowing us to shorten the simulation by half.

Despite the high number of pixels available from the IR camera reading, finding the linear map may not be straightforward. Therefore, several augmentations should be done for DMD. First, the effect of the dynamic current in pulse simulations is considered, which leads to the use of DMD with control [182]. Then, to enable computation of thermal gradients with respect to time, the X vector is augumented

with delayed snapshots as well as nonlinear terms [183, 184]. This leads to:

$$\underbrace{\begin{bmatrix} X_4^N - T_{\min,c}^{\text{sim}} \\ X_3^{N-1} - T_{\min,c}^{\text{sim}} \\ X_2^{N-2} - T_{\min,c}^{\text{sim}} \end{bmatrix}}_{Y^+} = A \underbrace{\begin{bmatrix} X_3^{N-1} - T_{\min,c}^{\text{sim}} \\ X_2^{N-2} - T_{\min,c}^{\text{sim}} \\ X_1^{N-3} - T_{\min,c}^{\text{sim}} \end{bmatrix}}_{Y} + B \underbrace{\begin{bmatrix} I_3^{N-1} \\ I_2^{N-2} \\ I_1^{N-3} \\ \left(I_3^{N-1}\right)^2 \\ \left(I_2^{N-2}\right)^2 \\ \left(I_1^{N-3}\right)^2 \end{bmatrix}}_{\Upsilon} \tag{12}$$

$$Y^+ = AY + B\Upsilon \tag{13}$$

Here double delay was used as well as current with the square of the current at the same time. This allowed us to capture the second derivative of the temperature as well as power losses related to the square of the current. As it may not be possible to find high dimensional versions of A and B, SVD was employed to find reduced order versions, following the procedure in [182], we first define Ω by concatenating Y and Υ vertically.

$$\Omega = \begin{bmatrix} Y \\ \Upsilon \end{bmatrix} \tag{14}$$

then the corresponding singular value decomposition is found as

$$\Omega \approx \tilde{U}_r \tilde{\Sigma}_r \tilde{V}_r^{\text{H}} \tag{15}$$

here $(\cdot)^{\text{H}}$ denotes the hermitian (or complex-conjugate transpose) operator and r denotes that only the first r singular values and corresponding singular vectors are

computed and the rest is truncated. Using SVD again:

$$Y^{+} \approx \hat{U}_p \hat{\Sigma}_p \hat{V}_p^{\mathrm{H}} \tag{16}$$

In this study,$r = p = 14$ was used, which is found by trial-and-error. Then reduced order matrices $\tilde{A}$ and $\tilde{B}$ are computed by:

$$\tilde{A} = \hat{U}_p^{\mathrm{H}} Y^{+} \tilde{V}_r^{\mathrm{H}} \tilde{\Sigma}_r^{-1} \tilde{U}_r^{*} \hat{U}_{p,\,1:y} \tag{17}$$

$$\tilde{B} = \hat{U}_p^{\mathrm{H}} Y^{+} \tilde{V}_r^{\mathrm{H}} \tilde{\Sigma}_r^{-1} \tilde{U}_{r,\,y+1:y+q}^{\mathrm{H}} \tag{18}$$

where $a : b$ denotes only rows from a to b are used where y number of rows of Y and q is the number of rows of Υ. Lastly, any prediction of X_{pred} could be written as:

$$z_{k+1} = \tilde{A} z_k + \tilde{B} \Upsilon_k \quad \forall k \in [1, N_{\mathrm{pred}}] \tag{19}$$

$$z_1 = \hat{U}_p^{\mathrm{H}} Y_1 \tag{20}$$

$$X_{\mathrm{pred},k} = \hat{U}_{p,1:M} z_k + T_{\mathrm{min},c}^{\mathrm{sim}} \tag{21}$$

Here $N_{\mathrm{pred}} = 2500$ was used to guess until the 2500 s.